POLITECNICO DI TORINO

Master's Degree in Energetic and Nuclear Engineering

Master's Thesis

Graphene-modified $LiFePO_4$ cathodes for advanced Li-/Na-ion secondary batteries

Supervisor
Prof. Claudio Gerbaldi, Politecnico di Torino

Co-supervisors
Dr. Giuseppina Meligrana, Politecnico di Torino
Prof. Jean-Marie Tarascon, Collège de France

Candidate
Tommaso Platini

March 2019

Table of Contents

List of Figures and Tables

Preface

This work focuses on the development and characterization of nanostructured olivine lithium iron phosphate ($LiFePO_4$) as cathode material for Lithium-ion batteries (LIBs). Nowadays, issues such as how modern society faces challenges related to climate change, air pollution and energy production are a key concern worldwide. The current and future strategies for energy production, storage and distribution go far beyond the fundamental technology-related challenges and involve political and economic repercussions, which require a broad cradle-to-grave knowledge of the materials, energy cycles and geopolitical scenarios. From the first understanding of the critical consequences associated with the uncontrolled rise of human emissions, the scientific community embraced the tough task of developing new and clean solutions to match the energy demand. The global energy scenarios a large growth in the implementation of renewable sources, in particular of the solar and wind-based technologies, which, nonetheless, require a proper storage system to overcome the issues related to their intermittent nature. Moreover, the growing interest in electric (EV) and hybrid-electric vehicles (HEV) is a further reason to claim the importance of the current wide research over electrochemical storage technologies.

The research work in this thesis is included within the broad research topic centred on the development of high performing cathode materials for advanced lithium-ion battery systems. LIBs are the main commercial solution for the smart portable electronic market and the choice of reference for powering the new-born electrical automotive sector, because they combine high energy and power density with lightweight and design compactness, as well as good cycling stability. Recently, research over materials for electrochemical storage systems opened towards a new path, which combines the striking features of graphene in terms of ionic and electronic conductivity and mechanical stability with the deep knowledge on insertion compounds that can host Li^+ ions, responsible for the electrochemical process between the two battery's electrodes. The attention has been focused so far on materials for the negative electrode and several techniques have been developed to form graphene/insertion compounds hybrids, which exploit the appealing properties of the two materials. However, the cathode is particularly critical in determining the capacity of a Li-ion cell and a slight enhancement of its characteristics can trigger huge profits in the overall performance of the battery.

Following this truth, it seemed worthy to explore the possible benefits that graphene might bring to a cathode material which suffers from low lithium-ion diffusion throughout its structure. In this sense, it is explained the decision to focus the experimental activity on $LiFePO_4$. This material, indeed, brings about great advantages in terms of intrinsic safety, abundance and eco-friendliness of the constituent elements, but exhibits poor ability in diffuse Li^+, which graphene it is expected to boost, in particular under high current regimes.

In addition, this work tries to look forward to the future of electrochemical storage beyond Li-ion batteries. Based on the most modern projections that forecast a deep modification of the electric distribution grid because of the large increase in electricity generation by intermittent renewable sources, a multipronged approach with alternative technologies complementing the LIBs appears to be essential for the incoming large-scale production of electrochemical storage systems. In this sense, great research efforts are made on developing Sodium-ion batteries (NIBs), which own several similarities with the Li-ion technology but rely on a cheaper, more abundant and uniformly worldwide distributed fundamental material, namely sodium, Na. Following this environmental sensitivity, $LiFePO_4$ has been used as pristine material to obtain the sodiated equivalent sodium iron phosphate ($NaFePO_4$) that can combine the safety and stability advantages of $LiFePO_4$ with the low-cost and environmental advantages of sodium.

At a formal level, this thesis is structured in four main chapters. Chapter 1 provides a brief but comprehensive overview of the current and projected changes of the energy production scenario, with the intention of stressing on the actual centrality of the research over electrochemical storage technologies. Chapter 2 focuses on Li-ion batteries, explaining their working principle and retracing the history of the main materials implemented in this technology since the initial developments until nowadays. Furthermore, this chapter approaches the main bottlenecks due to the increasing exploitation of lithium raw material and describes Na-ion batteries as the principal alternative under the spotlight of researcher to diversify the large-scale production of electrochemical storage systems. The first part of the experimental activity is addressed in Chapter 3 and deals with the attempt to improve the ability of Li^+ ions to be extracted and inserted in the olivine-type structure of $LiFePO_4$ during the electrochemical charge and discharge processes. Graphene oxide and reduced graphene oxide is added in quality of conductivity enhancers during the electrode preparation step according to an easy and practical methodology that guarantees the homogeneous coating of the nanosized $LiFePO_4$ particles. The electrochemical tests are performed either on a commercial carbon-coated or on a direct hydrothermally synthesized

$LiFePO_4$, focusing on the samples' behaviour under high current regimes. Chapter 4 faces the challenge to use $LiFePO_4$ as pristine material for obtaining the sodiated equivalent $NaFePO_4$. The scope of this activity is to evidence the possibility to completely remove the Li-ions from $LiFePO_4$ and insert the bigger Na-ions into the de-lithiated $FePO_4$, while maintaining the same crystalline structure of the pristine material, which is characterized by favourable cationic channels. Two different methodologies, namely an electrochemical and a chemical process, are used for the purpose and the electrochemical results are analysed in detail. Furthermore, both the $NaFePO_4$ samples, prepared with the two methodologies, are coupled with commercial hard carbon anodes to evaluate the practical application of this material in the full-cell configuration.

The experimental activity related to Chapter 3 has been carried out in the Group of Applied Materials and Electrochemistry lab (GAME lab) of Politecnico di Torino, whereas the experimental activity that refers to Chapter 4 has been developed during an internship project carried out in the Solid State Chemistry and Energy lab at Collège de France, Paris, under the supervision of Professor Jean-Marie Tarascon, principal researcher and lecturer at Collège de France and head of the French network on electrochemical energy storage (RS2E).

1. Global energy challenge

1.1 A changing energy mix

Energy procurement/supply is a polyhedral topic deeply entrenched in the public debate for its technological, social and geopolitical-related issues. The most recent human history has been "powered" by a fossil fuel-based energy system, which is no more sustainable nowadays. The combustion products of these energy sources are among the main causes of environmental pollution, which entails serious repercussions on human health and global warming. Moreover, considering the depletion of resources on which the current industrial system and services are built on, the scientific community wonders for how long it will be possible to sustain the current energy consumption, as well as to support the rapid growth of global energy demand of a constantly expanding world economy, characterized by the gradual spreading of the western lifestyle among the developing countries, involved at the same time in an unstoppable demographic increase. The expected growth of the world population of 1.7 billion people, who will mainly settle in the urban areas of developing economies, determine about 25% increase in world energy demand from now to 2040 (*viz.* up to 18000 Mtoe with respect to 14000 Mtoe of 2017 (**Figure 1.1**).

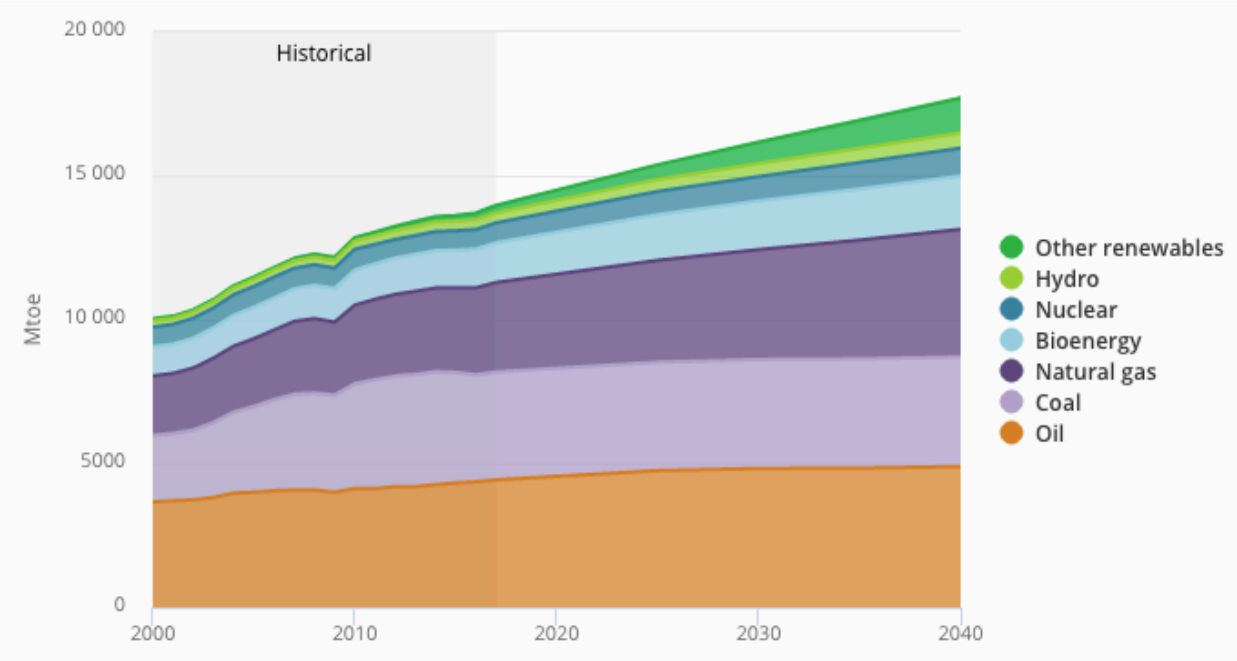

Figure 1.1 World total primary energy demand according to the New Policies Scenario of the IEA's World Energy Outlook 2018 [1].

In addition, a gigantic increase of energy consumption by Asian countries (led by India and China) is expected for all the resources and technologies, as well as investments in the sector. Asia alone accounts for half of the global growth of gas demand: 60% of wind and photovoltaics, 80 % of oil, and over 100% of coal and nuclear consumption.

In the framework of a continuously evolving global energy scenario, the second half of the 21st century has faced several oil crises and sub-sequent – even reckless – races to ensure secure energy supply, leading to unforeseen consequences in the political and societal structures. Luckily, we are now undergoing a global major transformation towards a different energy supply system that focuses on widespread affordability, reliability and sustainability of the energy mix.

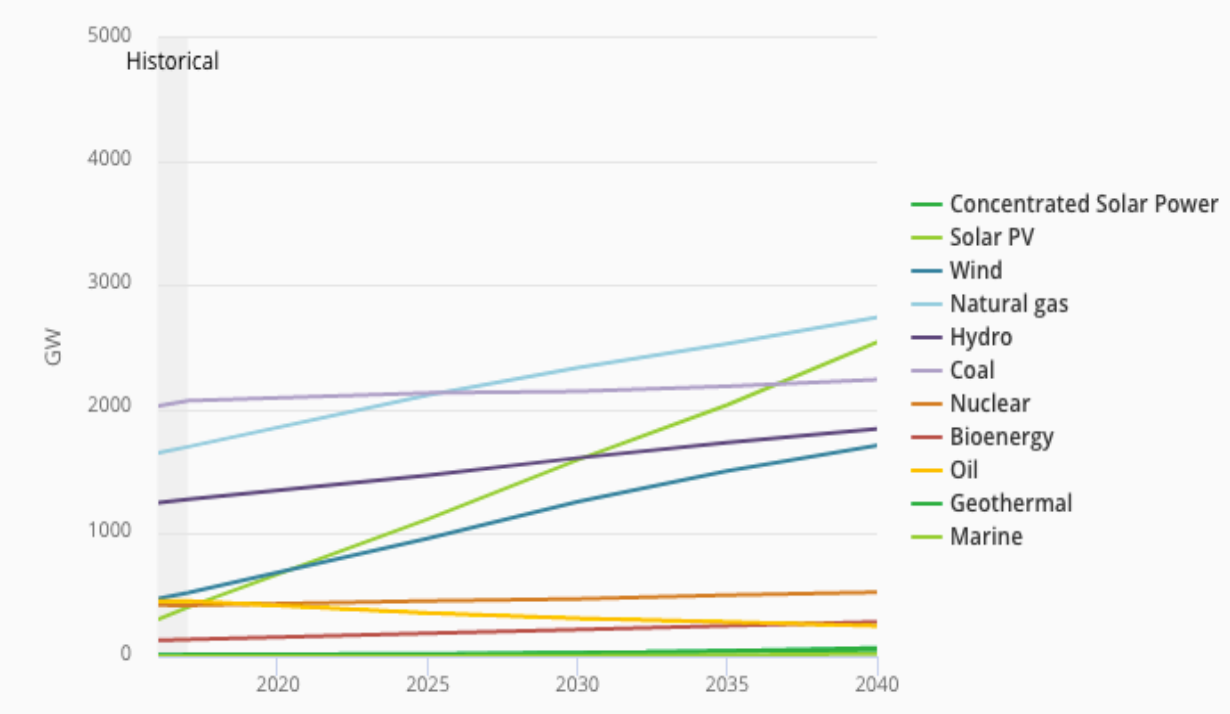

Figure 1.2 Installed power generation capacity by type of source according to the New Policies Scenario of the IEA's WEO 2018 [1].

Although both the current and foreseen energy policies cannot meet the long-term climate goals set by the *Paris Agreement*[1] in 2015 for air pollution and universal energy access, the

[1] The Paris Agreement was negotiated during the XXI Conference of the parties (COP21) of the United Nations Framework Convention on Climate Change (UNFCCC) and set the goal (among the others) to maintain the average global temperature increase well below 2 °C (compared to pre-industrial levels) as a long-term objective; in fact, the attempt is to limit the increase to 1.5 °C, as this would significantly reduce the risks and impacts of climate changes [103].

New Policies Scenario[2] outlined in the *World Energy Outlook* (*WEO*) 2018 foresees much brighter solutions with a drastic increase installed power generation capacity by renewable energies (**Figure 1.2**) and a much larger share in the total energy consumption growth (**Figure 1.3**).

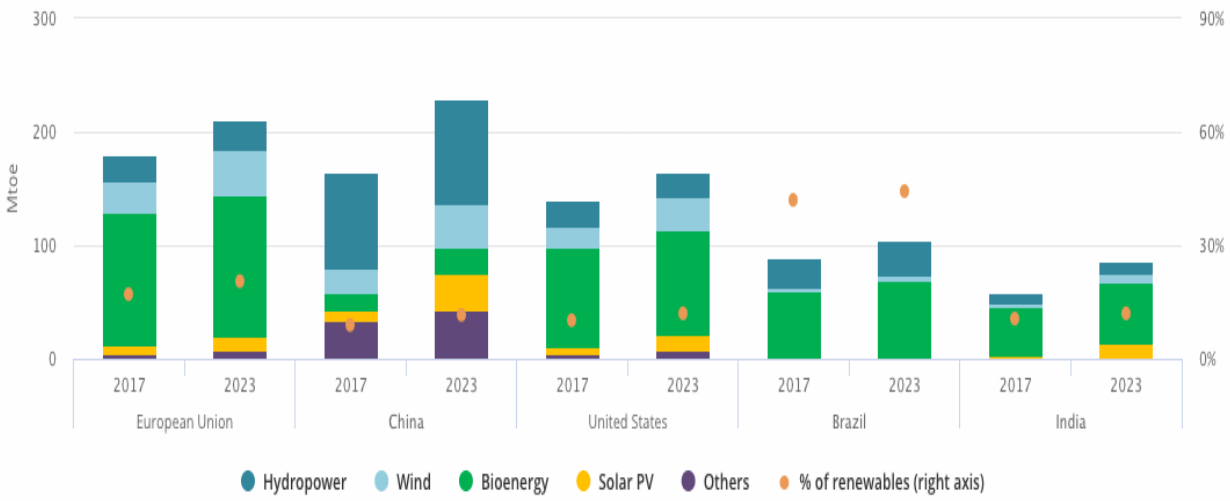

Figure 1.3 Comparison of the renewable energy consumption in major markets worldwide (data from 2017 and 2023), according to the New Policies Scenario of the IEA's WEO [1].

Although the encouraging projections of the New Policies Scenario of a robust implementation of modern renewable energies, it's still a long way up towards a sustainable development that might effectively solve the problems related to environmental pollution and the alarming trends related to global warming. In this sense, the latest projections in the growth of CO_2 global emissions are critical, if one considers the sharp reduction needed to meet the goals of the Paris Agreement on climate change. Indeed, after three years of substantial flatness, global emissions grew by 1.4 % in 2017, reaching a historical value of 32.500 Gt and are expected to increase even more in the coming years (**Figure 1.4**).

[2] The international Energy Agency (IEA) provides medium and long-term energy projections and differentiate between Current and New Policies Scenarios. The Current Policies Scenario only considers the impact of those policies and measures that are solidly enshrined in legislation as of mid-2018, whereas The New Policies Scenario also includes the likely effects of announced policies, including the Nationally Determined Contributions made for the Paris Agreement.

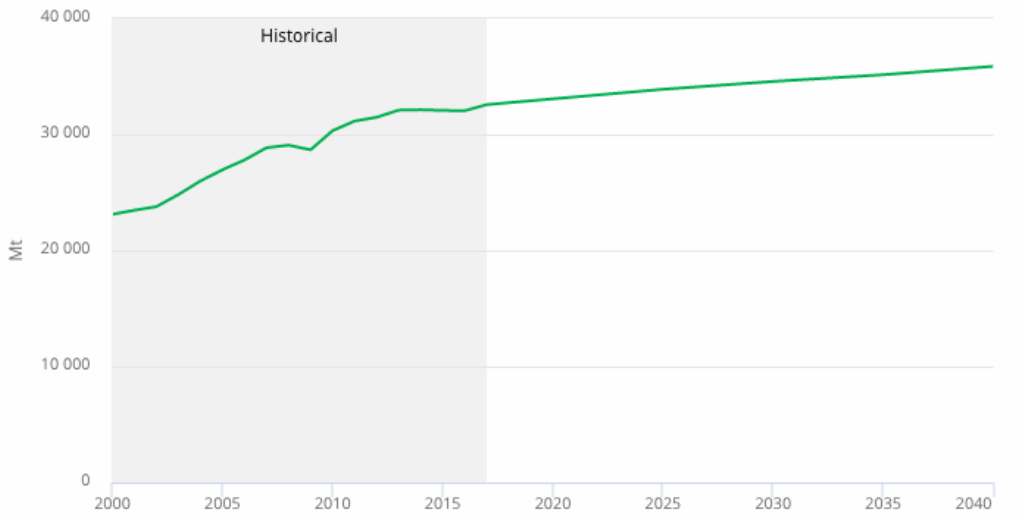

Figure 1.4 Global CO_2 emissions in the New Policies Scenario of the IEA's WEO 2018 [1].

1.2 The importance of electrochemical storage for the supply of electric energy

In the energy supply system, the energy storage devices provide the ancillary services to decouple power generation and load, thus assuring the stability and the reliability of the electrical grid. Among the overall rise in energy demand, electricity demand has seen the most significant increase (3.1 %) in the latest years, and renewable energies accounted for half of the additional electricity production, which resulted in 25% share in global generation in 2017 (**Figure 1.5**). Future projections forecast their increase at about 30 % of global power demand in 2023, counting for the 70 % of the global electricity generation growth in the considered period, leaded by photovoltaics and wind power plants.

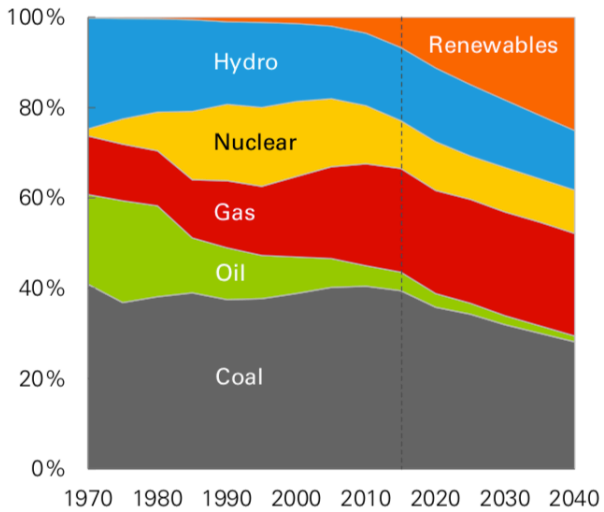

Figure 1.5 Share of present total electricity generation and projections according to the 2018 BP Energy Outlook [2].

The increase in electricity generation from photovoltaics and wind power is fundamental in the concept of 'flexible' electrical grid. Indeed, the electrical system should be able to accommodate the intermittent nature of the modern – expanding – renewable sources, while concurrently ensuring the necessary continuous, non-intermittent supply. The energy storage systems come into the picture in this respect and, beyond the pumped storage hydropower (PSH) that still dominates the present share within the employed storage technologies, electrochemical energy storage technologies are regaining extraordinary importance and attracting global interest among others for their favourable versatility in terms modularity and response time [3] (**Figure 1.6**).

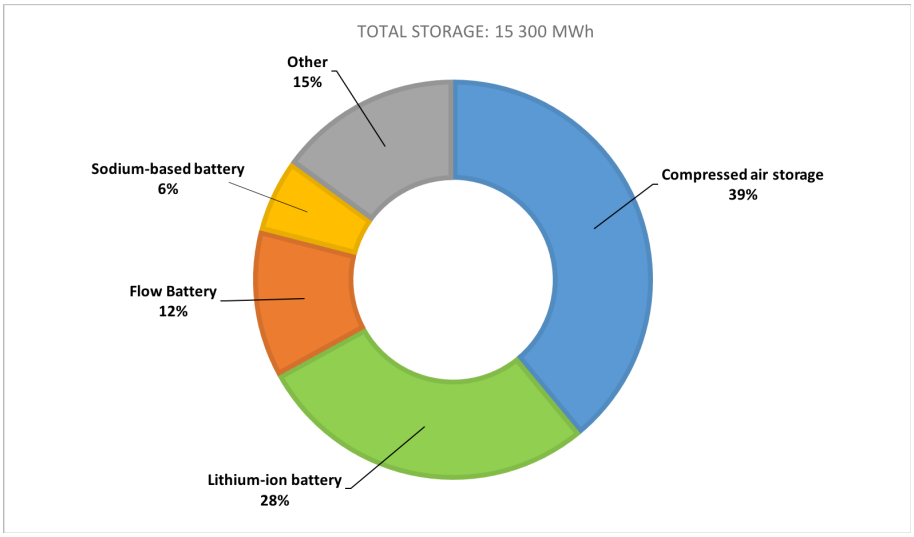

Figure 1.6 MWh of non-hydro installed storage technologies in 2017. Readapted from [1].

Among the electrochemical storage systems, Lithium-ion batteries have shown a massive increase in installed capacity due to a drop in the battery costs of 22 % until 2017 and are the nowadays the technology of choice in the battery's panorama (**Figure 1.7**). However, despite the growth of batteries' installed volume and the continuous implementation of new Pumped-Storage Hydro-electricity (PSH) systems, the consistent addition of 80 GW of energy storage capacity is calculated to be urgent before 2030 in order to match the forecasted increase in electricity production, moreover, a differentiation of electrochemical storage technologies other than lithium-ions is desirable to avoid any concern in active material depletion.

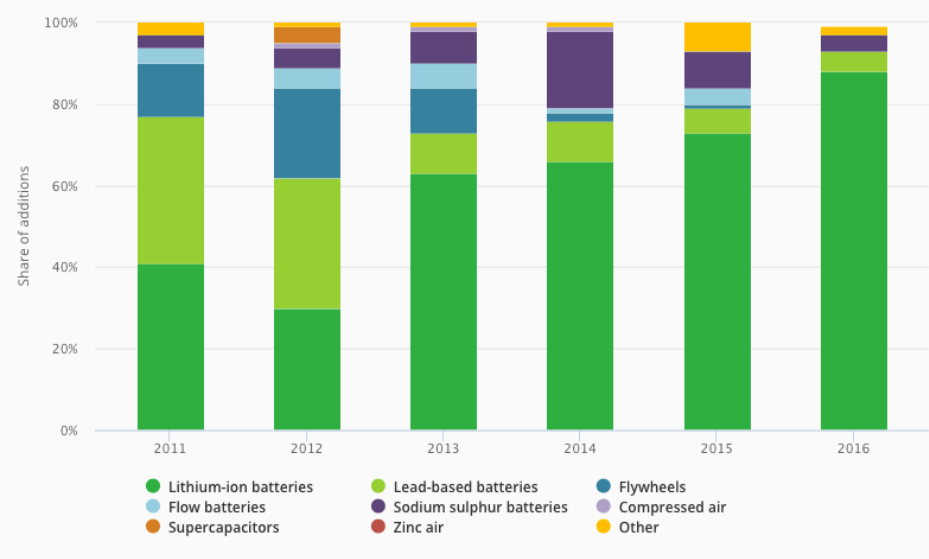

Figure 1.7 Share of annual battery storage additions by technology [1].

1.3 The electrification of the automotive sector

The fast electrification of the global energy supply system is involving also the transportation sector, with projections forecasting a deeper penetration of electric vehicles (EVs) in the market in the nearest future. The latest international agreement on climate change clearly evidence how the reduction of internal combustion engine (ICE) cars leads to a decrease of local air pollution, which concurrently positively impacts over the environment and human health. The electrification of the automotive sector is pictured by the growth in the number of electric cars sold around the world (**Figure 1.8**) in the near past, led by China which doubled the number of electric cars in 2017 and counts for almost 40 % of the global amount.

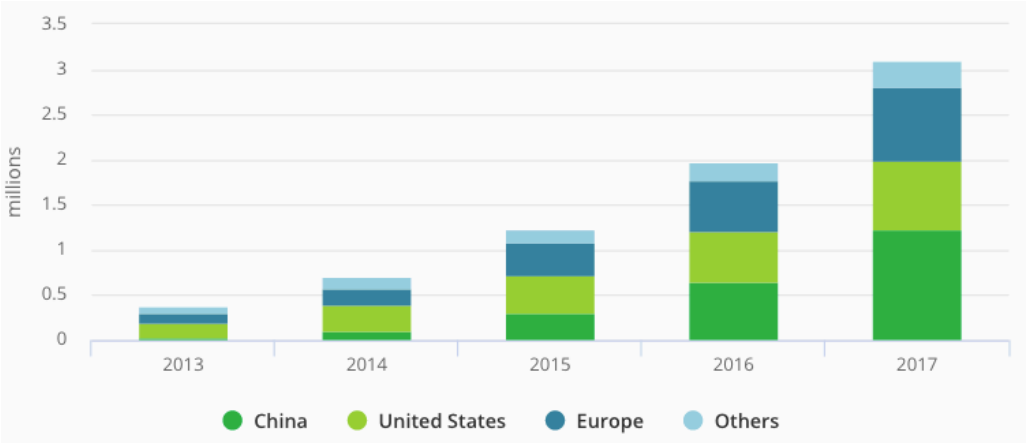

Figure 1.8 Number of electric cars on the road by region, including all the different types of EVs [1].

On the other hand, Scandinavian countries own the highest penetration of electric vehicles in the national market, with Norway leading from the top of his 39 % of electric cars' market share.

The expansion of the electric vehicle's market is mainly boost by the decrease of the cost curve of the electrochemical storage system of choice for the powering the automotive sector, namely Lithium-ion batteries (**Figure 1.9**), thanks to improved performances and increased production.

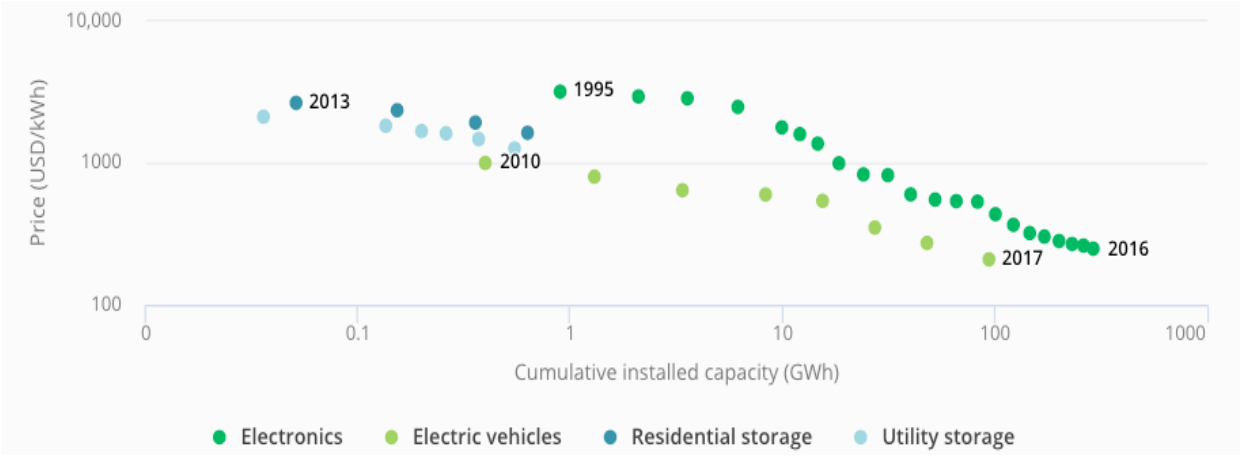

Figure 1.9 Curve of price and cumulative installed capacity of LIBs by sector [1].

The most optimistic scenarios foresee a consistent explosion of the market share of EVs, with more than 300 million cars on the road by 2040, meaning that around 30 % of kilometres per car passenger might be driven exploiting an electric power system (**Figure 1.10**).

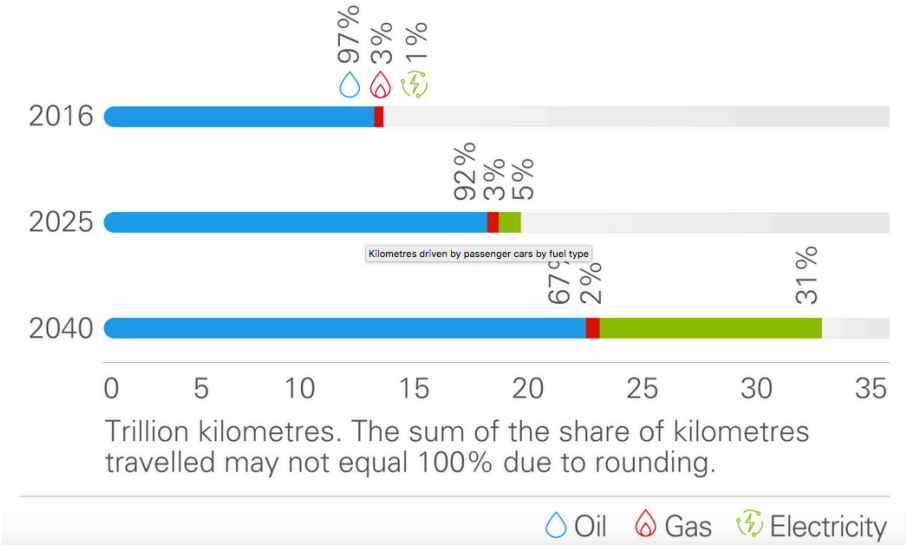

Figure 1.10 Current and future projection of kilometres per car passenger driven by fuel type [2].

However, careful analyses provide a global overview of the transition phenomena occurring to the energy system and, in accordance with a broader prospective of the overall energy cycle, consider the origin of the electricity produced to charge such a great amount of forecasted EVs. In this sense, the increase in electric cars on the road easily implies a short-term increase in the electricity produced by coal power plants, which hopefully will be replaced as large as possible by electricity generation from renewable sources being highly widespread around the world, so as to meet the desired goals of the latest environmental policies for a sustainable development.

2. Lithium-ion batteries

2.1 Electrochemical power sources

2.1.1 General features of batteries

A battery is an electrochemical power source, namely a device capable of converting chemical energy into electrical energy and *vice versa* [4]. A battery is formed by several basic units called cells, each of them composed of three major components:

- the positive electrode (cathode);
- the negative electrode (anode);
- the electrolyte system.

The two electrodes host the electroactive materials, whereas the electrolyte is generally a liquid solution containing a dissociated salt, source of ions. The chemical energy is stored in the electroactive species of the two electrodes and it is converted into electric current by means of electrochemical reduction-oxidation (redox) reactions [4]. The operating principle can be expressed in the form of a closed electrical circuit (**Figure 2.1***)* in which the electrodes provide both the electrons and the ions responsible for the transfer of charge between the two points in the circuit. When the cell is connected to an external load, the current flows spontaneously through the circuit.

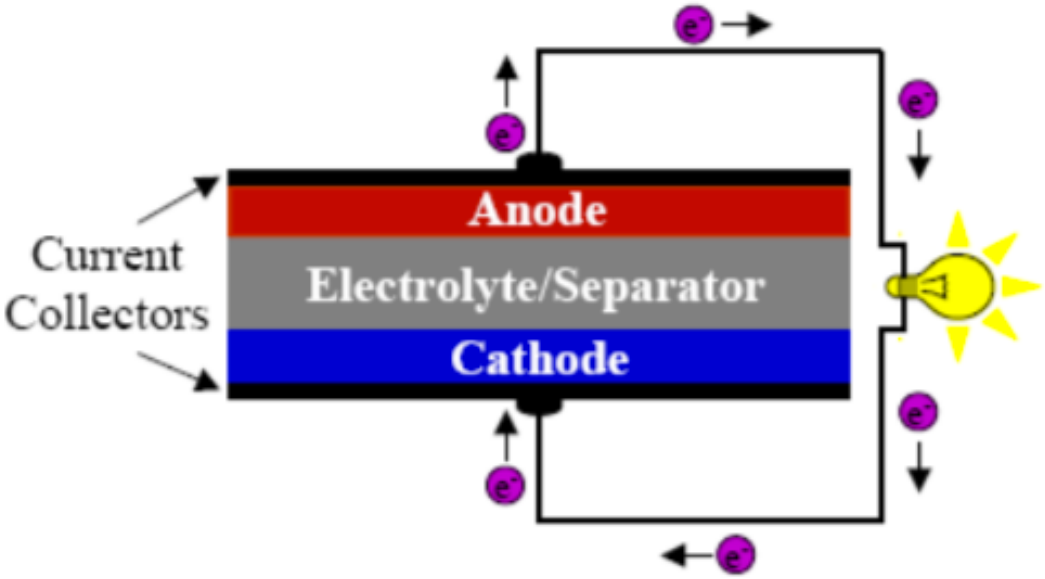

Figure 2.1 Schematic picture of an electrochemical cell (discharge process) [5]

During this spontaneous (discharge) process, at the negative electrode (the reducing electrode), the active material gives up electrons to the external circuit and it is oxidized. Meanwhile, the cathode or positive electrode accepts electrons from the external circuit and it is reduced. The circuit is completed by the electrolyte, the medium for the transfer of cations and anions from the anode to the cathode to balance the overall charge. Hence, the current flow is supported by electrons inside the electrodes and by ions into the electrolyte. Externally, the current flows through the circuit and it is tapped by the user.

According to their ability of being recharged, batteries can be classified in primary or secondary batteries. A *primary battery* is a device that converts the chemical energy of the active species into electricity only once and, then, it must be discarded. More precisely, it undergoes a unique spontaneous discharge cycle driven by the difference in the electrochemical potential at the two electrodes. Conversely, a *secondary battery* can be recharged thanks to an external power supply that forces the non-spontaneous inverse redox reaction during which the cathode active material oxidises and the anode active material reduces (charging process).

2.1.2 Quantities characterising a battery

The electrical energy that a battery is able to deliver is a function of the cell potential and capacity, both of which are linked directly to the chemistry of the system. For this reason, it is essential to define these basic quantities [5].

The *theoretical capacity* (Q_t) is the ideal (maximum) amount of charge that can be extracted from a battery with respect to the amount of active material contained in the electrodes, it can be expressed in *Coulomb [C]* or *Ampere hour [Ah]* (1 Ah = 3600 C) and it is defined as follows:

$$Q_t = x \cdot n \cdot F \tag{2.1}$$

where:

- x = number of moles of active material;
- n = number of electrons/ions exchanged per mole of active material during the redox reaction;
- *F = Faraday constant* in C mol^{-1};

The *practical capacity (Q)* is the actual amount of electric charge supplied by the electrode materials during real operation, and it can be defined as the product of the current delivered and the time:

$$Q_t = i \cdot t \tag{2.2}$$

with *i* being the current (Ampere) and *t* the time (hour). The capacity is strictly linked to the availability of sites in the electrode hosting the ions. In turns, the number of sites depends on the type of nanostructured electrode material and the surface of the electrode itself. Both the theoretical and practical capacities are generally considered in their specific values per unit mass (Ah g^{-1}) or unit volume (Ah dm^{-3}).

The *coulombic efficiency* (Y) is a measure of the reversibility of the electrochemical process and it is defined as the percentage ratio between the capacity delivered during discharge over the capacity accumulated in the previous charge of the battery.

$$Y = \frac{Q_d}{Q_c} * 100 \tag{2.3}$$

The *open-circuit voltage* (V_{oc}) is the potential difference across the terminals of the battery at rest:

$$V_{oc} = -\frac{1}{nF} \cdot (\mu_A - \mu_c) \tag{2.4}$$

where $\mu_A - \mu_c$ is the difference in chemical potential between the anode (A) and the cathode (C). It is important to distinguish between V_{oc} and $\bar{V}$, being the latter the voltage measured during the battery operations.

Once defined the basic quantities determining the battery operation, the related quantities such as energy and power can be introduced.

The *energy (E)* an electrochemical power source can supply depends on capacity and operational voltage and it is expressed in Joule (J) or in Watt hour (Wh):

$$E = Q \cdot \bar{V} \tag{2.5}$$

As in the case of capacity, the specific energy can be defined by referring to the unit mass (Wh g^{-1}) or unit volume (Wh dm^{-3}). Taking into consideration the theoretical capacity, the *theoretical energy* (E_t) can be defined as follows:

$$E_t = \int_0^{Q_t} V(q) \cdot dq \approx x \cdot n \cdot F \cdot \bar{V} \tag{2.6}$$

where V(q) is the working voltage expressed as a function of the supplied electric charge *q*. The *power* (P) delivered by a power source is defined, in Watt (W), as the product of the average working voltage and the current flowing in the system:

$$P = I \cdot \bar{V} = \frac{Q \cdot \bar{V}}{t} = \frac{E}{t} \tag{2.7}$$

From equations (2.5) and (2.6), the *theoretical power (P_t)* can be obtained as follows:

$$P_t = \frac{\int_0^{Q_t} V(q) \cdot dq}{t_d} = \frac{x \cdot n \cdot F \cdot \bar{V}}{t_d} \tag{2.8}$$

where t_d is the time to fully discharge the battery. Other important parameters that give a wider comprehension of the battery characteristics are the *C-rate*, *cycle life, shelf-life, self-discharge* and *overpotential. C-rate* is a measure of the current applied to the system: the current required to fully discharge the battery in 1 hour is indicated with the C-rate of 1C. A C-rate of 0.5C corresponds to the current required to fully discharge in two hours, whereas a current of 2C completes the process in half an hour, and so on. *Cycle life* is a measure of the number of cycles (one cycle is a charge followed by a discharge or *vice versa*) that the battery withstands before starting to deliver a capacity lower than the 80 % of the value at the first cycle. *Shelf-life* and *self-discharge* correspond to the period of time over which a battery can be stored without significant deterioration and the loss of capacity under open-circuit condition due to internal chemical reactions, respectively. The *overpotential* (η) defines the deviation of the operating voltage from the ideal value, given by side reactions and electrode/electrolyte interface modification (passivation). The overpotential is related to the operating conditions and it is positive ($\eta > V_{ideal}$) during charge and negative ($\eta < V_{ideal}$) during discharge and it is represented in the *polarization curve (V_c = V_c (I))*. The polarization curve shows graphically the relationship between the working potential across the electrodes and the current density flowing through the cell.

2.2 Origin of Li-ion batteries

Lithium is nowadays the dominant material in the field of electrochemical storage. The precursor of LIBs (also known with the name of '*rocking chair*' systems) is the rechargeable Li metal cell. The basic concept of Li-metal batteries is to use lithium metal at the negative electrode and an insertion compound to host lithium ions at the positive electrode. The advantages in using Li metal are well known since the early 70s, when the first primary cells were assembled [6]. The reasons behind the huge exploitation of this metal lie in its highly negative redox potential (E°= -3.04 V versus standard hydrogen electrode - SHE) and in its considerable low weight (equivalent weight M = 6.94 g mol^{-1} and density ρ = 0.53 g dm^{-3}), which enable the design of storage systems with high energy density [6]. Nevertheless, Li metal batteries exhibited significant problems due to the high reactivity of Li-metal with the electrolyte, which prevented their widespread intrusion in the market of secondary batteries. In fact, during each subsequent charge cycles, a dendritic plating of Li metal on the negative electrode may arise, leading to the formation of lithium branches that might come into contact with the positive electrode and cause short circuit. The reaction between the ions of the alkali metal and the electrolyte is called *passivation* and causes a great loss in capacity and important safety issues led by a high overheating of the cell.

To circumvent the safety issues of Li metal, the substitution of metallic lithium by a second insertion material (as the compounds used in the cathode) opened the era of LIBs, named after the presence of lithium only in its ionic rather than in its metallic state. Demonstrated firstly by Murphy [7] and then by Scrosati [8], by the presence of insertion compounds in both the electrodes, LIBs solve the problems related to dendrite growth, thus guaranteing enhanced safety. After only about a decade, in 1991 Sony Corporation commercialized the $C/LiCoO_2$ cell, capitalizing the discovery of the highly reversible, low voltage Li intercalation/de-intercalation process in carbonaceous materials [9]. This cell composition led LIBs to such a great commercial success that still today there are no successful contenders in the market. In conclusion, a huge research activity emerged in the following years until the present status with the development of new, highly performing materials, leading LIBss to be the most widely used technology in the electronic portable market, as well as more recently in the rapidly growing electric automotive sector.

2.3 The working principles of Li-ion batteries

A Li-ion battery is a rechargeable electrochemical power source composed of electrode materials that can store Li^+ ions reversibly. The two host materials have the capability of 'intercalate/insert' and 'de-intercalate/de-insert' the Li^+ ions within and from their crystalline structures. The term 'de/intercalation' simply refers to a de/insertion process of ions into a layered host substance, whereas the pure de/insertion terminology is more suitable for those compounds having a 3-D framework containing cavities connected by narrow channels [5]. The figure below shows a sketched picture of the working principles of a LIB (**Figure 2.2**).

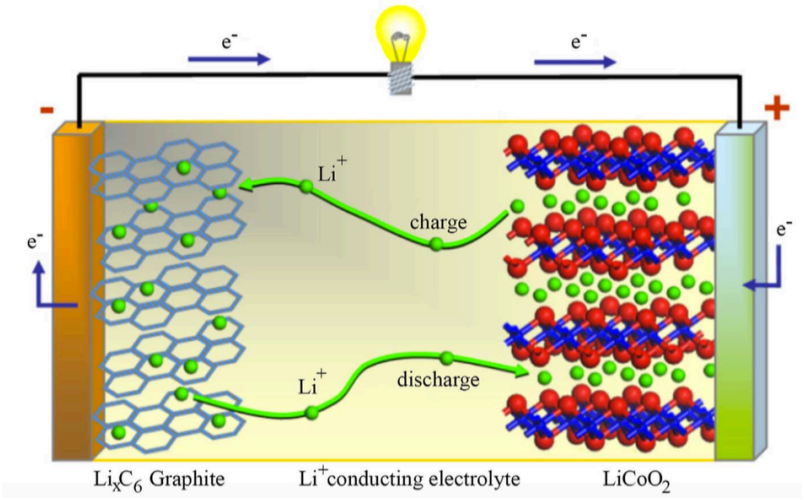

Figure 2.2 Schematic representation of a Li-ion battery [10]

In a charged cell at the open circuit condition, the lithium ions are fully intercalated in the anode structure and an electric field is produced by the difference in the electrochemical potential between the two electrodes. As the circuit is closed, a spontaneous process governed by the negative value of the Gibbs free energy ($\Delta G < 0$) occurs. During this process, called *discharge,* electrons flow from the anode through the external circuit and recombine at the cathode side with the Li^+ ions that are extracted from the active anode material $Li_nA_mB_n$ (de-intercalation) and travelled across the electrolyte. The half reaction is the following:

$$Li_nA_mB_n \leftrightarrow A_mB_n + nLi^+ + ne^- \tag{3.1}$$

The process implies the oxidation of the active material at the anode and the reduction of the active transition metal at the cathode. With the de-intercalation, the Gibbs free energy

difference decreases according to the concentration of lithium ions in the anode active material structure until the end of battery operation. The *charge* of the battery is basically the opposite process. However, being a non-spontaneous ($\Delta G > 0$) process, it requires the application of an external source of power to drive the electrons through the external circuit. Li^+ ions de-intercalate from the cathode structure leaving oxidized the active metal and intercalate into the anode that reduces. The Gibbs free energy, in this case, grows until it reaches the value associated to the full charge state. The half-reduction reaction of the cathode active material ($Li_xM_yY_z$) is:

$$Li_{x-n}M_yY_z + nLi^+ + ne^- \leftrightarrow Li_xM_yY_z \quad (3.2)$$

The overall reaction can be generalized as follows:

$$Li_xM_yY_z + A_mB_n \leftrightarrow Li_{x-n}M_yY_z + A_mB_n \quad (3.3)$$

The process is reversible, thereby allowing lithium ions to move back and forth between the electrodes (here it comes the definition of “shuttlecock” or “rocking chair” battery for LIBs).

2.4 Materials for Li-ion batteries

This paragraph briefly illustrates the development in the electrode and electrolyte materials’ research in Libs along the years. Moreover, the secondary elements needed in the practical cell assembly are briefly introduced in the last section.

Generally speaking, all the fields of application of LIBs require high energy and power densities [11], but each specific sector might focus particular attention on different key properties, accordingly to the characteristics of the device that the battery powers. For example, safety and long operational life are utmost important parameters in the emerging EVs and HEVs markets, whereas other sectors require design flexibility and compactness. However, regardless of the battery technology and application, it is important to remind that the power and the energy delivered by the battery system are directly dependent on its capacity and voltage, which are intrinsically connected to the active materials composing the electrodes. Other characteristics such as cycle-life, lifetime and safety are function also of the nature and stability of the electrode/electrolyte interfaces [6]. Therefore, the basic requirements of any battery technology are related to the intrinsic properties of the materials that form the cells. Thus, advances in the active chemistry that governs the

exchange of lithium ions are fundamental in view of greener and more efficient battery systems.

2.4.1 Materials for the positive electrode

Li-ion batteries originate from the necessity of avoiding the shortcomings of Li-metal at the anode, thus they do not benefit from the theoretically unlimited source of Li^+ ions provided by the negative electrode in the Li-metal batteries. Indeed, in LIBs the positive electrodes act as the source of lithium ions, thus requiring the use of air-stable Li-based intercalation compounds to facilitate cell assembly. With this configuration, the battery is therefore fabricated in the full discharged mode. The solid material that can host the Li^+ guest ion is called intercalation compound. These particular materials should have a proper network of pathways for the lithium ions to diffuse in-and-out of their structure material without damaging irreversibly the structure itself. For this reason, compounds showing cationic channels or interstitial sites between large ions in their structure are suitable as cathode materials. Moreover, the cell operation benefits from cathode materials showing reasonably high electronic conductivity.
In general, intercalation compounds can be identified into:

- metal chalcogenides;
- lithiated transition metal oxides;
- polyanionic compounds.

Furthermore, these three categories are sub-divided according to their crystal structure in:

- layered compounds;
- spinel structured compounds;
- olivine-type compounds;
- tavorite-type compounds.

Metal chalcogenides are the oldest class of cathode materials. The feasibility of the reversible intercalation of Li ions in these compounds has been firstly proven in the mid-1970s when Whittingham [12] proposed TiS_2 as cathode material for non-aqueous secondary batteries.
Lithiated transition metal oxides ($LiMO_2$) easily captured the interest of researchers because of their higher operating voltage and energy storage capability [11], overcoming metal chalcogenides as most promising Li-ion host materials [13]. Lithium ions can easily diffuse

between the O-M-O layers (but not through them) and the strong internal O-M bonds guarantee high stability to the structure [5].

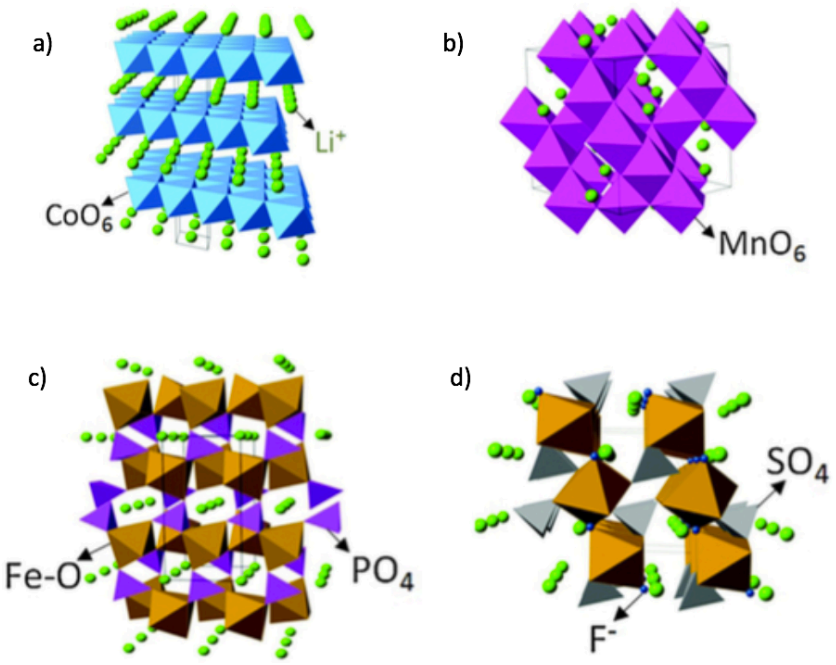

Figure 2.3 Examples of crystal structures of some representative cathode materials for LIBs. a) layered $LiCoO_2$, b) spinel $LiMn_2O_4$, c) olivine $LiFePO_4$, d) tavorite $LiFeSO_4F$. Readapted from [11].

The history of lithiated metal oxides begins in 1980 with the pioneering studies of Prof. J.B. Goodenough and co-workers, who introduced the layered $LiCoO_2$ (LCO) [14]. This very attractive material easily reaches a practical capacity of 150 mAh g^{-1} at the high discharge voltage of 3.9 V vs. Li^+/Li, leading to a specific energy of about 585 Wh kg^{-1}. The theoretical capacity is of 274 mAh g^{-1} and it shows good cycling performance. In addition, LCO shows a self-discharge of only about the 7% after 200 hours at open circuit voltage condition [15]. LCO is still today the most used material in the majority of LIBs and it powers most of the mobile phones and laptop computers in the market. Nevertheless, the high toxicity and cost of cobalt are important drawbacks. Moreover, the de-lithiation process of $Li_{1-x}CoO_2$ shows good reversibility only in the range $0 < x < 0.5$; at higher values, an irreversible change in the structure occurs, causing low thermal stability, oxygen release and corresponding decay of the cycling performances [16], [17]. Therefore, safe operations are guaranteed only if the charging voltage is limited to 4.2 V [18]. Another layered compound similar to LCO is $LiNiO_2$ (LNO), which delivers a specific capacity of 200 mAh g^{-1} at an operating voltage of 3.8 V vs Li^+/Li, but it also suffers from poor thermal stability and cycling capability [19]. These

drawbacks may be controlled by the partial substitution of Ni^{+} with other ions, such as cobalt itself, manganese, magnesium or aluminium. An example is the commercial $LiNi_{0.8}Co_{0.15}Al_{0,05}O_2$ (NCA) cathode used in Panasonic batteries for Tesla EVs [11]. Mg ions insertion in LNO improves the thermal stability at high state-of-charge [20], while Al ions positively affect the electrochemical performances [21]. Eventually, LCO and LNO attracted practical interest because they can form a complete solid solution ($LiNi_{1-y}Co_yO_2$) which can deliver a capacity of 180 mAh g^{-1} and combines both the advantages of the two original compounds [19], [22].

Besides the layered compounds, the spinel structured compounds have been intensively studied from two decades as alternatives cathode materials. Among them, the spinel $LiMn_2O_4$ (LMO) has interesting features including the environmental compatibility and the familiarity of the battery industry with the manganese-based compounds. Studied for the first time in 1983 [23], LMO seemed the perfect substitute for the expensive and toxic cobalt oxide. Unfortunately, it suffers from manganese dissolution into the electrolyte and poor practical specific capacity (100-120 mAh g^{-1}) that might be overcome by the partial introduction of other ions in the structure [24], [25] or by surface modification with oxide coating [26], [27]. Although these thorough attempts, the commercial viability of LMO in large-scale battery production remained limited so far. In order to conclude the transition metal oxide family, other compounds belonging to the manganese family are worth to be cited, such as the layered $LiNi_{1/3}Co_{1/3}Mn_{1/3}O_2$ (NMC) and $LiNi_{0.5}Mn_{1.5}O_4$. The first operates with a sloping voltage averaging around 3.8 V with a practical specific capacity of 160 mAh g^{-1}, whereas the second shows a flat operating voltage profile at 4.5 V vs Li^{+}/Li and a theoretical specific capacity of 156 mAh g^{-1} [28].

Polyanionic compounds are a class of electrode active materials composed of large $(XO_4)^{3-}$ tetrahedra (X = P, S, As, Mo or W) instead of the smaller O^{2-} anion of the metal oxides. They possess higher redox potential with respect to the metal oxides and the strong covalent X-O bond assures excellent thermal stability to the material. On the other hand, polyanions show low electronic conductivity, but as long as the electronic mobility is at least as large as the lithium ions mobility, this disadvantage is not too critical [13]. The excellent intrinsic safety of polyanions makes them suitable for large-scale LIB applications [29]. The most common examples of polyanionic compounds are NaSiCON-type and olivine-structured materials.

The olivine $LiFePO_4$ (LFP) is the representative material for this category of compounds. It is known for its excellent stability and power capability [11] that, in addition to the ability to deliver a practical specific capacity exceeding 90 % of its theoretical value (170 mAh g^{-1}) at

3.45 V vs Li^+/Li [30], make LFP a widespread commercialized cathode material and a serious candidate to lead the rapidly growing EV/HEV market. Other materials owning the phosphate polyanion $(PO_4)^{3-}$ are under study from the early 2000s. Examples includes $LiMnPO_4$, $LiCoPO_4$, $LiNi_{0,5}Co_{0,5}PO_4$ $LiMn_{0,33}Fe_{0,33}Co_{0,33}PO_4$ and, very recently, $Li_3V_2(PO_4)_3$. These materials exhibit the same (or combination of) transition metals of the previously detailed lithiated metal oxides, but take advantage of the structural properties of the phosphate polyanion compared to the O^{2-} anion. $LiMnPO_4$ (LMP) and $Li_3V_2(PO_4)_3$ both provide a relatively high operating voltage (4 V vs. Li^+/Li), but while the former shows a lower conductivity with respect to LFP [31], the latter delivers a good capacity of 197 mAh g^{-1} and it is able to retain the 95% of the theoretical capacity at a current rate of 5C [32].

In recent years, a last group of polyanionic materials is under deep investigation in several research laboratories. They show a tavorite crystalline structure with 1D diffusion cationic channels that facilitate Li^+ de/insertion and add a fluorine ion to the phosphate or sulfate group. $LiFeSO_4F$ (LFSF) and $LiVPO_4F$ (LVP) belong to this category and both of them show good performance in terms of galvanostatic cycling tests in lithium cells. LFSF exhibits high voltage and quite good capacity (151 mAh g^{-1}) [33], but its real advantage is the enhanced ionic/electronic conductivity with respect to most of the polyanionic compounds. LVP, instead, performs well in terms of high voltage and capacity, but the presence of the toxic vanadium rises some concerns for its environmental impact. **Figure 2.4** shows the operating voltage profiles versus specific capacity of some positive electrode materials.

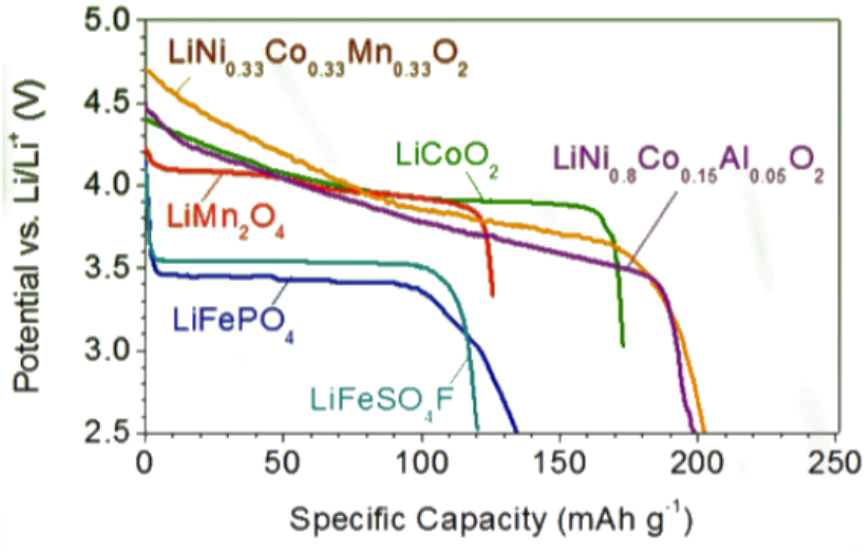

Figure 2.4 Operating voltage profile vs specific capacity of the most widely used/studied positive electrode materials for LIBs [11].

2.4.2 $LiFePO_4$ as cathode material

This thesis work aims to explore the potential improvements of the well-known olivine $LiFePO_4$. A wider discussion over this material and its main applications in the electric automotive sector is, therefore, essential and detailed in the followings.

LIBs composed of $C/LiCoO_2$ anode/cathode combination are still commercially dominant in several sectors, but the toxicity and cost of cobalt are eroding their market share in the production of portable electronic devices and already make them unsuitable for the large-scale battery production (e.g., electric transport on the road and power supply storage systems). In the building of a sustainable society, a greener and more reliable battery technology is fundamental to be coupled to the renewable energy production sector. The mineral triphylite $LiFePO_4$, belonging to the polyanionic cathode compounds, represents a step forward towards the envisaged direction, due to its intrinsic safety and highly abundant transition metal component. The study on phosphate materials started with Padhi and co-workers over twenty years ago [34], and $LiFePO_4$ soon proved to be one of the most promising material, being commercialized since 1999 [35]. The most important features of $LiFePO_4$ can be summarised as follows: reasonably high theoretical capacity of 170 mAh g^{-1}, attractive flat voltage vs current profile at about 3.45 V vs Li^+/Li, environmental compatibility, inherent safety, and presence of the highly abundant iron as active transition metal. In particular, the stability of the material at high temperatures, given by the strong P-O covalent bonds, does not allow oxygen to be released upon overcharging [5]. Among all of these good parameters, the improved safety plays a primary role in considering $LiFePO_4$ a leading candidate as cathode for the next generation LIBs to power the electric cars and/or the intermittent renewable energy supply systems. $LiFePO_4$ has an ordered olivine structure with an orthorhombic crystal system, as shown in **Figure 2.*3c***, and is able to de/intercalate 1 Li^+ ion per formula unit. During the charging process, the extraction of Li^+ ions results in the formation of the heterosite $FePO_4$ [5]. Unfortunately, this material has important drawbacks of low ionic and electronic diffusion, which lead to a considerable loss of capacity at high C-rates and prevent the proper electrochemical operation of the active material particles. Anderson [36], [37] proposed two models detailing the problematic Li^+ extraction/insertion mechanism. The two models are shown in **Figure 2.5**. The 'radial model' hypothesises that during charge the lithium extraction from a particle starts at the surface, leaving an inactive portion of $LiFePO_4$ passivated by a superficial quasi-amorphous layer of

$FePO_4$ that blocks the Li^+ diffusion from the core of the particle. During discharge, the analogous process occurs.

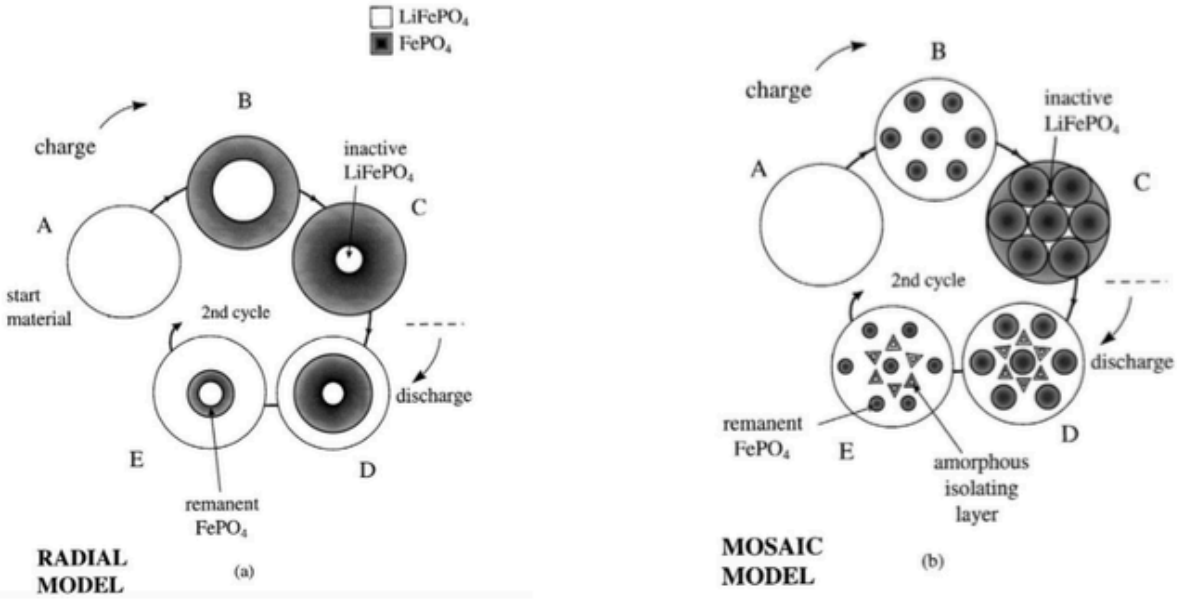

Figure 2.5 Schematic representations of two possible models for lithium extraction/reinsertion into a single LiFePO4 particle: (a) the ``radial model'', and (b) the ``mosaic model''. Readapted from [36]

Differently, the 'mosaic model' hypothesizes that Li^+ de-insertion starts simultaneously in different portions of the particle, leading to the formation of several amorphous insulating layers of $FePO_4$. On the other hand, the implementation of several solutions to lower the capacity loss led, in the past years, to the synthesis of $LiFePO_4$ able to deliver practical specific capacity in the excess of 95 % of the theoretical value. Yamada [38] achieved this result by reducing the grain size, which is a critical issue to minimize the losses. Improvements in $LiFePO_4$ performances were obtained by increasing the conductivity with a carbon-coating of the grains and by adding carbonaceous surfactants to the precursors during synthesis [39]. Carbonaceous surfactants maintain the particles isolated one from each other, thus enhancing intra- and inter-particle conductivity [5]. Further studies on nanostructured hydrothermally synthesized $LiFePO_4$, implying the addition of a second alcohol-based surfactant, managed to enhance the capacity delivered at higher C-rates [40]. In conclusion, the increased performances and the constant operating voltage (it accounts for constant performance upon cycling) and the huge temperature operating range (from -30 to 60 °C) [41] led $LiFePO_4$ batteries with graphitic anodes to be widely commercialized. They endure up to 2000 full cycles and tolerate a wide state-of-charge window (15-100%).

2.4.3 Materials for the negative electrode

Lithium metal would be the best anode material due to its extremely high theoretical specific capacity (3860 mAh g^{-1}), low density (0.59 g cm^{-3}) and the lowest electrochemical potential of -3.04 V vs SHE [42]. Unfortunately, as already explained *paragraph 3.1*, the shortcomings associated with the presence of lithium in its metallic state required the evolution of the technology towards LIBs, by introducing a second insertion compound as negative electrode material. Therefore, also the anode must show the ability to host and deliver lithium ions in a reversible way, accordingly to the charge or discharge processes. In order to increase the potential difference with the positive electrode and, thus, the power delivered by the battery, a proper negative electrode material must have low potential versus the Li^+/Li redox couple.

Carbonaceous materials have been known to intercalate lithium ions since the pioneering work of Herold in 1955 and enabled the LIB technology to become commercially viable since 1991 when *Sony Corporation* released the first commercial Li-ion battery exploiting $LiCoO_2$ at the cathode and soft carbon (more precisely coke) at the anode. Carbon materials with different structural modifications enable the production of anodes and they can be roughly classified in soft carbons, hard carbons and graphite. Soft carbons present a nearly ordered crystalline structure (small crystals stacked nearly in the same direction) that may be induced in graphitisation upon heating. At the contrary, hard carbons show a completely amorphous structure. In the early stages, LIBs comprised soft carbons; however, hard carbons easily replaced the more ordered material offering higher volumetric and gravimetric energy densities [43]. In his review of anode materials for LIBs, Loeffler also explains how the introduction of hard carbons allowed to increase the cut-off potential from 4 to 4.2 V vs. Li^+/Li, enhancing the overall energy density of the device, while enabling excellent cyclability. Nevertheless, the potential profile of both soft and hard carbons is sloping, resulting in a varying overall cell voltage upon operation; furthermore, the full capacity is obtained by exploring very low discharge cut-off potential, which may result in dendritic growth and the related safety issues. In addition, the mobile phone market requires a constant operating voltage exceeding 3 V [44]. Hence, the researchers worked hard to replace those anode materials with graphite, which almost fully satisfies safety and operational issues. Graphite is still today the most widely used anode material for LIBs. The mechanism of lithium intercalation in the active carbonaceous materials of the graphite negative electrode is simply described as:

$$xLi^+ + nC + xe^- \rightarrow Li_xC_n$$

Graphite can intercalate 1 Li^+ per 6 C, leading to LiC_6 after the complete charge process. Alternatively to carbonaceous material, several elements (e.g., M = Sn, Pb, Al, Sb, Zn, Si, In) are able to reach reversibly with lithium to form *metal alloys* (Li_xM) with low operating potential [45]. Metal alloys feature appealing theoretical specific capacity, and appeared for the first time as anode materials in a commercial Li-ion battery in the 1980s [30]. Lithium-silicon alloy, for example, can deliver about 4200 mAh g^{-1}, namely a theoretical specific capacity higher than lithium metal (3862 mAh g^{-1}) and graphite (372 mAh g^{-1}) [5]. On the other hand, metal alloys suffer from severe issues upon cycling, mainly ascribed to the large volume contraction/expansion upon de/lithiation. The excess volume changes lead to fractures in the active material particles, resulting in loss of electronic connection and, in the worst case, to the pulverisation of the material. These fundamental disadvantages hindered the commercial success of metal alloys.

A different approach, suitable for at a power voltage (around 3 V or below) applications, opened new pathways in the search for the optimum anode material. In this regard, lithium titanate ($Li_4Ti_5O_{12}$, LTO) represents a promising alternative to graphite. First reported in 1994 [46], LTO combines a good theoretical capacity (175 mAh g^{-1}) and outstanding cycling stability due to negligible volume expansion. However, the most striking property of LTO is its electrochemical potential of about 1.55 V vs Li^+/Li, which lies within the stability window of common electrolytes, thereby allowing operations without any electrolytic decomposition and SEI formation. Unfortunately, LTO features an insulating character, but this sole disadvantage can be overcome by nanosizing LTO particles to shorten the electron diffusion pathway and increase the electrode/electrolyte contact area [43].

2.4.4 Materials for the electrolyte system

The electrolyte does not provide the active material for the electrochemical reactions, but it is as important as the two electrodes in a battery. The electrolyte works as a bridge between the electrodes and it is in direct contact with all the components in a cell, thus influencing the safety of the whole system. More importantly, the electrolyte/electrode interface affects the chemical stability of the cell, which might significantly limit the effective exploitation of the active electrode materials. Before reviewing the development of the electrolytic systems adopted in LIB technology throughout the years, it is worth understanding the characteristics of the electrode/electrolyte interface in terms of chemical

stability. The active electrode materials in a battery have different electrochemical potential values, as shown in **Figure 2.6**, some of them actually lying outside of the voltage stability window of common electrolyte solutions.

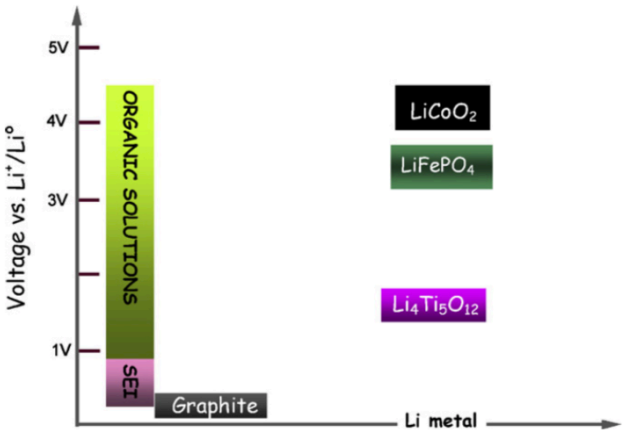

Figure 2.6 Potential vs. Li+/Li of some of the most widely used electrode materials in comparison with the stability window of common liquid organic electrolytes [28].

If the electrode potential (especially of the anode) is outside of the stability window, the electrolyte decomposes, forming a passivation layer called *solid electrolyte interface* (SEI). This surface reaction (**Figure 2.7***)* is a common feature of the anode/electrolyte interface. As a result, a variety of compounds forms, implying a huge loss of lithium ions and, correspondingly, irreversible capacity loss during the first charge cycle. Nevertheless, the formation of a proper SEI layer is fundamental for the long-term operation of a LIB. Indeed, it allows ionic (not electronic) conduction [47], and it is impermeable to the electrolyte molecules, therefore it acts as a protective layer and suppresses the further decomposition of the electrolyte [48]. On the contrary, the intercalation process is not hindered as lithium ions can flow easier through the SEI [47], [49]. The presence/formation of the SEI layer has considerable effects on the development of electrolyte material and remains strictly coupled with the development of the electrodes. The optimum electrolyte must meet the following basic criteria [50]:

- good ionic conductor, while having negligible electronic conductivity to avoid self-discharge;
- wide (electro)chemical stability window in order to be coupled with the majority of electrode materials;
- thermal stability within the range of battery operating temperatures;
- low toxicity and limited environmental hazards

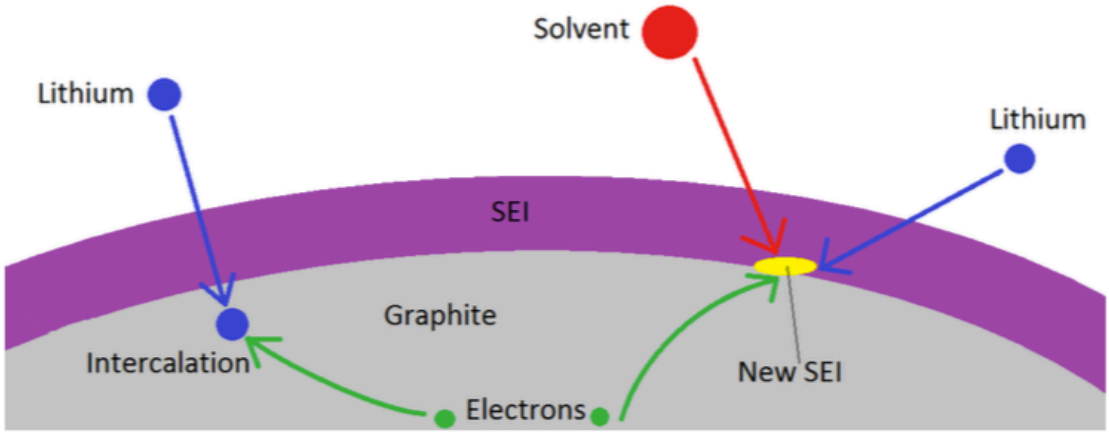

Figure 2.7 SEI formation at anode surface during charge in a LIB [47].

Moreover, low cost and ease of production are highly desirable. The most widely used electrolyte system is based on a lithium salt dissolved in a mixture of *non-aqueous* organic solvents, which is used since the first commercialized LIBs. Generally, the salt is lithium hexafluorophosphate ($LiPF_6$) and the solvent is a mixture of organic carbonates, such as ethylene carbonate (EC) and dimethyl carbonate (DMC), diethyl carbonate (DEC), and/or ethyl methyl carbonate (EMC) [51]. However, carbonate solvents are characterized by low voltage stability and several studies demonstrated that they decompose at above 4.5 V vs. Li^+/Li [52], [53]. On the contrary, organic fluorinated solvents can match the high voltage operating conditions brought by the introduction of higher voltage cathode materials, thus assuring superior electrochemical stability [54], [55].

The progressive widespread diffusion of LIBs towards large-scale production has definitely elevated the safety and stability requirements to a higher level. In this repsect, organic electrolytes are flammable and limit the reliability of the technology. For this reason, environmentally benign and low-cost *aqueous electrolytes* have been studied since the mid-1990s [56]. Lithium salts such as lithium nitrate ($LiNO_3$) or lithium sulfate (Li_3SO_4) in aqueous solvents have been investigated with different electrode combinations, such as $LiV_3O_8/LiFePO_4$ or $LiTi_2(PO_4)_3/LiFePO_4$, with promising results [57], [58]. Unfortunately, the narrow electrochemical stability window (1.23 V) of liquid water restricts the implementation of these electrolytes in LIBs [50]. Recently, a new water-based electrolyte has been proposed, which consists of a lithium salt extremely concentrated in water. Due to the very high salt concentration, this system is called *water-in-salt* and it is characterized by the formation of an interphase between the electrode and the electrolyte that extends considerably the electrochemical stability window [59].

A completely different approach is represented by the development of polymer electrolytes. This class of electrolytes can be subdivided into solid and gel-type polymer electrolytes. The former boasts enhanced mechanical properties. However, both of them have been developed because of the benefits they can provide with respect to liquid electrolytes in terms of safe battery operation [50]. Concerning solid polymer electrolytes, poly(ethylene oxide) (PEO) is the most widely used polymer matrix. Its advantages are stability, safety and the ability to prevent lithium dendrite growth, while the main drawback is its low ionic conductivity at ambient temperature, due to its crystalline nature. The addition of lithium salts, ceramic particles [60] or even carbon nanotubes [61] has been explored during the years to increase the ionic mobility due to enhanced amorphisation, but the slow improvements in the technology did not allowed yet the solid polymer electrolytes to replace the more mature liquid electrolyte systems.

2.4.5 Other materials for the practical cell assembly

The set-up of a battery requires some additional components other than the two electrodes and the electrolyte systems, namely separator, binders and electronic conductivity enhancer.

Concerning the practical assembly of a test cell or a commercial battery, a barrier is required to physically separate the two electrodes in order to avoid internal short-circuit. The so-called *separator* is the essential element that fulfil this task for both liquid and gel polymer electrolyte-based batteries. The separator is placed between the two electrodes and it is completely wet by the electrolyte, allowing the ion transfer without participating at any reaction. The essential properties are: mechanical strength, porosity, chemical and thermal stability [62]. The porosity is a key aspect for separators to allow the proper ionic conductivity of the electrolyte, whereas strength and stability are fundamental properties for the safety of the whole system. If the separator collapses, an internal short-circuit may occur leading to possible thermal runaway and irreversible damage cell failure. Generally, separators are microporous polyolefins, such as polyethylene and polypropylene with a thickness of the order of 25-35 μm.

Binders, instead, are involved in the fabrication of the electrodes and connect the active material particles. Such a coating is important to accommodate the large dimensional change during electrode operations and to make the active material adhere to the current collector. Binders are generally made of polyvinylidenefluoride (PVdF) or a dispersion of olefin elastomers [5]. Being electronic insulators, it is desirable to obtain sufficient binding

properties keeping as low as possible the binder content. Another crucial requirement for binders is the chemical stability with both the electrodes and electrolyte components.

The *electronic conductivity enhancers* are electronic conducting materials (e.g., carbon black), which are mixed with the active electrode material particles to facilitate the Li^+/electron diffusion/insertion. Effective mixing techniques, such as ball milling or magnetic stirring in a solvent, are necessary to get a homogeneous dispersion of the enhancer and the active particles

2.4.6 Graphene in Li-ion batteries

Since its discovery, graphene appeared as a real breakthrough in various fields of material science and condensed-matter physics; more generally, it represented a conceptually new class of materials, the so-called 2-D materials that are only one atom thick [63]. Graphene is a flat monolayer of carbon atoms arranged in a two-dimensional honeycomb lattice, having outstanding mechanical [64], electrical [65] and thermal [66] properties. Being the fundamental building allotrope of common graphite (see **Figure 2.8**), graphene can be employed in a wide range of applications, spacing from electronic to energetic and biomedical engineering.

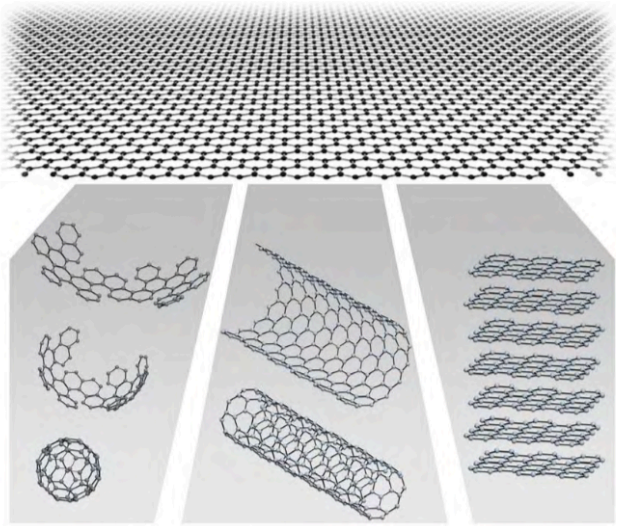

Figure 2.8 Graphene (a) is a single 2D sheet of graphite. It can be wrapped up into fullerenes (b), rolled into nanotubes (c) or stacked into graphite (d) [63].

Among all the remarkable properties of graphene, in this thesis it is exploited for its superior electronic conductivity to enhance the performance of $LiFePO_4$ cathodes at high current densities. Previous works studied the application of graphene nanosheets (GNS) as high

capacity anode materials, due to its higher specific capacity (ranging from 540 mAh g^{-1} to 744 mAh g^{-1} according to the preparation methods) with respect to the commonly used graphite (372 mAh g^{-1}) [67]. While graphite is the most used anode material for its capability to reversibly intercalate lithium ions in its layered crystals, GNSs provide another type of intercalation with enhanced storage capabilities thanks to the optimisation of the intergraphene sheets distance through interacting molecules, such as carbon nanotubes and fullerenes. Other research activities are focused on the implementation of heteroatom graphene doped compounds with tuned high-rate capability and excellent long term cyclability for Li-based batteries, such as Li-O_2 and Li-S. For example, nitrogen- or boron-doped graphene have been reported to show specific capacities higher than 1,040 mAh g^{-1}; however, low coulombic efficiency at the first cycle and fluctuation of capacity due to a manifold surface chemistry and a complex electrochemical behavior of graphene at the electrolyte/electrode interface represent major challenges for the industrial use of graphene-based electrode materials [68]. Regarding LIBs for EV/HEV applications, the preparation of mixed metal oxides with graphene oxide (GO) or reduced graphene oxide (rGO), chemically derived from graphene, is believed to produce graphene/metal oxides hybrids that effectively combine the advantages of graphene and metal oxides, respectively, in terms of high ionic/electronic conductivity and high specific capacity. In addition, the implementation, by different techniques, of thin layers of GO or rGO might also provide solutions to the huge volume contraction/expansion of metal oxides during repeated charge/discharge cycles and for the formation of a more stable solid electrolyte interphase (SEI).

The research activity carried on so far on graphene has been more specifically focused on anode materials; however, the addition of rGO layers has been studied also on cathode for LIBs. In this respect, M. Kim et al. [69] optimized a 'spray-drying' technique to synthesize micro-sized, spherical graphene-based $LiMn_{0.75}Fe_{0.25}PO_4$ composites as cathode material, which exhibit improved electrochemical properties with respect to the basic polyphosphate pristine material.

2.5 Li-ion batteries for application in electric vehicles

Li-ion batteries are the power sources of choice for a wide range of applications, including portable electronic devices, renewable energy supply systems and electric road transport, due to their superior characteristics and advanced performance in terms of highest energy

density, negligible memory effect and low self-discharge rate [41]. According the power supply system, the electric vehicle industry proposes to the market the following different car technologies: hybrid electric vehicles (HEVs), full electric vehicles (EVs), plug-in hybrid electric vehicles (PHEVs), photovoltaic electric vehicles (PEVs) and fuel cell vehicles (FCVs) [70]. Generally, vehicles powered by batteries need the following requirements by the energy storage technology: high specific energy, which guarantees long electric range (autonomy) without the need of recharge, high specific power to contribute the most in terms of horsepower, safety, long lifetime, low cost and lightweight. LIB is now the benchmark technology, but while $LiCoO_2$-based batteries still dominate the portable electronic market, the short cycle life and the cost and safety concerns of the critical raw element, cobalt, left this technology out of the picture for the car industry [35]. The majority of car manufacturers (e.g., Volkswagen Group, General Motors, Toyota) are focusing on NMC as cathode material for its excellent specific energy and lifetime, which favour its utilization in EVs and PHEVs. **Figure 2.9** shows the real trend in the battery sales for electric vehicles, where it is clear the increasing trend of electric vehicle sales in the coming years and the fundamental role played by LIBs in this specific market.

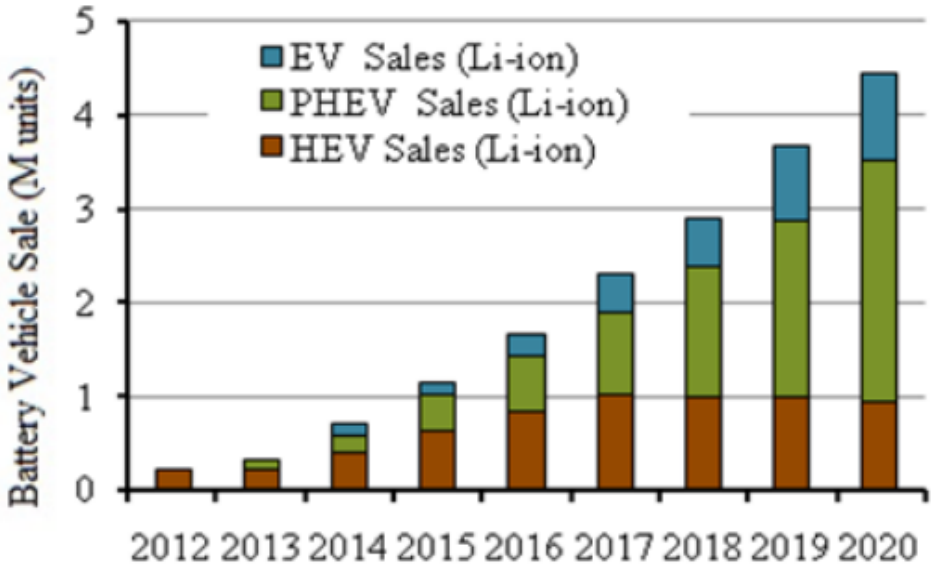

Figure 2.9 Real scenarios and projections of LIB-based electric vehicle sales up to 2020 [41].

Figure 2.10, instead, compares several cathode materials according to their main advantages and shortages. NMC key property is, indeed, the outstanding specific energy. From the analysis of **Figure 2.10**, it appears evident the superior performances provided by

NCA, the application of which is wide but anyway limited by its high cost and safety issues. Only a few companies utilise NCA cells, including Tesla, who produces vehicles with the longest electric range on the market, generally exceeding 400 km (it requires a heavy battery-pack) [35]. In this configuration, NCA provides a lighter battery system. Beside NMC and NCA, the only other cathode material available in the automotive market is $LiFePO_4$. LFP-based LIBs are very safe, rely only on abundant and eco-friendly materials and have a high operational life. However, the distance with the competitor materials in terms of specific energy is still huge. The Chinese car company BYD promotes LFP cells and hopes to recover the gap in performances through cell innovation and further development in LFP performance.

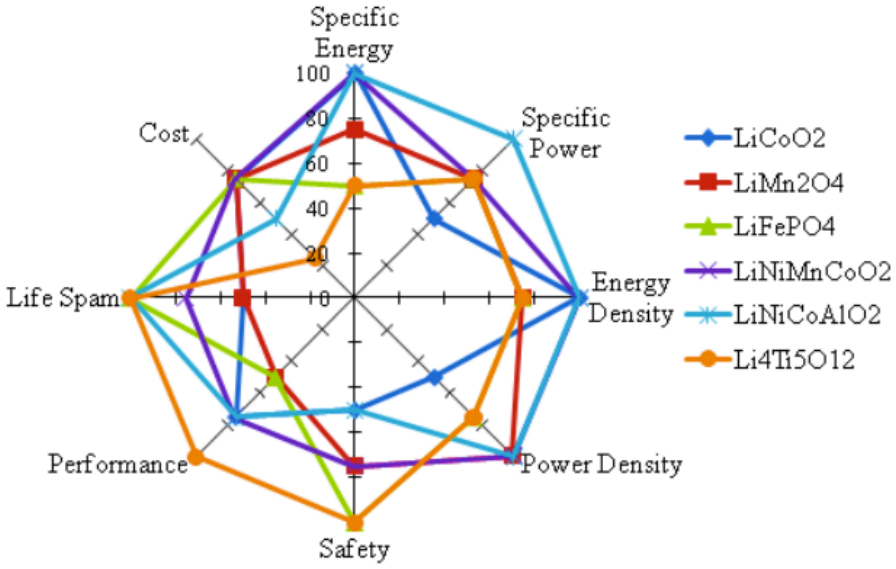

Figure 2.10 Comparison among LIB types (by cathode material) indexed values [41].

An increase in LFP market share is highly challenging as long as performances count more than environmental concerns. Beside public incentives and state regulations to push towards the electrification of road transport, the attraction of customers for EV cars is inexorably related to car performances and decrease in costs. This thesis is directly linked to this topic and tries to propose a solution for decreasing the energy/power performance gap of LFP with the other cathode material contenders.

2.6 Environmental and commercial bottlenecks of Li-ions batteries

2.6.1 Critical raw materials

The current and future strategies for energy production, storage and distribution go far beyond the fundamental technology-related challenges and involve political and economic repercussions, which require a broad cradle-to-grave knowledge of the materials, energy cycles and geopolitical scenarios. For a real sustainable development and for matching the new decarbonisation standards, the modern environmental and energy policies have to develop evaluations of critical raw materials concurrently to the projections of renewable power generations and additions of storage energy capacities. By definition, a critical raw material represents an element with distribution risks [35], based on the following two main factors:

- natural scarcity, in relation to the demand projection of competence sectors;
- supplies concentrated in few countries, especially if located in politically instable regions.

Although the first point can be mitigated by judicious recycling politics, it is generally true that industries not always properly accomplish to this duty, therefore a diversification of technological solutions and materials is becoming a requirement of utmost importance. Concerning LIBs, two elements are nowadays considered critical or nearly-critical in terms of prospective availability and rising demand: cobalt and lithium itself. However, if toxicity and environmental impact have also to be considered, also vanadium-based materials rise some concerns for their environmental unfriendliness. Although cobalt counts on a higher natural abundance compared to lithium, its low concentration in the soil leads to much lower reserves. The majority of cobalt reservoirs are located in Congo, which supplies the 54 % of the global demand, while Australia, Russia, Canada and China count for the 5 % each. Cobalt is very important in LIBs because $LiCoO_2$ still remains the most widely used material for the portable electronic market and Li-ion industry counts for the 30 % of current cobalt global supply. Unfortunately, besides its toxicity and disposal-related issues, serious ethical concerns animated the public debates for the unruled mining activity in the conflict-stricken Congo, which operates under low safety standards and high levels of toxicity due to water pollution to which local communities are exposed [71].

2.6.2 Lithium as the 'new gold'

Since 2010, electrochemists pondered on the expectations of LIBs to power the new born electric automotive sector in relation to the available lithium resources [72]. Unfortunately, the question is still valid today: according to the foregone explosion of EVs/HEVs production, lithium might experiment a considerable increase in its price with a consequent race of developed countries to control its reserves, mainly located in concentrated regions facing political instability.

According to *USGS* (*United State Geological Survey*), world lithium resources have been revised to approximately 47 million tons in 2018, while the Global Lithium Reserves[3] are calculated to be 16 million tons [73] and are primarily located in Andean South American countries besides China, Australia, Canada and Russia. Lithium is extracted for the 80 % from brine lakes and saltpans, while the 20 % remaining comes from hard rock resources at higher production costs. LIBs are the main end-use market, counting for the 39 % of the global lithium consumption (37800 tons in 2016) and market previsions forecast that this share will rise at 50 % in 2020. In addition, the cumulative Li-ion market for the period 2020-2030 is forecasted to be 2.5 TWh, meaning a cumulative Li-demand of about 400000 tons, equivalent to the 2.5 % of the global lithium reserves, according to the current material intensity of 0.16 kg kWh^{-1}. The energetic transition implies the conversion of the pollutant fossil fuel-based cars in electric vehicles and LIBs are the technology of choice as power delivery system. However, at the moment, over 70 millions of cars are produced [74] every year and a full conversion to EVs or PHEVs would alarmingly increase the depletion rate of lithium over the actual depletion rate of oil; in addition, the analysis on lithium geological reserves prove that there is no sufficient economically recoverable material to bear the forecasted electric vehicle production [75]. Furthermore, the parallelism with oil holds on the concentration of supplies that might create new geopolitical tensions, with the Andean South American countries being considered as the 'new Middle-East' [72].

The global projection over lithium depletion and costs is even worse if one considers the desirable increase in electricity production from renewable energy sources. Cobalt-free LIBs, indeed, match the technological and environmental requirements for a highly efficient storage system of the electricity produced by the intermittent renewable energy sources and they are considered the technology of choice for future smart grid-connected energy storage systems. On the other hand, they already struggle when it comes to compete at cost

[3] By definition, the 'reserves' are those parts of the resource that can be economically extracted or produced at the time of the determination [75].

level and the discussed projections in the large-scale production market do not help in this respect. Currently, a Li-ion battery pack costs around 300 € kWh^{-1} and has a lifetime of 2000 cycles [35], which means an energy storage cost of 20 c€ kWh^{-1}, the double of the competitive cost for grid-connected storage systems of 10 c€ kWh^{-1}. Realistic long-term projections underline that LIBs will become competitive for a grid-connected use only if the cost of the battery pack will decrease at 200 € kWh^{-1} and the lifetime will concurrently increase at 2500 cycles, at least. In this way, the energy storage cost will stand behind 7 c€ kWh^{-1}. In terms of Li-ion chemistry, $LiFePO_4$ has the potential to be the dominant cathode material for the grid-connected energy storage systems, thanks to number of advantages previously discussed. Nevertheless, as already described, long-term scenarios categorized lithium as nearly-critical raw material, therefore it is not safe to strongly depend on lithium supplies. In this direction, recycling policies and diversification of electrochemical storage solutions are highly recommendable.

2.7 Diversification of the electrochemical storage for large-scale production: sodium ion batteries

As the large-scale production of LIBs for electric vehicles and power supply applications will enhance the shortcomings of lithium in terms of costs and availability, the diversification of electrochemical storage solutions is fundamental in the present scenario.

Sodium-ion batteries (NIBs) are among the most attractive alternative rechargeable systems because of the abundance (with uniform geographical distribution) and low cost of sodium raw material reserves, as well as the very similar operating principles with LIBs and reliance on eco-friendly materials. Indeed, sodium is the fifth-most abundant element on earth and the second lightest alkali element on the periodic table (after lithium) [76]. Unfortunately, the slightly higher redox potential of the Na^+/Na redox couple with respect to Li^+/Li (–2.71 compared to –3.03 vs. V vs. SHE, respectively) leads to lower values of energy density, which is an issue for both the EVs and PHEVs markets. Nevertheless, the research on cathode materials operating at higher voltage might overcome this drawback. On the contrary, the limited 0.3 V increase in redox potential does not lead to serious concerns regarding electrochemical storage systems for energy storage from renewables and large scale power supply for the grid, which do not need extremely high power and energy densities. Therefore, the advantages of sodium abundancy, reliance on eco-friendly materials and appealing operating features account for the role of NIBs as the most promising technology

for battery production in large volumes, in particular for the electrochemical storage of renewable energy power supplies, without splitting into the undesired lithium bottlenecks in terms of costs and geopolitical tensions.

Although researchers started to focus their attention on Na-based technologies alongside LIBs in the late 1970s, the benefits of Li-based electrochemical storage technologies in terms of higher energy density attracted the focus of both the scientific community and the battery producers away from sodium [77]. Therefore, the commercialization of Na-based batteries is still in its early stages of development. Nevertheless, the available Na-based technologies can be divided into two distinct categories: high temperature and low temperature sodium-based batteries. Sodium-sulfur, sodium-air and ZEBRA (Zero-Emission Battery Research activities) belong to the former category and, generally, imply molten sodium as negative electrode material, while NIBs are the main technology developed for low temperature operating conditions and they own several similarities to the LIB counterpart both in terms of working principles and component materials. Indeed, in a Na-ion cell the negative electrode oxidizes during discharge, releasing Na^+ into the electrolyte while electrons travel across the external circuit and recombine at the positive electrode, which reduces. During charge, the opposite process occurs due to the extraction of Na^+ from the cathode material structure.

2.8 Materials for sodium-ion batteries

In general, the main materials for NIBs are very similar to those developed for Li-ion cells. Nonetheless, the higher ionic radius of Na^+ (102 pm vs. 76 pm for Li^+ [78]) and the different interaction between Na^+ with the host structures generally lead to substantial differences in the materials behaviour in terms of structural volume changes and electrode/electrolyte interface reactions, which may cause dissimilar subjection to usury and structural resistance, respectively.

2.8.1 Materials for the positive electrode

NIBs rely on positive electrode materials able to de/intercalate Na^+ across their crystalline structure. Similar to the corresponding LIB cathodes, they can be categorized into *sodiated transition metal oxides* and *polyanion compounds.*

According to their crystalline structure, oxides can be further divided in tunnel-type and layered compounds. Sodium manganese oxide ($Na_{0.44}MnO_2$) is the first material, which attracted the attention of researchers for its ability to tolerate highly stressful structural changes during the insertion/de-insertion of sodium ions within its 'tunnel-type' crystalline structure [79]. The redox process revealed multiple voltage steps over the range of 2-3.8 V with specific capacity of about 140 mAh g^{-1}. Despite the unappealing irreversibility shown when the material was charged beyond x = 0.25, $NaMnO_2$ appeared attractive for the implementation in water-based and hybrid Li/Na-ion batteries. Layered oxides mainly include the sodium intercalated equivalent of the lithiated transition metal oxides having the formula AMO_2 (where A = Li, Na and M = Co, Mn, Ni and different combinations thereof); nonetheless, they exhibit substantial differences in terms of redox potentials and phase evolutions during cycling, mainly caused by the larger size of Na^+ that often leads to disruptive structural changes and step-wise voltage profiles [76]. Taking $LiCoO_2$ and $NaCoO_2$ as examples, they own the same framework of CoO_6 edge-sharing octahedra, but $NaCoO_2$ shows numerous phase transitions and larger hysteresis losses during cycling (see **Figure 2.11**), leading to the limited exploitation of only half of the theoretical capacity [80]. However, the partial substitution of Co with Fe, Ni or Mn can tune the electrochemical performances, giving rise to layered oxides resulting by the combination of several transition metals such as $Na_{0,33}Co_{0,66}Mn_{0,33}O_2$ or $NaFe_{0,5}Co_{0,5}O_2$.

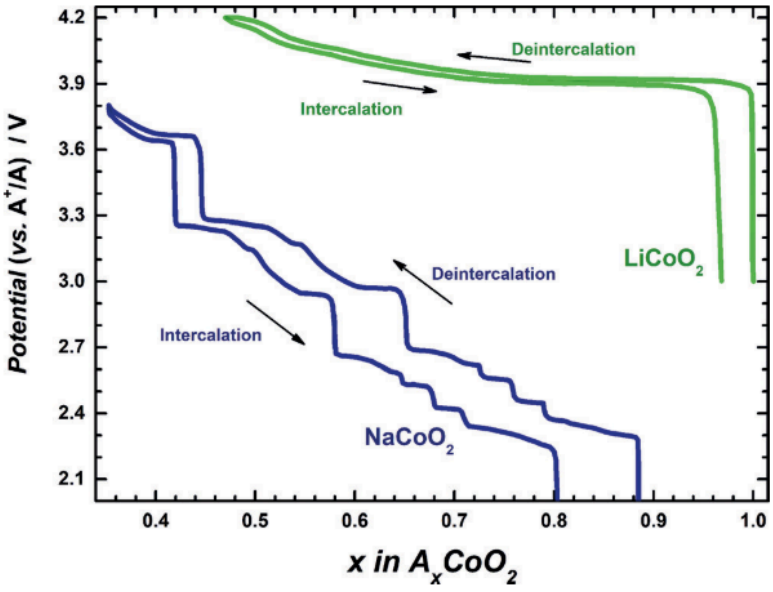

Figure 2.11 Potential vs. amount of inserted alkali metal ion profiles of Li/LiCoO2 (green line) and Na/NaCoO2 (blue line) cells.

$NaFeO_2$ is another layered-type oxide, which delivers capacities of about 100 mAh g^{-1} when cycled up to 3.4 V, but it suffers from capacity fading when the cut-off voltage is set above 3.5 V vs. Na^+/Na. The equivalent $LiFeO_2$ exhibits the same capacity loss issues due to cationic disorder, but only at voltages higher than 4.2 V vs. Li^+/Li.

Concerning the second class of materials for the positive electrode, intensive research is now focused on polyanionic insertion compounds because of their higher operating voltage and intrinsic safety. The former advantage is of major concern bearing in mind the higher redox potential of sodium compared to lithium [76]. As in LIBs, phosphate compounds are among the most investigated systems. *NASICON* (Natrium Super Ionic CONductors)-type compounds are the oldest phosphate systems and include vanadium-, iron-, chromium- or titanium-based polyphosphates (e.g., $Na_3V_2(PO_4)_3$, $Na_2TiFe(PO_4)_3$, $Na_2TiCr(PO_4)_3$). However, their intermediate voltage makes them less attractive than other phosphates, such as olivines or fluorophosphates. In LIBs, olivine $LiFePO_4$ has been the first commercialized phosphate material and the corresponding isostructural sodium compound ($NaFePO_4$) exhibits the same appealing electrochemical features of its Li-based counterpart. Unfortunately, $NaFePO_4$ appears in nature in its maricitic form, which is thermodynamically stable, but electrochemically inactive. However, as reported in the pioneering work of Moreau et al. in 2010 [81], it is possible to electrochemically or chemically intercalate sodium ions into the de-lithiated $FePO_4$ in order to form an isostructural orthorhombic $NaFePO_4$ (**Figure 2.12**), which takes advantage of the characteristic cationic channels of the olivine-type crystalline system for a rapid, easy and fast Na^+ extraction and insertion.

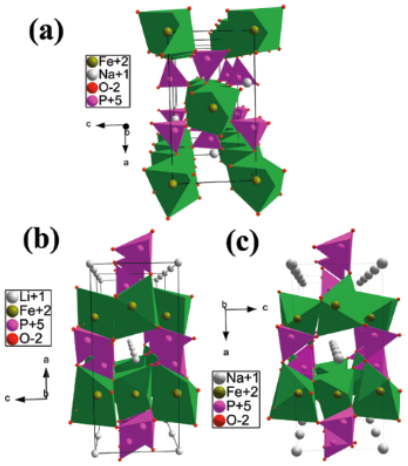

Figure 2.12 Different structures of maricite NaFePO4 (a), olivine LiFePO4 (b) and olivine NaFePO4 (c) [81].

Olivine $NaFePO_4$ can reversibly de/intercalate Na^+ ions with good cycling stability and reasonably high values of specific capacities of 120 and 100 mAh g^{-1} at C/20 and C/10 rates, respectively. Because of the larger size of Na^+ with respect to Li^+, it exhibits a volume contraction/expansion of about 17%, more than twice that of Li-olivine (7%), and undergoes more complex phase transformations during the extraction and insertion of Na^+. Actually, a voltage profile with a double plateau arises at 3 and 3.2 V vs. Na^+/Na during charge, due to the formation of an intermediate phase having a higher kinetic barrier. On the contrary, a single plateau is observed at 2.8 V vs. Na^+/Na during discharge, accounting for the intercalation of Na^+ (**Figure 2.13** and **Figure 2.14**).

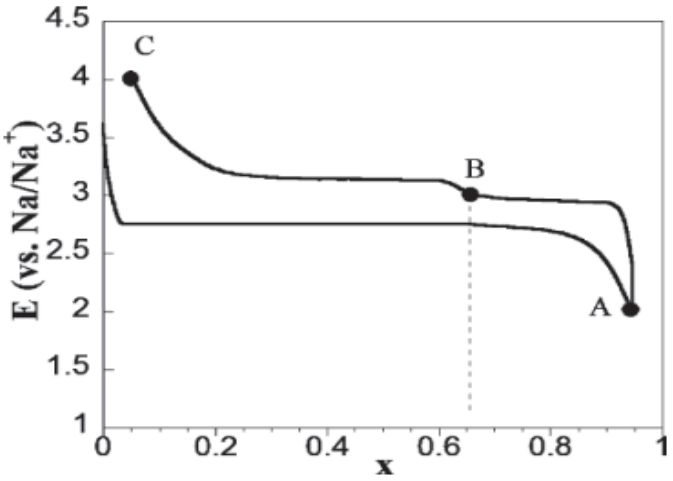

Figure 2.13 The characteristic electrochemical profile of the olivine NaFePO4 showing the single plateau in discharge and the double plateau in charge [81].

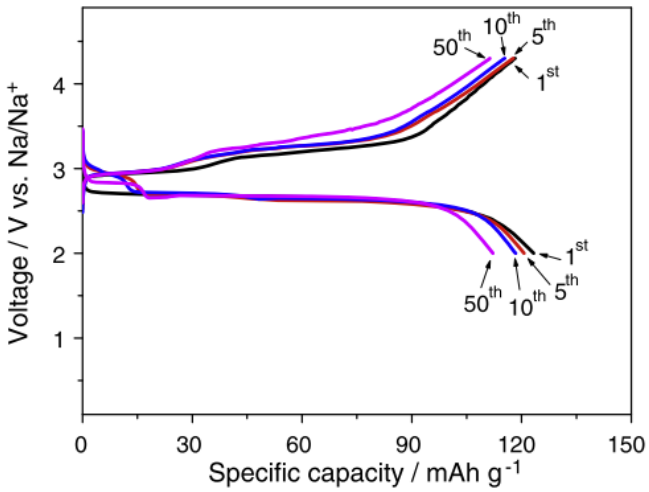

Figure 2.14 Potential vs. specific capacity profiles of the olivine $NaFePO_4$ upon 50 consecutive charge/discharge cycles at C/20 [82].

2.8.2 Materials for the negative electrode

The main difference with LIBs regards the choice of the materials for the negative electrode. Irrespectively to Li^+ ions, Na^+ ions do not easily intercalate within the ordered graphene sheets, which restricts the use of *graphite* as NIB anode material. Some challenging issues concerning the structural evolution and the need of using ether-based electrolytes, which strongly bond to Na^+ [83], [84], must be solved in this respect. Because of the larger ionic size of Na^+ ion, Wang et al. proposed the synthesis of graphite from GO with expanded distance between the graphene layers, obtaining a reversible capacity of 248 mAh g^{-1} and cycle life of 2000 cycles [85]. On the other hand, sodium ions can insert into the highly disordered structure of *soft carbons* and within the short-range ordered structure of *hard carbons*. The latter, in particular, is the most appealing anode material because it exhibits high specific capacity of 300 mAh g^{-1} and a favourable insertion mechanism of Na^+ ions, which is described as the 'house of card' model (**Figure 2.15**), at approximately the same potential of the sodium metal itself.

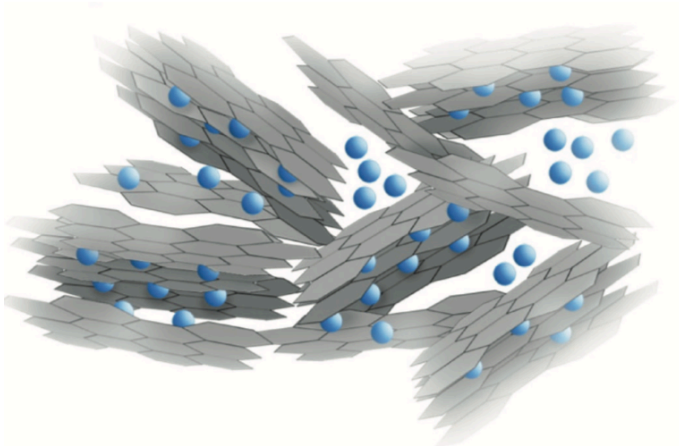

Figure 2.14 Sketched representation of the 'house of card' model for the insertion mechanism of Na+ into the structure of hard carbons. The Na+ ion storage occurs both between the graphene layers, as well as within the interstitial pores in the voids of the material structure [86].

Other than carbon anodes, sodium alloys have recently been deeply considered because of the high theoretical capacities. Several elements may alloy with sodium (*viz.*, P, Sb, Sn, Ge, and Pb). Among them, phosphorous at the fully sodiated state "Na_3P" has a striking theoretical capacity of 2596 mAh g^{-1}, substantially higher than that obtainable using pure carbon; however, it faces the drawbacks of a poor conductivity and large volume

modifications during cycling. Low potential metal oxides and layered transition metal oxides represent further research stream. While the former involve the deoxygenation of the active material particles during sodiation with the sub-sequent alloying reactions with the metal itself, the latter deal with the classical insertion mechanism and rely on the use of early transition metal like vanadium or titanium. For example, $Na_2Ti_3O_7$ shows a theoretical specific capacity of 200 mAh g^{-1} at the very appealing potential of 0.3 V vs. Na^+/Na, low enough for fabricating full cells providing high working voltage, but anyway high enough to avoid the dendritic growth of Na metal during sodiation. At last, a considerable attention is pointed to the nanostructure Ti_2O for its stability and non-toxicity.

2.8.3 Materials for the electrolyte system

The most widely used electrolyte systems are similar to those implemented in LIBs. They can be subdivided into aqueous and non-aqueous liquid electrolytes, ionic liquids, glass and ceramic electrolytes and, eventually, gel-polymer and solid-polymer electrolytes. Non-aqueous liquid electrolytes are composed of a mixture of organic solvent mostly based on carbonates (e.g., EC, PC, DMC, DEC or mixtures thereof) and a sodium salt such as $NaClO_4$, $NaPF_6$ or NaTFSI; Na_2SO_4 is instead dissolved in water in the case of aqueous liquid electrolytes [87]. For what concerns gel-polymer and solid-polymer electrolytes, the same materials already proposed for LIBs are attracting the interest of the scientific community, clearly exploiting sodium instead of lithium as ionic conductor.

3. Graphene as conductivity enhancer for $LiFePO_4$ cathodes

Chapter 3 illustrates the experimental activity carried out in the laboratory of the 'Group of Applied Materials and Electrochemistry' (Game Lab) at the Department of Applied Science and Technology (DISAT) of the Politecnico di Torino.

As detailed in the previous section, after the pioneering work of Padhi et al. [34] lithium iron phosphate is considered the best candidate among the polyanion compounds to act as cathode material for the actual generation of Li-ion batteries. Its intrinsic safety, ease of production, low cost and eco-friendliness of the precursor materials play an important role in the choice of this material. Moreover, $LiFePO_4$ exhibits a high theoretical capacity of 170 mAh g^{-1} and an attractive flat voltage profile vs specific capacity of 3.45 V vs Li^+/Li, which result in a relatively high theoretical specific energy of 580 Wh kg^{-1}. However, this material pays the price of low overall performances if compared to other cathode candidates, thereby limiting its further expansion in the rechargeable battery market. The reason of the low performances resides in the low electronic and ionic conductivity, which limits the exploitation of the full theoretical specific energy, particularly at high current regimes needed for high demanding applications. This thesis work points the attention to this limiting aspect, showing how the striking conductivity properties of graphene may improve the electronic conductivity and Li^+ ion diffusion characteristics of $LiFePO_4$.

For this reason, $LiFePO_4$ has been synthesized in the laboratory through hydrothermal synthesis, as already shown in literature [39], [40], and compared with a commercial $LiFePO_4$. All the materials have been prepared in the form of test electrodes, which have been deposited on aluminium foils in order to be electrochemically characterized by means of cyclic voltammetry and galvanostatic cycling techniques[4]. The purpose of this experimental activity was to analyse how the addition of graphene, in the form of graphene oxide (GO) or reduced graphene oxide (rGO), as conductivity enhancer during the electrode preparation step can improve the performance at high C-rates of the cathode materials.

[4] Cyclic voltammetry and galvanostatic cycling are two standard electrochemical techniques for the evaluation of the electrochemical performances of a material in terms of working potential, current rate and specific capacity. An explanation of their basic principles is provided in **APPENDIX II**.

3.1 Materials and Methods

3.1.1 Hydrothermal synthesis of nanostructured $LiFePO_4$

Lithium iron phosphate ($LiFePO_4$, LFP) can be prepared with different synthetic route, among them the mild hydrothermal synthesis in the presence of a carbonaceous surfactant is a practical, low energy consumption, low cost and easily scalable process, which has been reported to produce high performing lithium iron phosphate with nanosized carbon-coated particles [39]. The addition of a carbonaceous surfactant has been demonstrated to prevent the oxidation of Fe^{2+} to Fe^{3+} during the firing stage following the synthesis and increase the conductivity of the material. The former advantage is fundamental because the oxidation reaction of iron corresponds to the charge process of a Li-ion cell with $LiFePO_4$ as cathode material, therefore a premature oxidation during synthesis leads to a great loss of electrochemical activity in the material. The increase in conductivity is, instead, achieved because the surfactant limits the growth of large particles, thereby enlarging the specific surface area, and produces a thin carbon coat during the pyrolysis process, which enhance both the intra- and inter- particle conductivity [39]. The starting precursors are:

- $FeSO_4 \cdot 7H_2O$ (*Sigma-Aldrich*, 99%+);
- H_3PO_4 (*Sigma-Aldrich,*99%+)
- LiOH (*Emsure*, 98%+)
- hexadecyltrimethylammonium bromide ($C_{19}H_{42}BrN$, CTAB, *Sigma-Aldrich*, 99%+)

Two samples are prepared, the first (LFP-STD) is synthesized in a pure water solution, whereas the second (LFP-OH) differs for the addition of ethanol as co-solvent.
Firstly, the carbonaceous surfactant CTAB is completely dissolved in double distilled water (*Milli-Q*) under constant mild stirring for approximately 1 h in a Teflon bottle (in the case of the sample LFP-OH, the surfactant is dissolved in a mixed water and ethanol solution with weight ratio water-alcohol of 50:50). A $FeSO_4 \cdot 7H_2O$ and a H_3PO_4 water solution are prepared, separately, and then mixed with the dissolved CTAB. Only at the end, when $FeSO_4$ is completely dissolved, a LiOH water solution is added[5]. The mixture is vigorously stirred for 1 minute and heated at 120 °C for 5 hours. The molar ratio of $FeSO_4 \cdot 7H_2O$, H_3PO_4 and LiOH is 1:1:3. After the heating process, the Teflon bottle is cooled down to ambient temperature and the resulting green precipitate washed with double distilled water and filtered to

[5] The addition of LiOH at the final stage of the mixture is important to avoid the formation of $Fe(OH)_2$, which can be easily oxidized to Fe^{3+}.

completely eliminate the excess of surfactant. The so-obtained green amorphous compound is then dried overnight at room temperature and hand-mortared to fine powder. Eventually, the powder is fired at 600 °C[6] under pure N_2 inert flux for 12 h in a *Carbolite Split Tube Furnace* (*Model VST 12/300*). The heat treatment is necessary to obtain the crystalline phase and to form the thin carbon film that homogeneously covers the grains, thus optimising the electrochemical response at high current regimes.

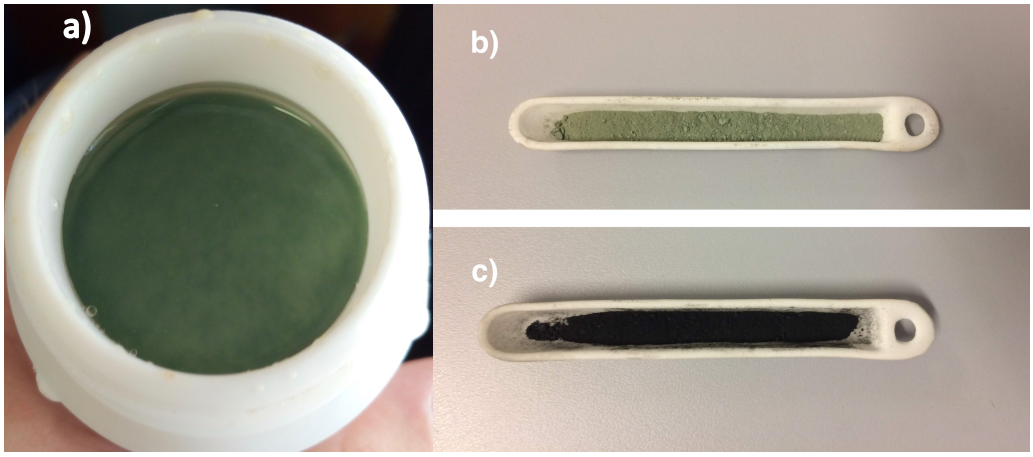

Figure 3.1 Different steps of the hydrothermal synthesis of $LiFePO_4$: green water solution after 5h at 120 °C (a), precursor $LiFePO_4$ powder after the removal of the excess of surfactant, (c) $LiFePO_4$ after the heat treatment at 600 °C under inert (N_2) flux.

3.1.2 Electrode preparation and cell assembly

This section illustrates the electrode preparation and the test cell assembly procedures carried out in this experimental thesis work. During these steps, LFP-STD is prepared with and without addition of graphene oxide as conductivity enhancer, thus resulting in two different electrodes: LFP-STD and LFP-STD-GO. Therefore, from now on, LFP-STD will be the hydrothermally synthesized lithium iron phosphate without alcohol and without graphene oxide, whereas LFP-STD-GO will be the same hydrothermal synthesized active material with the addition of graphene oxide during the preparation of the electrodes. The LFP-OH electrode is prepared with the same procedure and it does not contain graphene oxide.
Carbon black (*Alfa Aesar*) as basic conductivity enhancer is firstly hand-mortared with the active material powder to obtain a uniform dispersion among the active particles (in the

[6] In particular, the powder is firstly exposed to a 7 °C min^{-1} heating rate from ambient temperature to 600 °C, then the temperature remained constant for 12 °C and, eventually, the sample is cooled to room temperature without any imposed cooling rate.

case of LFP-STD-GO, graphene oxide is hand-mortared with carbon black and the active material). Secondly, the obtained mixture is transferred in glass vessel adding a precise amount of poly(vinylidene fluoride) (PVdF, *Sigma-Aldrich*) as binder. N-methyl-2-pyrrolidone (NMP, *Sigma-Aldrich*) solvent is added and the viscous mixtures is slowly stirred for at least 5 hours in order to form a homogeneous slurry. The three different slurries (LFP-STD, LFP-OH and LFP-STD-GO) exhibit the weight percentages summarized in **Table 3.1**.

Weight %	LFP-STD	LFP-OH	LFP-STD-GO
Active material	70	70	70
Carbon Black	20	20	16
GO	-	-	4
PvDF	10	10	10

Table 3.1 Weight percentages of the slurry's components for the electrode preparation of the three samples LFP-STD, LFP-OH, LFP-STD-GO.

Each slurry is then cast on an aluminium foil by the '*doctor blade*' technique. The 'doctor blade' is a blade of adjustable height that can slide horizontally to evenly spread the slurry on the Al foil. After evaporating the solvent overnight, disks of 1 cm are punched out and dried for 12 h at 120 °C under high dynamic vacuum in a B*ü*chi chamber (*Model B-585*) (**Figure 3.2**).

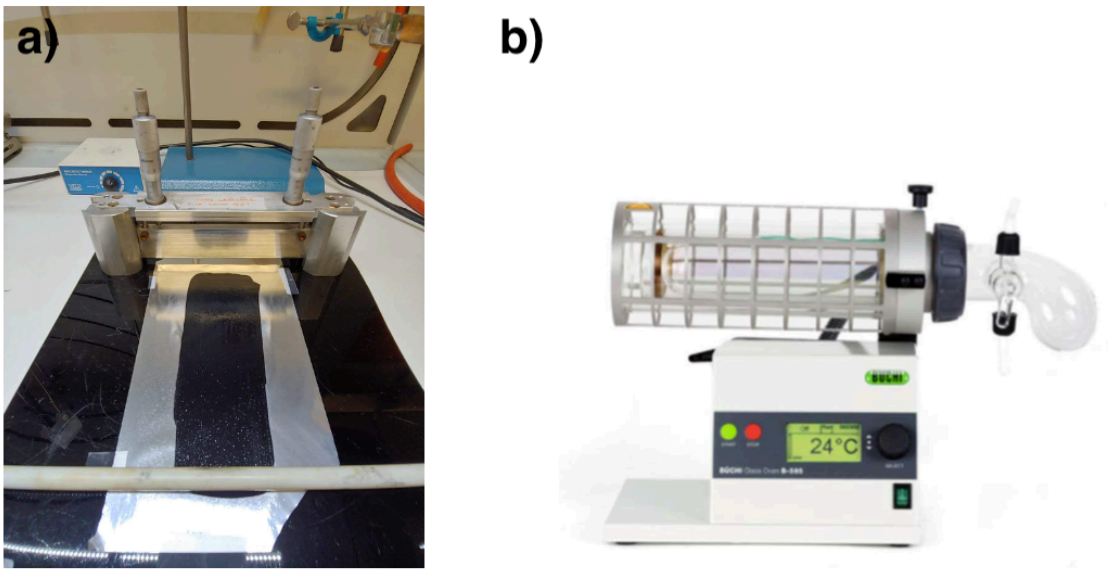

Figure 3.2 Electrode slurry spread on Al foil with the 'doctor blade' (a). B*ü*chi chamber (model B-585) for vacuum drying (b).

For the electrochemical tests, the disks are transferred in a dry-room environment (a room with low humidity atmosphere, 10m2, R.H. <2% ± 1 at 20 °C, Soimar Group) and the active material is weighted by subtraction of the weight of the Al foil. Eventually, the electrodes are assembled in standard three electrodes T-type test cell (see **Figure.3.3**) composed of a main polyethylene T-shaped body in which three 304 stainless-steel cylinders with a diameter of 10 mm can be inserted.

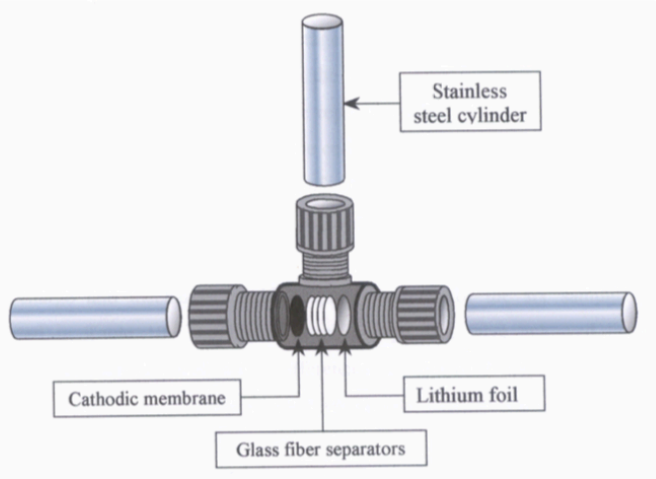

Figure 3.3 Schematic picture of a three electrodes T-cell. [5]

The T-cells are assembled in the dry-room environment as follows. One of the stainless-steel cylinders is inserted through a hole of the central body and tightened with a threaded ring. From the opposite hole the working electrode (Al foil coated with the cathode material) is carefully inserted and stuck on the top of the cylinder. Two glass microfiber separators (*Whatman*) are adjusted over the cathode disk and wet with few droplets of electrolyte (1 M $LiPF_6$ solution in 1:1 mixture of carbonate (EC) and diethyl carbonate (DEC)). A high purity lithium foil (counter electrode) is pressed on the top of the second stainless-steel cylinder and inserted in the second hole to finish the sequence cathode-separator-anode as shown in **Figure 3.3**. After tightening the second cylinder with a treaded ring, an excess of electrolyte is poured inside the third central hole. Eventually, also the third cylinder is inserted and tightened (for cyclic voltammetry tests, a second Li metal disk is attached on top of the third cylinder acting as reference electrode). The cell is sealed with Parafilm® tape to avoid air infiltration and transferred outside the dry-room for the electrochemical measurements.

3.2 Structural and electrochemical characterization of the sample LFP-STD

This section reports the structural and electrochemical characterization of $LiFePO_4$, hydrothermally synthesized in pure doubly distilled water, namely sample LFP-STD. First, the structural analysis by X-ray diffraction is carried out, which is fundamental to confirm the successful synthesis of the crystalline $LiFePO_4$ material having the expected orthorhombic crystal structure. Then, the sample is tested for its electrochemical behaviour by the galvanostatic cycling and cyclic voltammetry techniques.

3.2.1 Structural characterization by X-ray powder diffraction

X-ray powder diffraction (XRPD)[7] patterns were recorded on an X'Pert MPD DY 1165 diffractometer equipped with Cu Kα radiation source in order to confirm the formation of the olivine-type $LiFePO_4$ structure of sample LFP-STD. The diffraction data were collected in the 2θ range of 10-70° with intermittent step of 0.02°.

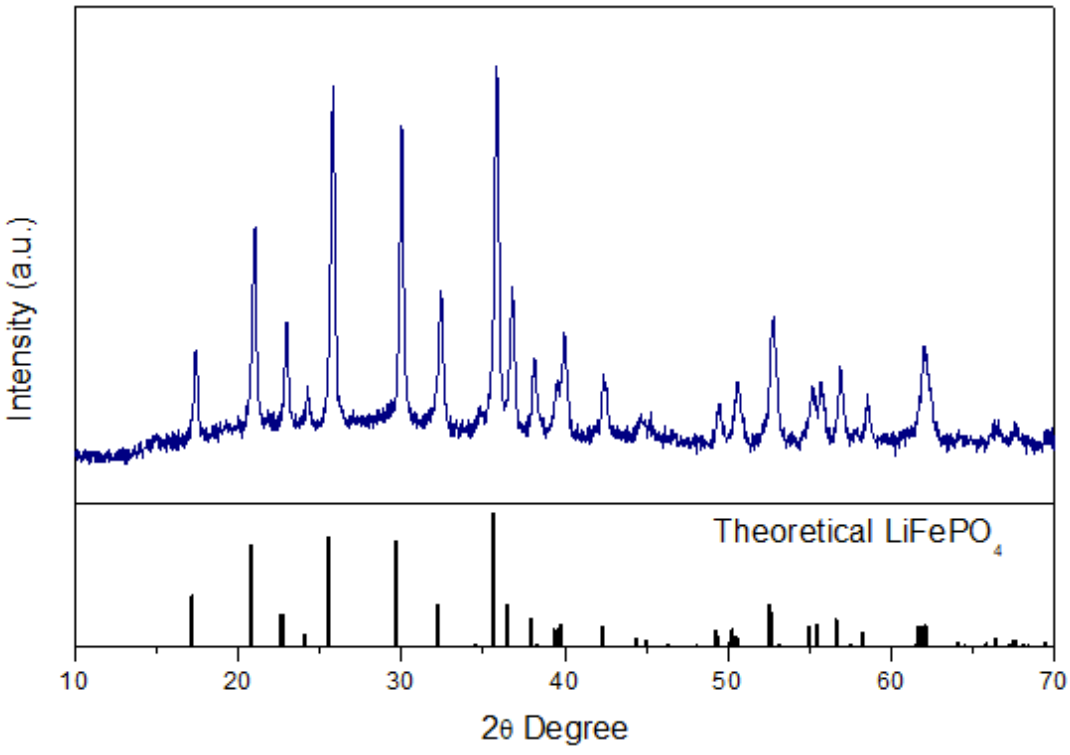

Figure 3.4 XRPD diffraction pattern of sample LFP-STD.

[7] **Appendix I.I** provides a detailed explanation of the X-ray diffraction technique.

The diffraction profile shown in **Figure 3.4** confirms the expected orthorhombic olivine-type crystal system featuring a '*Pmnb'* space group, as it can be easily deduced from the main diffraction peaks characteristics of $LiFePO_4$ that correspond to the reference $LiFePO_4$ pattern (see the black lines in Figure 3.4). The synthesis process involved the decomposition of the organic species forming the carbonaceous surfactant (CTAB) during the firing stage at 600 °C under inert N_2 flux. No evidence of a crystalline carbonaceous phase appears in the diffraction pattern, neither in the amorphous phase. The reason may reside either in the marginal presence of the formed carbon or in the very small thickness of the formed carbon layer on the nanosized $LiFePO_4$ particles.

3.2.2 Electrochemical characterization: cyclic voltammetry and galvanostatic cycling

This section illustrates the electrochemical results of the sample LFP-STD, which has been hydrothermally synthesized in pure doubly distilled water solution as described in **Chapter 3.1.1** and prepared for the electrochemical tests in a T-type cell according to the procedure detailed in **Chapter 3.1.2**. It is worth analysing the electrochemical results of this sample because it represents the reference sample for the understanding of the results and discussions in the following chapters. The sample has been characterised by means of galvanostatic cycling and cyclic voltammetry (see **Appendix II**). Briefly, the galvanostatic cycling regards the application of a direct and constant current that allows the evaluation of the working potential of the cell and the amount of charge passing through to circuit at every charge and discharge cycle. It is carried out at room temperature in a three electrode T-cell with LFP-STD as working electrode, lithium metal as counter electrode and 1 M $LiPF_6$ in 1:1 EC:DEC solution as electrolyte. The cut-off voltages are set to 2.8 and 4 V vs Li^+/Li, while the galvanostatic charge and discharge current regimes range from C/20 to 50C rates. The cyclic voltammetry, instead, is a technique in which a scan of the potential from a lower to an upper cut-off voltage (and viceversa) is performed and the current delivered during the electrochemical processes at specific voltage values is recorded. It is carried out at room temperature in a three electrode T-cell with lithium metal as both counter and the reference electrodes. The scan of the potential is set between 2.8 and 4 V vs Li^+/Li with a scan rate of 0.1 mV s^{-1} for ten consecutive cycles.

Cyclic voltammetry

Figure. 3.5 shows the cyclic voltammetry of the sample LFP-STD. The scan of the voltage starts at the V_{oc} and moves towards increasing (more anodic) potential values (upper side

of the graph). A specific current peak, anodic, appears in the graph at about 3.52 V vs Li^+/Li, ascribing to the extraction of Li^+ ions from the orthorhombic lithium iron phosphate structure with the concurrent oxidation of Fe^{2+} to Fe^{3+}. Once the upper cut-off limit is reached, the scan is reversed and a second peak, cathodic, is recorded at about 3.33 V vs Li^+/Li. This second peak accounts for the re-insertion of Li^+ ions into the $FePO_4$ structure with the corresponding reduction of Fe^{3+} to Fe^{2+}. The presence of the main peaks with a mid-point potential of 3.42 V and the concurrent absence of other signals in the plot confirm the purity of the sample in which only the characteristic extraction and insertion of Li^+ ions in LFP occur.

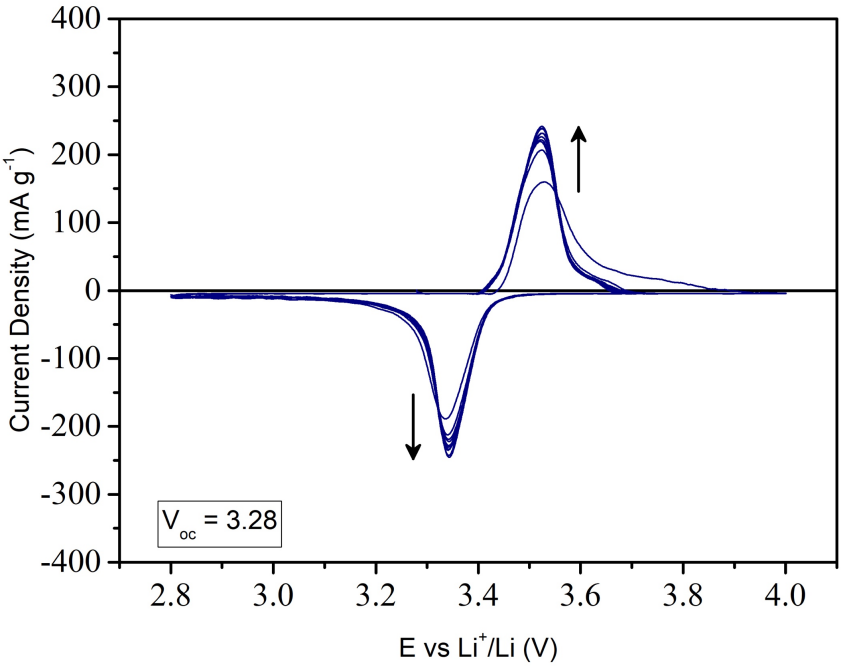

Figure 3.5 Cyclic voltammetry (1st to 10th cycle) of the sample LFP-STD at ambient laboratory temperature. Scan rate 0.1 mV s. Voltage range 2.8-4 V. vs. Li^+/Li.

Moreover, the outstanding reversibility of the electrochemical process is demonstrated by the fact that the cathodic peak is always slightly greater than the previous anodic one, thus leading to an increase of the peak intensity with the ongoing of the cycles. During the electrochemical process, the material structure is subjected to a volume expansion/contraction of about 7 % [78], correspondingly to the insertion/de-insertion of Li^+ ions. The peculiarity of the first cycle, which behaves evidently different from the following ones, is likely linked the volumetric change of the material structure that, for the first time, undergoes the lithium de-insertion. From the second cycle onwards, the structure

has already endured the shock of the electrochemical process and the overall process becomes well reversible. It can be noticed the increase and the reciprocal approach of the anodic and cathodic peaks to the mid-point voltage with the ongoing of the cycles, which is a further evidence of the good reversibility of the process. The electrochemical process described is in accordance with the typical behavior reported in literature [88]–[90].

Galvanostatic cycling at low C-rates

The galvanostatic cycling of the sample LFP-STD at low C-rates (from C/20 to 1C) is shown in the figures below. **Figure 3.6** shows the characteristic charge/discharge flat voltage profiles over specific capacity given by the two-phase Li^+ ions extraction and insertion mechanism in which a $LiFePO_4/FePO_4$ interface appears based on the following reaction:

$$LiFePO_4 \leftrightarrow Li_{1-x}FePO_4 + xFePO_4 + xLi^+ + xe^- \quad (3.1)$$

The working potential during discharge at C/20 and C/10 is about 3.42 V vs Li^+/Li, close to the theoretical value of 3.45 V; the overpotential increases at higher C-rates (> 3.53 V vs Li^+/Li at 1C rate), but overall the electrochemical response is good accounting for a sufficient electronic conductivity at low-medium current densities.

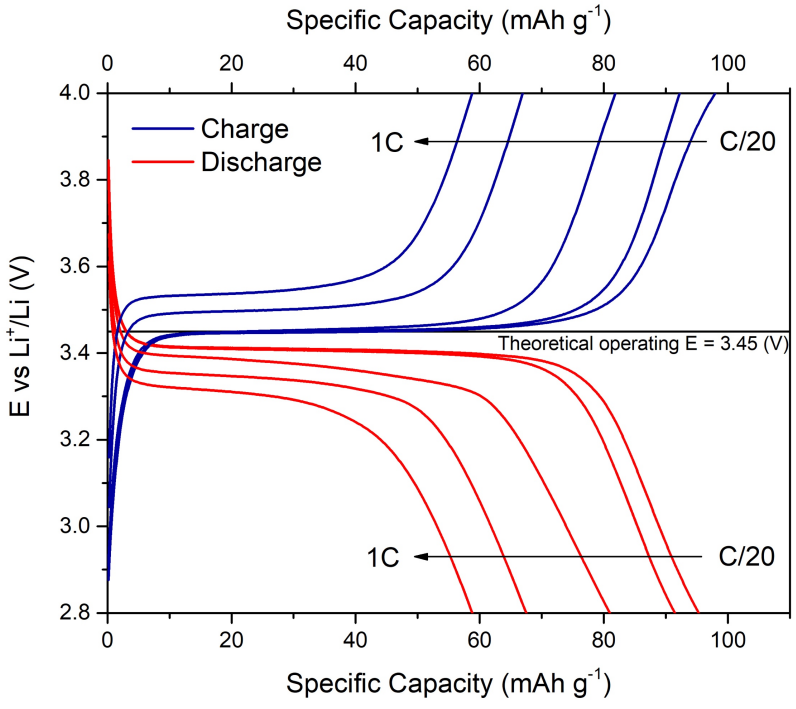

Figure 3.6 Charge/discharge potential vs. specific capacity at low C-rates of the sample LFP-STD, cycled from C/20 to 1C at ambient laboratory temperature.

Figure 3.7 shows the cyclic performance of the sample. The remarkable reversibility of the electrochemical process, already observed by the cyclic voltammetry, is confirmed by the high values of coulombic efficiency[8], which ranges from 97% at C/20 to 99% at 1C. The overall electrochemical performance in terms of specific capacity output is rather limited, about 98 mAh g^{-1} during charge (96 mAh g^{-1} in discharge) at C/20, but it is well retained when passing at C/10; slightly higher decrease in the performance is observed when increasing the C-rate to higher values (as already seen in **Figure 3.6** with the overpotential in discharge increasing at above C/5). At high current regimes, diffusion problems likely arise during the extraction of Li^+ from the host structure, leading to a drop of the specific capacity at about 60 mAh g^{-1} at 1C, which is nonetheless very much stable upon cycling.

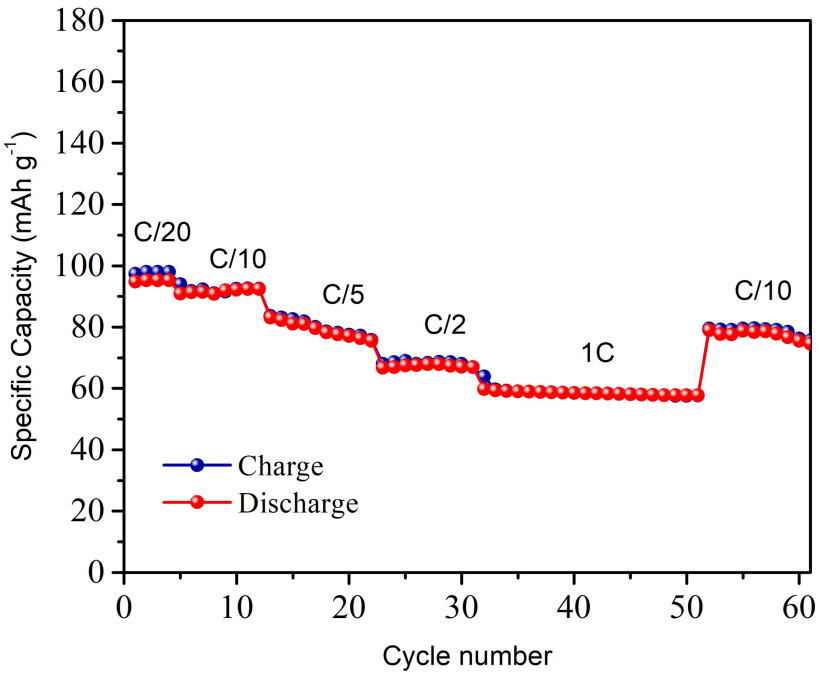

Figure 3.7 Cycling performance at low C-rates of the sample LFP-STD, cycled from C/20 to 1C at ambient laboratory temperature.

The reasons of the limited diffusion process might be a non-uniform particle size and/or an imperfect formation of the thin carbon-coating layer during the synthesis process and, in particular, the following annealing step. Indeed, literature reports that Li^+ ions straggle to diffuse within particles having larger diameter, thus the portion of the material in the bulk

[8] As a reminder, the coulombic efficiency is the percentage ratio of the capacity delivered during discharge over the capacity accumulated in the charge step of the cell.

of the active particles cannot be properly participate in the redox process and, therefore, contributes very little to the electrochemical performance, resulting in the uncomplete extraction of Li^+ ions from the structure.

Galvanostatic cycling at high C-rates

The galvanostatic cycling of LFP-STD at high C-rates (from 1C to 50C) is performed in order to assess the rate capability of the sample, *viz.* the limit at which this material still undergoes reversible electrochemical activity. The results are shown in the figures below (recorded on freshly assembled cells).

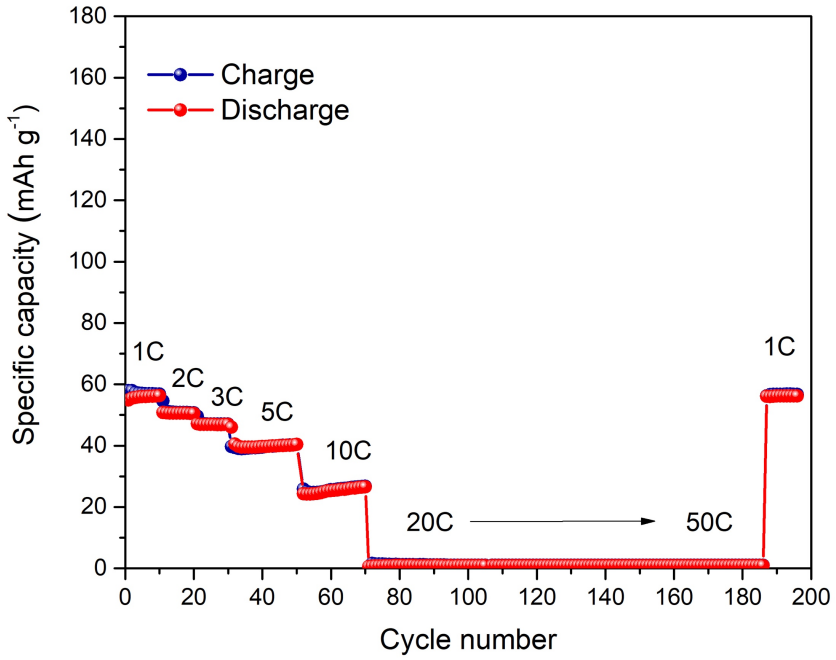

Figure 3.8 Cycling performance at high C-rates of the sample LFP-STD, cycled from 1C to 50C at ambient laboratory temperature.

Although the rather limited performances, the sample LFP-STD still exhibits electrochemical activity up to 10C rate (see **Figure 3.8**) with outstanding reversibility and stable capacity at each of the tested current regimes. The coulombic efficiency, indeed, is 94 % at the first cycle and increases up to almost 99% after the fifteenth cycle. The initial lower value can be easily explained by the fact that the structure undergoing the extraction and insertion of Li^+ ions has to adapt to the 'shock' of the consequent volume contraction and expansion under the already quite high current regime of 1C, therefore the discharge capacity is initially low and increases after few cycles. At C-rates higher than 10C, the active material cannot

withstand reversible Li+ ions intercalation and the cell capacity output decay to zero. Nonetheless, this is not at all indication of cell failure; indeed, when the current is again decreased to 1C, the full initial capacity is recovered, which confirms that the material structure has not been damaged by the high current and the reason for the absence of any electrochemical process resides in the low electronic conductivity of the material and too low Li^+ ions diffusion. Concerning the voltage vs specific capacity profiles (**Figure 3.9**), the characteristic flatness of the plateaus is recorded up to 3C rate, while at 5C and higher a smooth sloping plateau is observed accounting for the high diffusion resistance. Concordantly to **Figure 3.8**, no voltage profiles are recorded from 20 C.

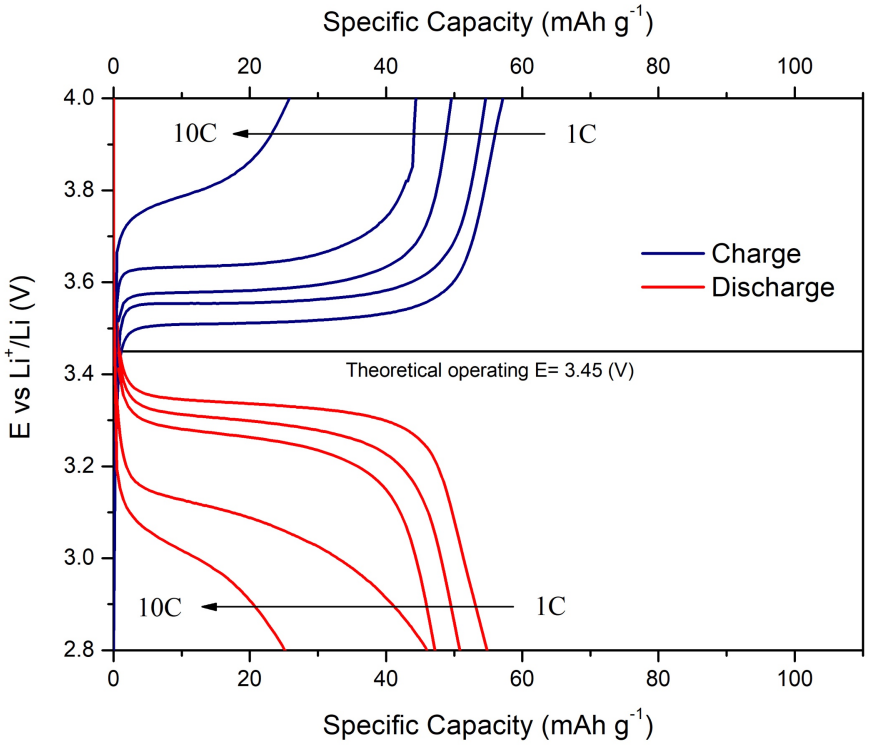

Figure 3.9 Charge/discharge potential vs. specific capacity at high C-rates of the sample LFP-STD, cycled from 1C to 50C at ambient laboratory temperature.

3.3 Comparison of the electrochemical behaviour of samples LFP-STD and LFP-OH: the influence of ethanol on the C-rate

This section compares the electrochemical results of the two samples hydrothermally synthesized in two different solvents. In the case of LFP-STD, pure doubly distilled water solution has been used, while LFP-OH has been synthesized in a mixed ethanol/water

solution. The introduction of ethyl alcohol in the synthesis process has been already reported to influence the micellar structure of the surfactant (CTAB), leading to remarkable structural-morphological differences and to improved electrochemical performances at very high C-rates [40].

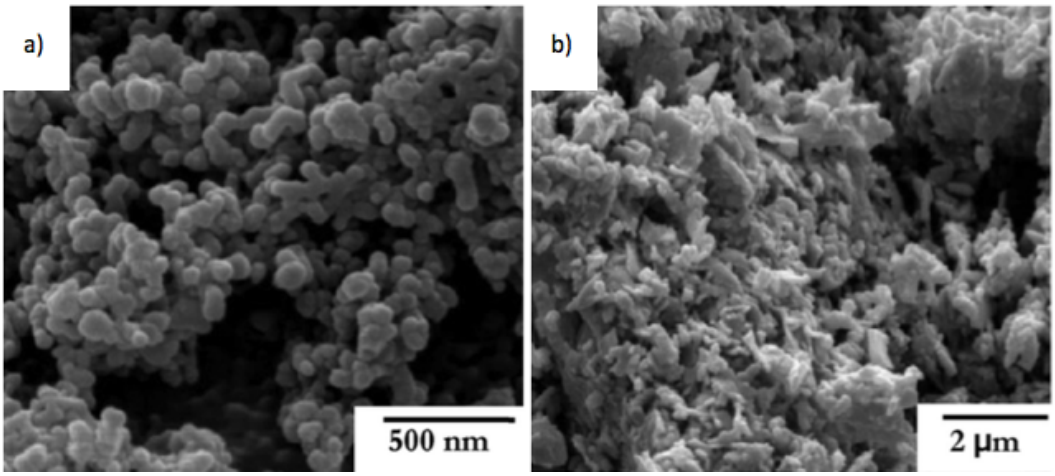

Figure 3.10 SEM micrographs of two typical lithium iron phosphate samples hydrothermally synthesized in pure water (a) and mixed ethanol/water (b) solution [40] .

The SEM images of **Figure 3.10** show the effect of the co-solvent in the morphology of the $LiFePO_4$ nanoparticles as reported in literature. The ethyl alcohol promotes a leaf-like particle growth (**Figure 3.10b**), rather than a more circular shape (**Figure 4.10a**), and leads to the formation of a carbon coating having higher homogeneity. As a consequence, better performances due to an improved ionic diffusion are expected to be observed at very high C-rates.

Cyclic voltammetry

Figure 3.11 compares the 10^{th} voltammetric cycles of the two samples (LFP-STD and LFP-OH) performed at ambient laboratory temperature between the voltage range 2.8-4 V vs Li^+/Li and a scan rate of 0.1 mV s^{-1}. The effect of the addition of ethanol is clearly visible by two distinctive modifications of the CV profiles. First, the peak intensity (i.e., the maximum current density value recorded during the potential scan) largely increases (360 mAh g^{-1} for the anodic peak of LFP-OH compared to the 245 mAh g^{-1} of the sample LFP-STD), meaning a remarkable enhancement in the electrochemical activity associated with the Li^+ diffusion and the Fe^{2+}/Fe^{3+} redox process. Moreover, LFP-OH exhibits sharper reduction/oxidation

peaks, indicating that Li^+ ion diffusion is facilitated within the active material particles, and the overall electrochemical kinetics is largely improved.

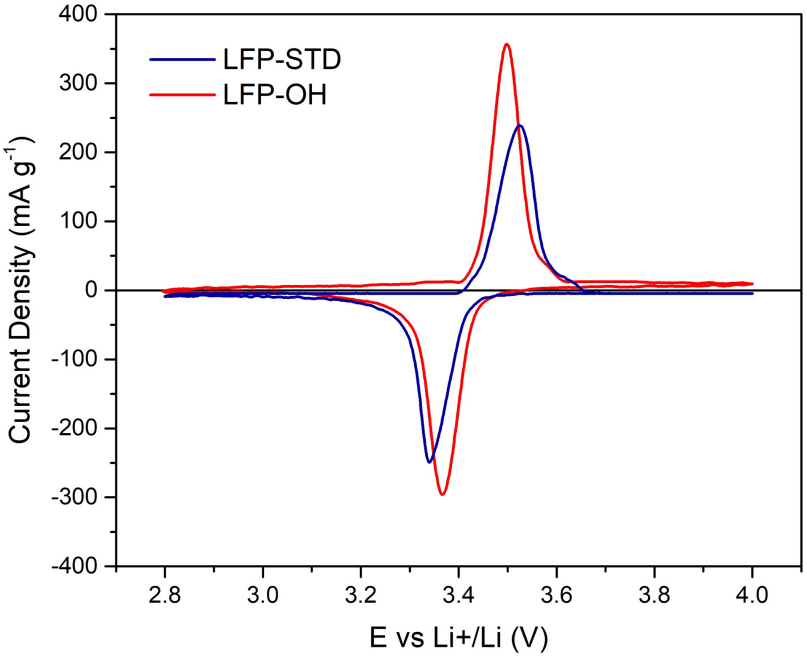

Figure 3.11 Comparison between the 10th voltammetry cycles of the samples LFP-STD and LFP-OH at ambient laboratory temperature. Scan rate 0.1 mV s. Voltage range 2.8-4 V vs. Li+/Li.

Galvanostatic cycling at high C-rates

According to the improvements of the electrochemical process at very high C-rates reported in literature because of the addition of ethanol during synthesis [40], it is worth comparing the galvanostatic cycling tests performed on the two samples only at high C-rates above 1C. The galvanostatic cycling behavior (**Figure 3.12**) of LFP-OH is evidently improved with respect to LFP-STD, showing a quite impressive value of specific capacity of about 80 mAh g^{-1} at 10C rate in discharge. In particular, it is important to underline that the sample LFP-OH exhibits electrochemical activity until the very high 30C rate with an average specific capacity of about 13 mAh g^{-1} in discharge and a coulombic efficiency ranging always higher than 99%, even approaching 100% at very high C-rate. In addition, the capacity retention when the current regime is increased, namely the rate capability, is similar between the two samples until the 5C rate. On the contrary, when passing to the 10C rate, the LFP-OH sample outperforms LFP-STD, with a much better capacity retention.

The comparison of the galvanostatic charge/discharge potential versus specific capacity profiles of the samples at 1C (**Figure 3.13)**, 5C (**Figure 3.14)** and 10C (**Figure 3.15**) are also

reported. The curves, extracted from the cycling test carried out at increasing C-rates, demonstrates the superior performances of LFP-OH, which exhibits reduced overpotential and an extended flat voltage plateau even at high 10C rate.

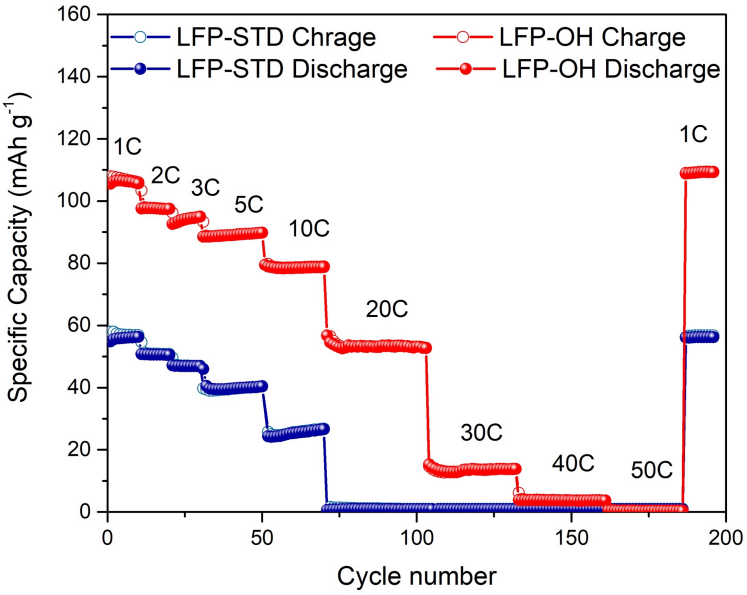

Figure 3.12 Comparison of the cycling performance at high C-rates of the samples LFP-STD and LFP-OH, cycled from 1C to 50C at ambient laboratory temperature.

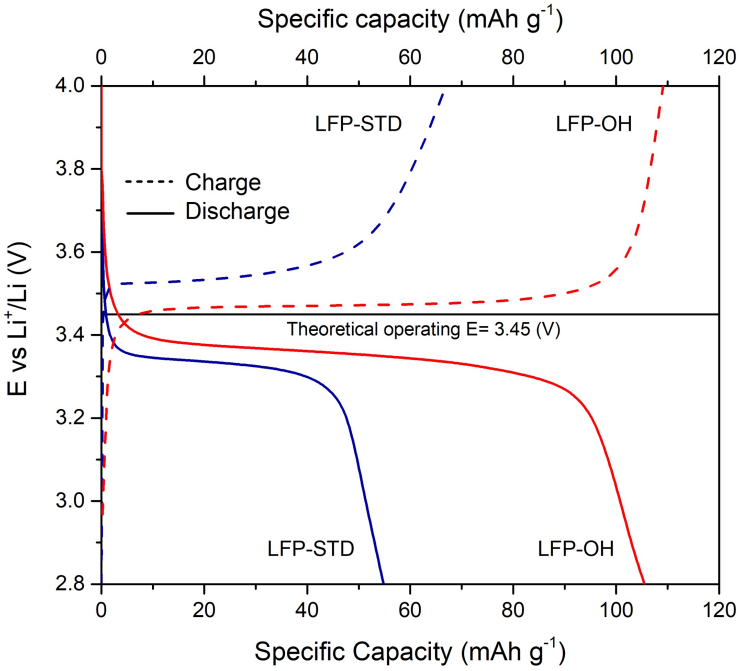

Figure 3.13 Comparison of the charge/discharge profiles of the samples LFP-STD and LFP-OH at 1C rate. Cycles extracted from cycling tests carried out at increasing C-rates at ambient laboratory temperature.

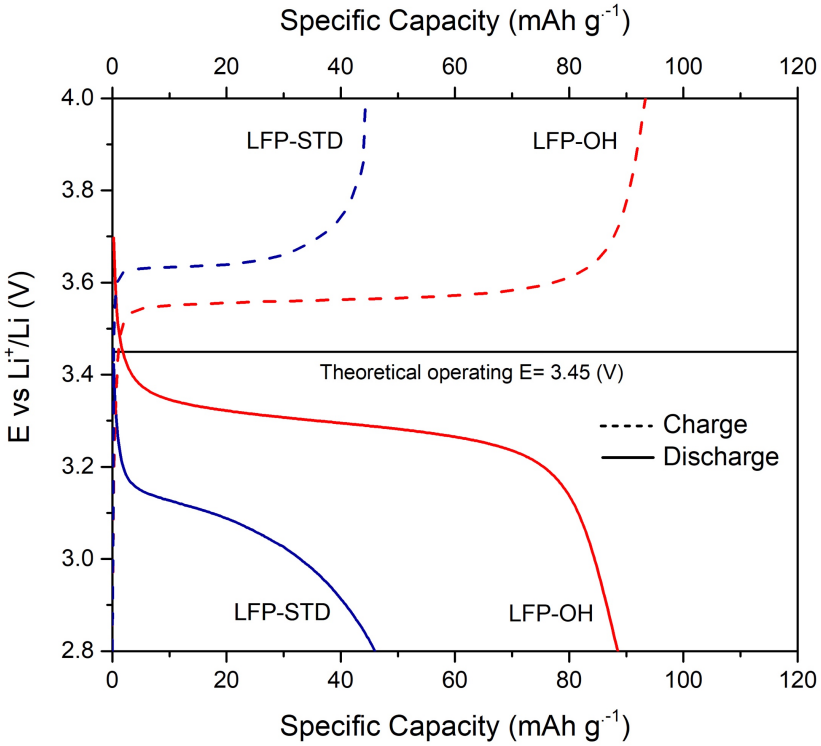

Figure 3.14 Comparison of the charge/discharge profiles of the samples LFP-STD and LFP-OH at 5C rate. Cycles extracted from cycling tests carried out at increasing C-rates at ambient laboratory temperature.

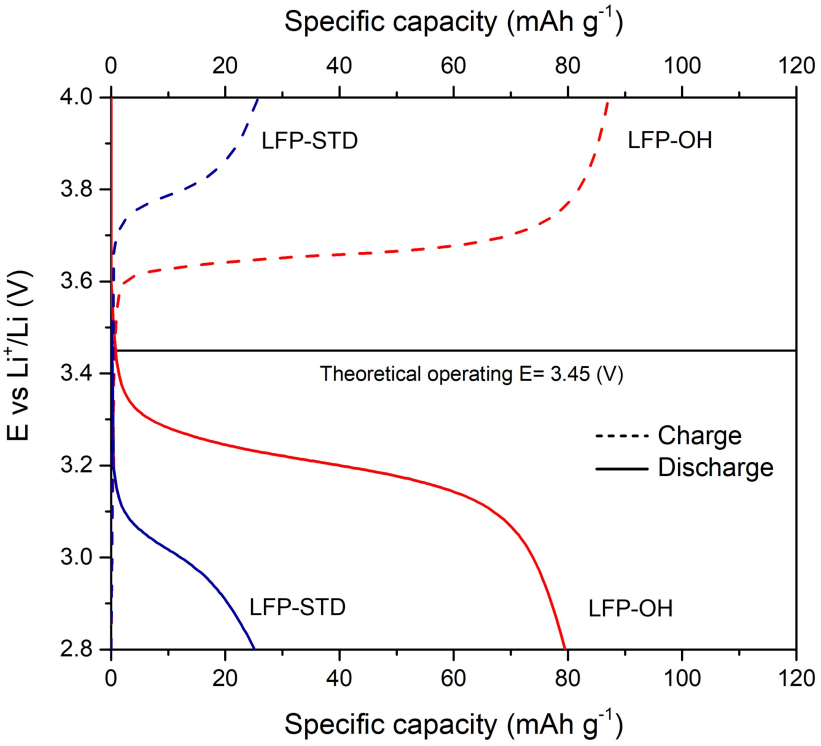

Figure 3.15 Comparison of the charge/discharge profiles of the samples LFP-STD and LFP-OH at 10C rate. Cycles extracted from cycling tests carried out at increasing C-rates at ambient laboratory temperature.

3.4 Comparison of the electrochemical behaviour of samples LFP-STD and LFP-OH: the influence of graphene oxide at high current densities

As detailed in Chapter 2, extended research on graphene showed the striking electronic properties of this material. The aim of this section is to illustrate the effect of graphene oxide as conductivity enhancer for the hydrothermally synthesized lithium iron phosphate in pure water solvent. A slight addition of graphene oxide during the electrode preparation process (as detailed in **paragraph 3.1.2**) is expected to boost the electronic conductivity of the sample LFP-STD, providing an alternative path to the addition of ethanol during the synthesis process for the increase in performances of $LiFePO_4$. As a reminder, **Table 3.2** reports the slurry composition of the two electrodes under study obtained with (LFP-STD) and without (LFP-STD-GO) addition of GO.

Weight %	LFP-STD	LFP-STD-GO
Active material	70	70
Carbon Black	20	16
GO	-	4
PvDF	10	10

Table 3.2 Weight percentage of the components of the slurries for the electrode preparation of the two samples LFP-STD and LFP-STD-GO.

Cyclic voltammetry

Figure 3.16 compares the 10th voltammetric cycles of the two electrodes, which have been performed at ambient laboratory temperature in the voltage range 2.8-4 V vs Li^+/Li and a scan rate of 0.1 mV s^{-1}. The current per unit mass delivered by the cell is nearly doubled with the addition of 4% of graphene oxide (GO) in the electrode mixture, meaning a consistent extension in the electrochemical activity associated with the Li^+ diffusion and the Fe^{2+}/Fe^{3+} redox process. Moreover, the sample LFP-STD-GO exhibits slightly sharper peaks, indicating a faster ion extraction and insertion kinetics.

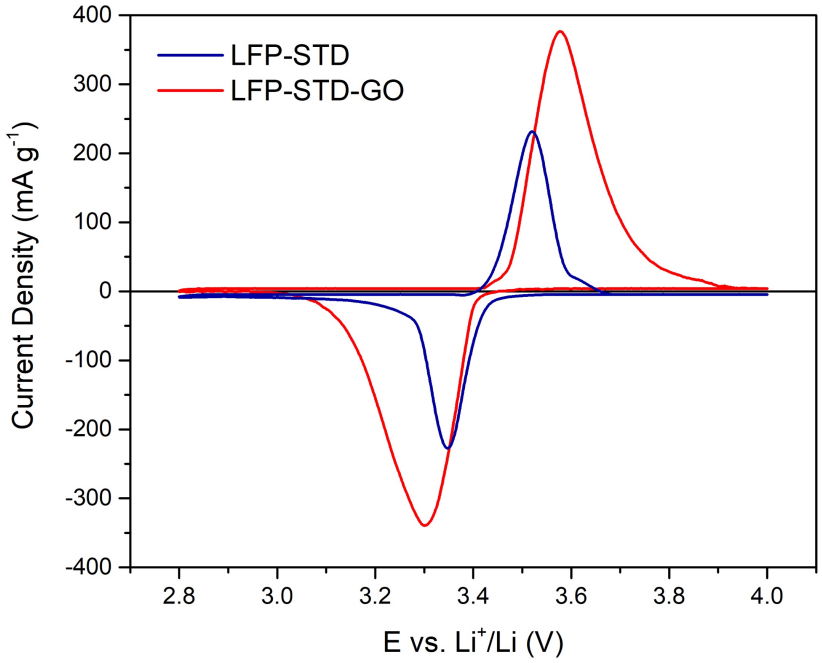

Figure 3.16 Comparison between the 10th voltammetry cycles of the samples LFP-STD and LFP-STD-GO at ambient laboratory temperature. Scan rate 0.1 mV s. Voltage range 2.8-4 V vs. Li^+/Li.

Galvanostatic cycling at high C-rates

As previously shown in **Figure 3.8**, the galvanostatic cycling tests at high C-rates proved that the hydrothermally synthesized LFP-STD cannot reversibly operate under elevated current regimes. Therefore, it is interesting to see if the addition of the electronic conductive GO can improve the diffusion properties of the active material, allowing to withstand more severe operational conditions. The results of the galvanostatic cycling (**Figure 3.17**) show striking features and the impact of GO on the electrochemistry of LFP is clearly evident; although the overall specific capacity is still rather low and LFP-STD shows better performances up to 5C rate, LFP-STD-GO exhibits the expected enhancement in the electrochemical activity at C-rates higher than 10C. In particular, an increase of the specific capacity is observed already at 10C rate, but the remarkable effect is observed from 20C to 50C (24 mAh g^{-1} at 20C and 9 mAh g^{-1} at 50 C in discharge for LFP-STD-GO) with the coulombic efficiency being always stable at above 99%. Apart from the specific capacity values, the fundamental point to underline is that excellent electronic and ionic conductivities are mandatory for an electrode material to reach such an ultrafast rate capability and, in this respect, the addition of GO greatly contributes to the performance of the active material where diffusion processes are limited by the stressful operating conditions, particularly at very high C-rates.

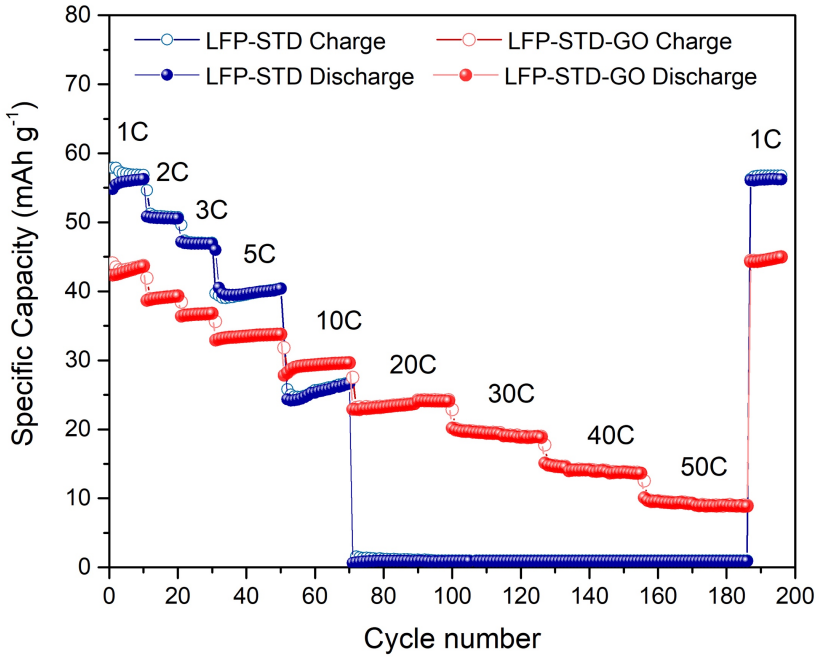

Figure 3.17 Comparison of the cycling performance at high C-rates of the samples LFP-STD and LFP-STD-GO, cycled from 1C to 50C at ambient laboratory temperature.

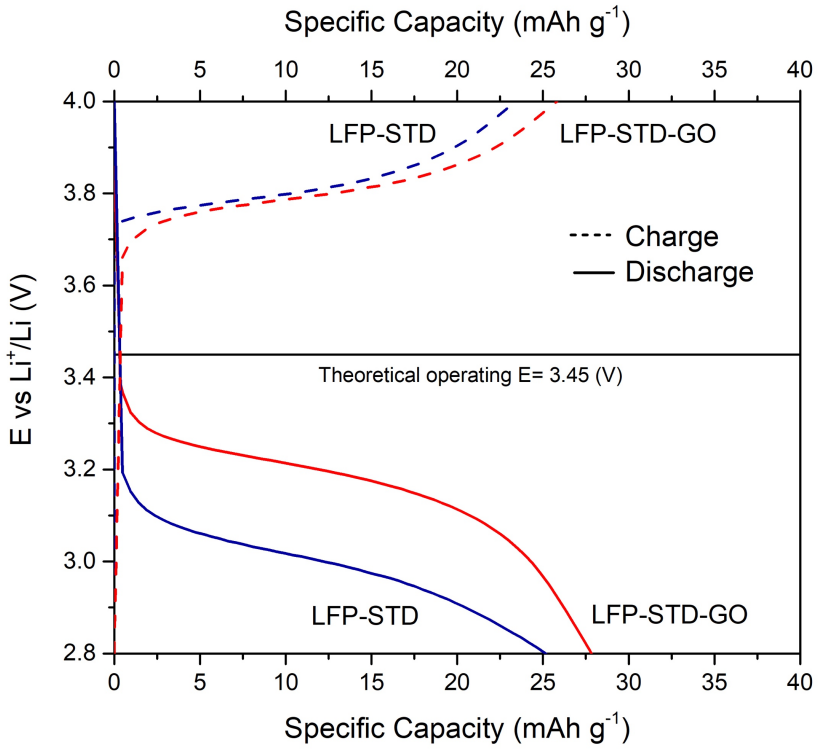

Figure 3.18 Comparison of the charge/discharge profiles of the samples LFP-STD and LFP-STD-GO at 10C rate. Cycles extracted from cycling tests carried out at increasing C-rates at ambient laboratory temperature.

Figure 3.18 reports the voltage profiles versus specific capacity at 10C of the two samples and confirms the results illustrated in **Figure 3.17**. In particular the discharge voltage profile of LFP-STD-GO shows a consistent reduction of the overpotential.

3.5 Electrochemical analysis of a hydrothermal $LiFePO_4$ optimized for high capacities.

As previously discussed, the addition of ethanol as co-solvent during the hydrothermal synthesis process of $LiFePO_4$ positively affected the performance of this cathode material at high C-rates. Moreover, I proposed the addition of graphene oxide as conductivity enhancer to increase the diffusion properties of the active material. The results demonstrated a substantial increase in capacity due to the addition of ethanol that influences the structure of the nanosized $LiFePO_4$, whereas the addition of GO accounts for an ultrafast rate capability, allowing the electrochemical diffusion of Li^+ within the active particles even under highly severe operating conditions. At this point, it is interesting to see if the addition of graphene leads to any improvements on a hydrothermal $LiFePO_4$ cathode, industrially optimized for delivering very high specific capacity values (near theoretical value of 170 mAh g^{-1}) at low C-rates, but having low rate capability at high C-rate due to lack of good diffusion characteristics.

Differently from the $LiFePO_4$hydrothermally synthesized with the use of the organic surfactant, the addition of graphene oxide did not produce the expected effect over the commercial $LiFePO_4$. The reason probably resides in the fact that graphene oxide does not feature the striking conductivity of pure graphene in its reduced state, resulting to be not enough conductive to improve an already optimized material. Following this hypothesis, a chemical process to get rid of the oxygen impurities has been performed in order to obtain a phase pure reduced graphene having suffiently enhanced conductivity to improve the performance of the $LiFePO_4$.

3.5.1 Reduction of graphene oxide

Chemists have found different method to obtain graphene: chemical vapour deposition, micro-chemical exfoliation, epitaxial growth, cut of carbon nanotubes, sonication and chemical reduction [91]. Chemical reduction of graphene oxide (GO) is the most attractive

among the various method to produce reduced graphene oxide (rGO) because of its adaptability to large scale production at relatively low cost [92]. Hydrazine is the most effective reducing agent reported in literature, nevertheless its toxicity is an important drawback for the possible future increasing demand of graphene [93]. Therefore, greener reductants are highly appreciated in order to develop new environmentally friendly synthesis routes. To this purpose, Vitamin C (L-ascorbic acid, L-AA) is generally considered the best substitute for hydrazine [69], [73]. Fernández-Merino [94] carried out an exhaustive comparison of the performance of several reducing agents with different concentrations and definitively showed that L-AA equals hydrazine in the reducing efficiency. In literature, several reducing strategies involving L-AA are reported. The reduction reaction occurs in a neutral, basic or acid environment [95]. As far as concern the basic environment, either ammonia or sodium hydroxide can be used [96]. The slightly alkaline environment has been found to be more favourable over neutral conditions. In fact, it is believed to promote the colloidal stability of graphene oxide sheets through electrostatic repulsion, thereby preventing the agglomeration of the reduced graphene oxide (rGO) layers during the reduction reaction [93], [97]. In this work, the chemical reduction of graphene oxide has been performed using L-AA in a basic environment according to the procedure detailed in the followings.

First, 0.1 mg ml^{-1} of GO is added to a 1 mM solution of L-AA in doubly distilled water (Milli-Q) [94]. Then, the pH of the solution is increased to 9-10 by the addition of 28% ammonia solution (*Aldrich)*. The solution is rapidly poured in a sealed Teflon bottle and left 30 minutes in an oven at 95 °C. At the end of the heat treatment, the newly formed rGO colloidal suspension has to deposit, to allow the proper removal of the remaining traces of unreacted L-AA and any other compounds that might have formed during the reaction. However, the deposition of the rGO layers is hindered by the alkaline environment. Therefore, the suspension is poured in a dialysis tubing cellulose membrane (*Sigma-Aldrich*) in order to restore a neutral pH through ionic exchange and concurrently allowing the deposition of the suspended material. As shown in **Figure 3.19**, the cellulose membrane is placed in a beaker filled with double distilled water. Due to the concentration gradient, ammonium ions (NH_4^+) diffuse through the semi-permeable membrane until a concentration equilibrium is reached between the water contained in the beaker and the solution inside the tube. In the meanwhile, the rGO layers deposit at the bottom of the tube. After approximately 5-6 hours, the value pH is evaluated. If the solution is still slightly basic, the liquid is drained and both the membrane and the beaker are re-filled with fresh doubly distilled water. This iterative procedure stops when the liquid contained both in the tube and in the beaker shows pH =

7. Eventually, the solid deposition is transferred in a plastic falcon, centrifuged three times at 10000 r min^{-1} for 15 minutes in order to remove all the residuals of the reduction reaction and dried under dynamic vacuum in a B$\ddot{u}$chi chamber for two hours at 50 °C.

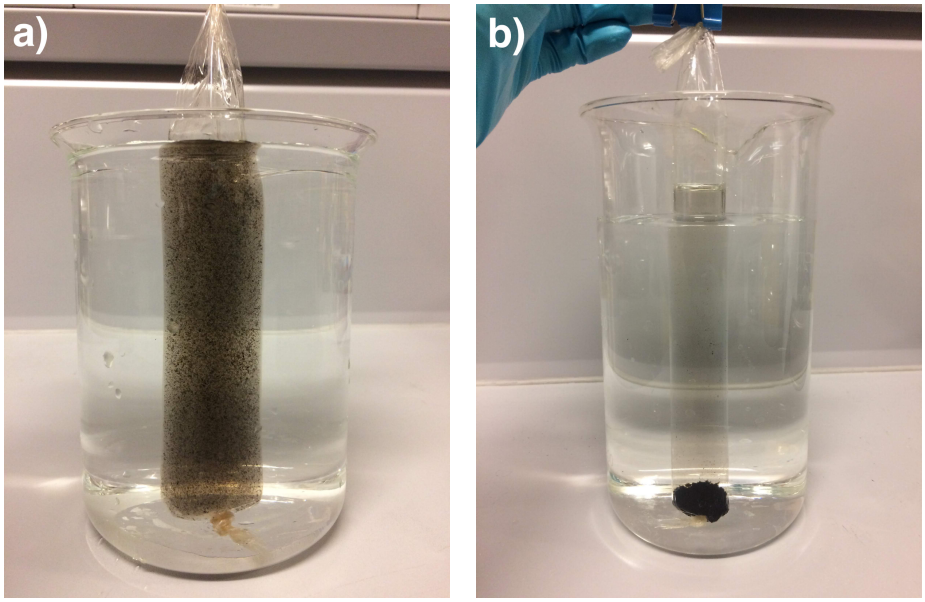

Figure 3.19 Reduction of graphene oxide in a dialysis tubing cellulose membrane, (a) immediately after being poured, (b) at the end of the iterative re-filling process corresponding to a pH=7 of the solution and deposition of rGO layers.

3.5.2 Structural characterization of reduced graphene oxide by X-ray powder diffraction

X-ray powder diffraction (XRPD) patterns were measured by an X'Pert MPD DY 1165 diffractometer equipped with Cu Kα radiation with diffraction data collected in the 2θ range of 10-35° with intermittent step of 0.02°. **Figure 3.20** reports the XRD pattern of the reduced graphene oxide. As it can be clearly seen, rGO shows an amorphous character. The absence of the characteristic diffraction peaks reported in literature for graphite at 2θ = 26.5° is indeed the expected result. The reason can be explained by considering the definition of Bragg's law (see **Appendix I.I**) itself according to which a diffraction peak is recorded when a constructive interference occurs between the crystalline planes and the incident X-ray. Being graphite composed of several 2D layers, namely graphene, constructive interactions between the layers and the X-ray give rise to the diffraction peaks, whereas if a single layer (or anyway a very few layers) of graphite are exfoliated, it is not possible to record any peak.

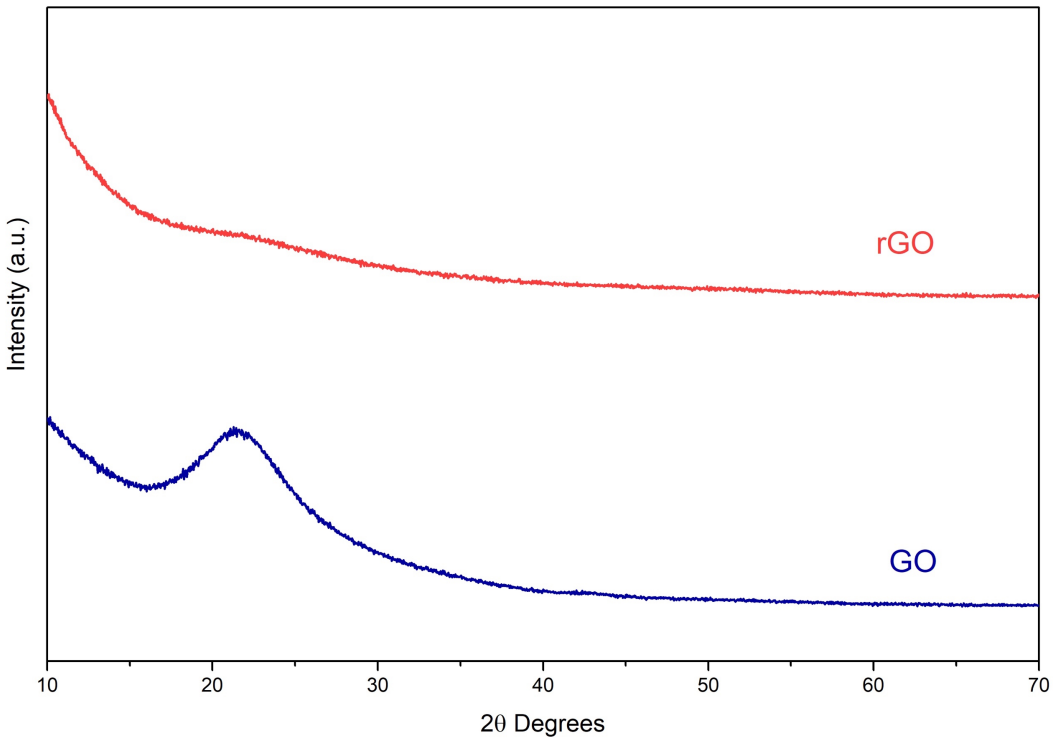

Figure 3.20 XRPD diffraction pattern of reduced graphene oxide (rGO) and graphene oxide (GO).

3.5.3 Electrochemical comparison of samples LFP-COM and LFP-COM-rGO. The influence of reduced graphene oxide at high current regimes

In order to evaluate the effect of the addition of rGO on the electrochemical behaviour of LFP, two test electrodes (LFP-COM and LFP-COM-rGO) are prepared according to the methodology detailed in **paragraph 3.1.2** and assembled in a three electrode T-type cell using lithium metal as counter electrode and 1 M of $LiPF_6$ in 1:1 EC:DEC solution as electrolyte (in the case of cyclic voltammetry, Li-metal is used also as the reference electrode). LFP-COM contains $LiFePO_4$ with carbon black as conductivity enhancer and PvDF as binder, according to the standard composition already used for LFP-STD, while rGO is added to the second slurry (LFP-COM-rGO) in the same amount (4%) as GO was introduced in the sample LFP-STD-GO. **Table 3.3** reports the weight percentages of the components of the two electrode slurries.

Weight %	LFP-COM	LFP-COM-rGO
Active material	70	70
Carbon Black	20	16
rGO	-	4
PvDF	10	10

Table 3.3 Weight percentage of the components of the slurry for the electrode preparation of the two samples LFP-COM, LFP-COM-rGO.

Cyclic voltammetry

Figure 3.21 compares the 10th voltammetric cycles of the two electrodes performed at ambient laboratory temperature between the voltage range 2.8-4 V vs Li^+/Li and a scan rate of 0.1 mV s^{-1}.

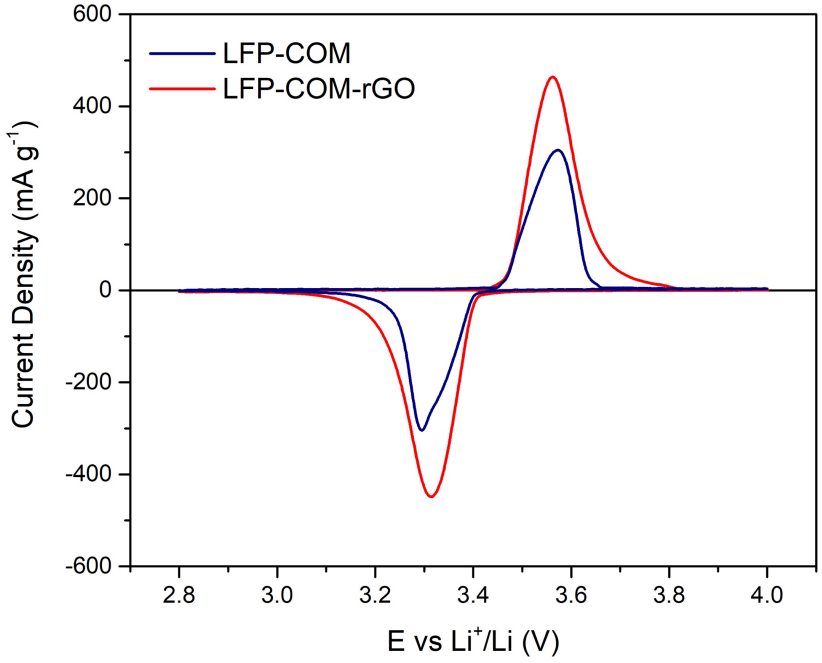

Figure 3.21 Comparison between the 10th voltammetry cycles of the samples LFP-COM and LFP-COM-rGO at ambient laboratory temperature. Scan rate 0.1 mV s. Voltage range 2.8-4 V vs. Li+/Li.

The addition of rGO leads to the formation of more intense and sharper current peaks, respectively ascribed to an increased current density and an improved kinetics of Li^+ extraction and insertion process. In addition, the anodic and cathodic peaks of LFP-COM-

rGO are closer to each other with a mid-point potential of 3.43 V vs. Li^+/Li accounting for an enhanced reversibility of the electrochemical process in the material.

Galvanostatic cycling at high C-rates

As already anticipated, LFP-COM is already optimized for delivering high capacities at low C-rates, but showing poor performances under high current regimes. Therefore, it is interesting to evaluate if the addition of the reduced graphene oxide improves the Li^+ ion diffusion through the active particles at high C-rates. **Figure 3.22** shows the comparison of the galvanostatic cycling of standard LFP-COM and the sample with rGO as co-conductivity enhancer (LFP-COM-rGO).

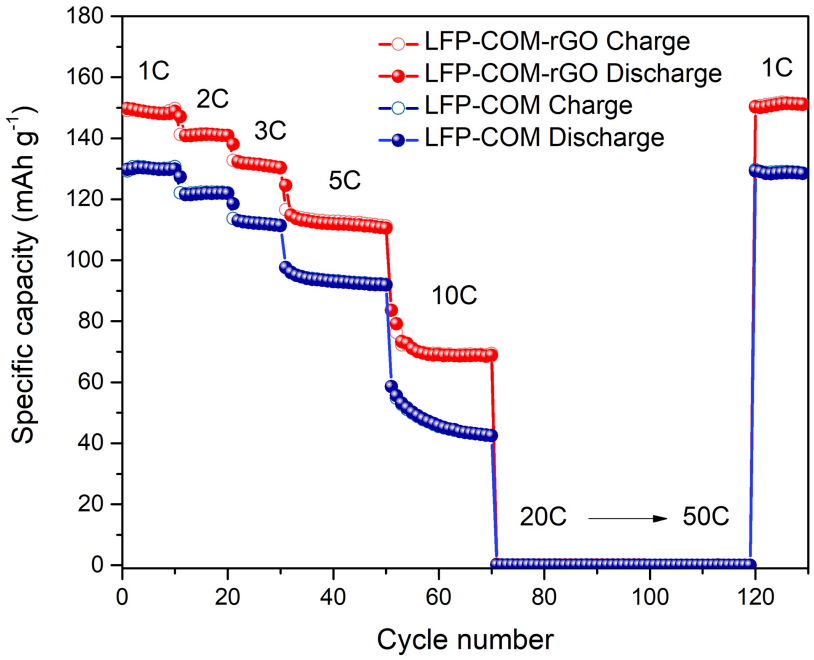

Figure 3.22 Comparison of the cycling performance at high C-rates of the samples LFP-COM and LFP-COM-rGO, cycled from 1C to 50C at ambient laboratory temperature.

Remarkably, sample LFP-COM-rGO shows a capacity in discharge of 147 mAh g^{-1} (148 mAh g^{-1} in charge) at the 10th cycle at 1C rate against the 130 mAh g^{-1} (132 mAh g^{-1} in charge) of the standard LFP-COM sample. This increase in specific capacity is even more evident at higher 10C rate, with LFP-COM-rGO providing 58 mAh g^{-1} in discharge after the 70th overall cycle (over the 43 mAh g^{-1} of LFP-COM) and better cycling stability. Nevertheless, the addition of rGO provides enhanced performance only at lower C-rate; indeed, for both the materials the capacity drops to zero at C-rates higher than 20C. The reason might reside in

the different synthesis process of the $LiFePO_4$, which is not suitable for operating under highly severe current conditions. Therefore, Li^+ ions diffusion is likely limited by the different structural morphology of the material and cannot allow proper operation under ultrafast current rates, regardless of the enhancement in the conductivity provided by the addition of the reduced graphene oxide. The following figures show the voltage vs specific capacity profiles of the two samples at different C-rates.

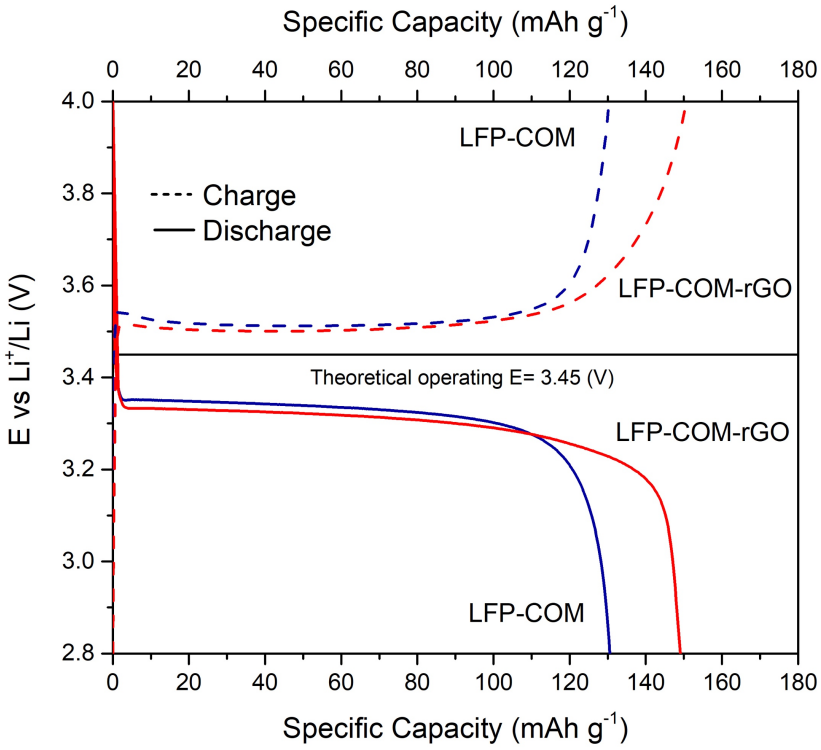

Figure 3.23 Comparison of the charge/discharge profiles of the samples LFP-COM and LFP-COM-rGO at 1C rate. Cycles extracted from cycling tests carried out at increasing C-rates at ambient laboratory temperature.

The profiles at 1C rate (**Figure 3.23**) appear very similar (LFP-COM shows a working potential of 3.36 V and LFP-COM-rGO of 3.35 V), showing the characteristic flat plateau given by the two-phase Li^+ insertion process. All the figures show the enhanced performance of the material upon addition of rGO (namely, increased specific capacity and more flat and extended voltage plateau). Well evident is the difference in the overpotential at 5C (**Figure 3.24**) and 10C (**Figure 3.25**) rate. In particular, at 10C rate LFP-COM-rGO shows an almost flat plateau during charge, which is ascribed to an improved extraction kinetics of Li^+.

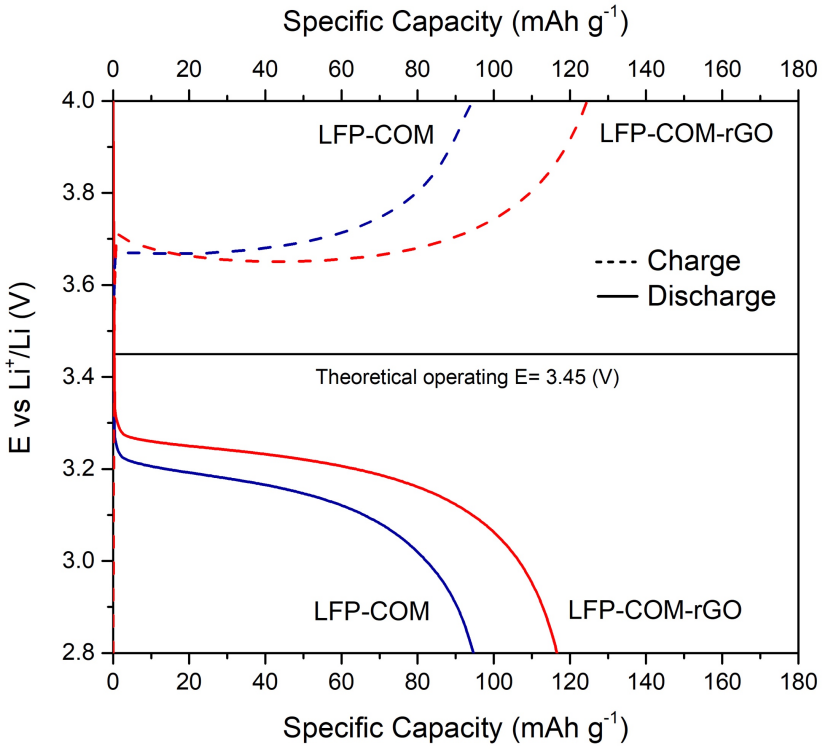

Figure 3.24 Comparison of the charge/discharge profiles of the samples LFP-COM and LFP-COM-rGO at 5C rate. Cycles extracted from cycling tests carried out at increasing C-rates at ambient laboratory temperature.

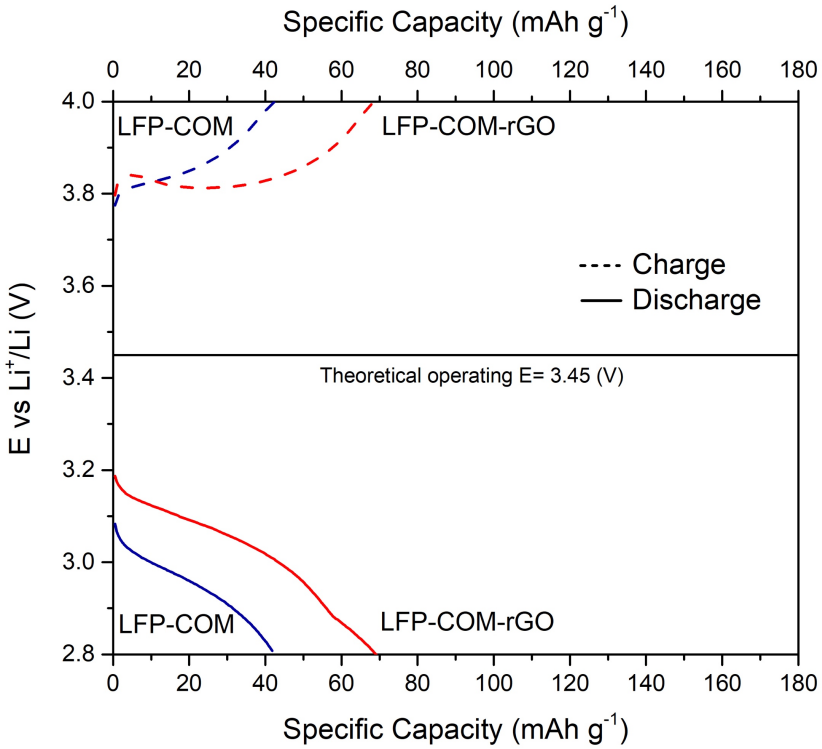

Figure 3.25 Comparison of the charge/discharge profiles of the samples LFP-COM and LFP-COM-rGO at 10C rate. Cycles extracted from cycling tests carried out at increasing C-rates at ambient laboratory temperature.

4. $LiFePO_4$ as pristine material for the development of sodium intercalated $NaFePO_4$: moving from lithium-ion to sodium-ion batteries

This chapter describes the research activity carried out during an internship stage at the *Collège de France*, Paris, under the guidance of Professor Jean-Marie Tarascon and his research group in the *Solid State Chemistry and Energy Lab*.

Li-ion batteries play a central role among the electrochemical storage systems, leading the market share of small-scale consumer electronics and power tools, as well as for the newly born electric automotive sector. However, the foreseen explosion of electric and plug-in hybrid electric vehicles production will drive the depletion of lithium resources, with the unavoidable increase of its price. In addition, the major transformation of the power grid towards smarter systems, which allow the connection of the increasing fluctuant renewable energy mix, will require even larger storage capacities and Li-based batteries are already not competitive in terms of cost for the grid-connected use. The diversification of the electrochemical storage systems is therefore essential and sodium-ion technology may greatly contribute to guarantee a highly efficient and low-cost alternative, in particular for the large-scale production of power supply systems for/from renewables. In fact, despite the higher reduction potential compared to lithium, sodium has several advantages in terms of low environmental impact, abundance and widespread of resources. Nevertheless, this is not considered a serious setback for use in power supply systems, which do not need very high energy and power densities.

The aim of this research activity is to illustrate the possibility of using the optimised $LiFePO_4$ as pristine material for the formation of its chemical equivalent sodium-based polyphosphate ($NaFePO_4$), maintaining the olivine-type structure of $LiFePO_4$ characterized by functional cationic channels for an ease and fast Na^+ extraction and insertion. Furthermore, $NaFePO_4$ is implemented as cathode material with commercial hard carbon as anode in full-cells configuration; a proper parametric setting is carried out in terms of mass balance and operating voltage window for exploiting at maximum the electrochemical performances of this sodium-based compound. As already reported in literature following the pioneering work of P. Moreau [81], the olivine structured $NaFePO_4$ can be prepared via chemical or electrochemical redox reactions from the pristine $LiFePO_4$. The electrochemical

process deals with the use of the galvanostatic cycling technique to extract Li^+ and insert Na^+ ions into the $FePO_4$ de-lithiated structure, whereas the chemical way exploits the oxidizing and reducing ability of co-reagent compounds (NO_2BF_4 and NaI) to chemically prepare the sodium intercalated $NaFePO_4$.

4.1 Materials and methods

4.1.1 Methodology for the electrochemical de-lithiation of $LiFePO_4$ and sub-sequent Na ion intercalation

The electrochemical de-lithiation of $LiFePO_4$ is performed in a two-electrode stainless-steel Swagelok®-type test cell properly sized to host a large amount of electrode material (**Figure 4.1**). For the electrochemical measurements, the working positive electrode is prepared by ball-milling (15 min) of the dry $LiFePO_4$ powder (80 wt%) with Carbon SP (20 wt%) as conductivity enhancer. No binders are used and no homogeneous slurries are prepared.
The Swagelok® cell is assembled in an Argon-filled Dry Glove Box (*MBraun 2000B,* H_2O and $O_2 < 0.1$ ppm). First, a Mylar® insulating membrane is placed around the internal walls of the main cell body to avoid internal short-circuits and an aluminium foil is contacted at the bottom acting as cathode current collector. The ball-milled powder is placed onto the Al foil and covered with three circular glass microfiber separators (*Whatman*), these latter are then wet with 1 M of $LiPF_6$ dissolved in a 1:1 EC:DMC solution acting as electrolyte. A high purity lithium foil *(Aldrich)*, used as negative electrode, is contacted on a stainless-steel circular current collector disk and pressed on the separators by three springs and a stainless-steel cylinder, which is eventually tightened to the rest of the cell with a plastic O-ring and a screw nut. The structure of this cell has inherent limitations in avoiding air infiltration and providing a proper electrical contact between the positive and negative poles. Therefore, the electrochemical tests are performed with the cell left inside the Argon-filled Glove Box and only the firsts few charge/discharge cycles provide reliable results before showing problems related to an improper contact between the electrodes. The electrochemical de-lithiation consists in a single complete galvanostatic charge cycle in which the Li^+ ions are extracted from the orthorhombic $LiFePO_4$.
After the charge process, the de-lithiated $FePO_4$ is washed several times with DMC (*Sigma-Aldrich)* and used as cathode in a Swagelok® cell having electrode diameter of 1 cm for the electrochemical sodiation (namely, the insertion of Na^+ ions). The smaller Swagelok® cell

(**Figure 4.2**) feature a better insulation and electrical contact, enabling to perform galvanostatic tests for several cycles.

Figure 4.1 A two electrode swagelok-type test cell sized to host great bunches of electrode material.

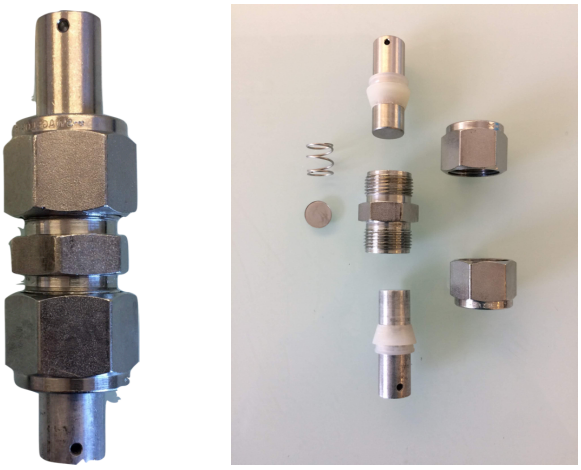

Figure 4.2 Swagelok-type test cell for electrochemical insertion of Na+ ions.

In the assembly procedure, a Mylar® membrane is placed at the interior walls of the central body to avoid internal short-circuit. An aluminium cylinder of 8 mm of diameter is inserted in the inferior hole of the stainless-steel central body and tighten with a plastic O-ring and a screw nut. The de-lithiated olivine $FePO_4$ is laid down at the centre of the aluminium cylinder inside the main body, and then three -glass fibre separators are placed on the top of the powder and wet with few droplets of 1 M of $NaPF_6$ in polycarbonate (PC) solution acting as electrolyte. High purity sodium metal is spread on a stainless-steel current collector disk and

pressed on the separators with a spring and a stainless-steel cylinder; tightened to the central body with a second O-ring and a bolt. The electrochemical sodiation consists in a single complete discharge cycle in which Na^+, provided by the sodium metal anode, inserts in the de-lithiated $FePO_4$ olivine structure.

Eventually, the sodium intercalated $NaFePO_4$ is washed with DMC and electrochemically characterized within coin-type cells (R-2032) in full cell configuration, namely with commercial hard carbon used as anode material.

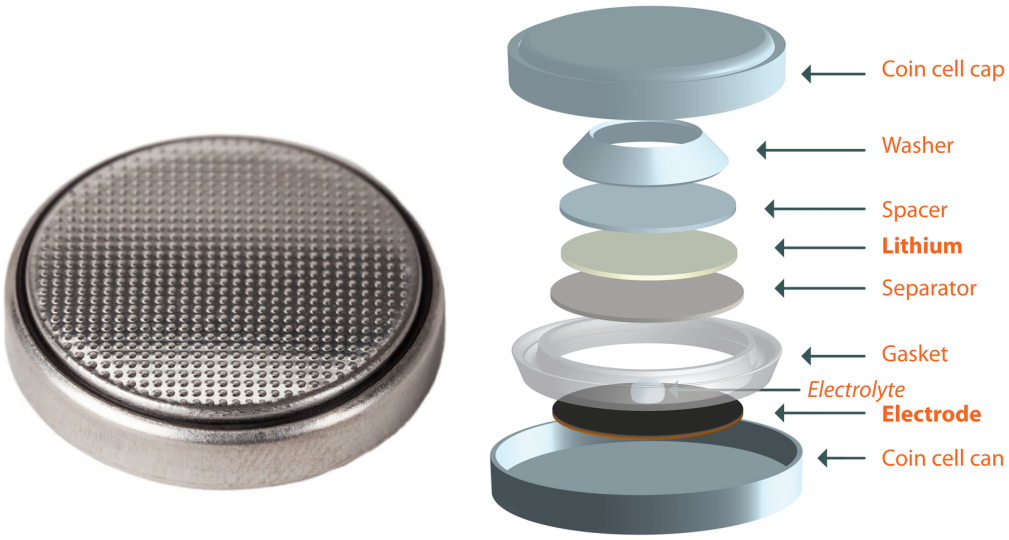

Figure 4.3 Coin-type R-2032 test cell for the electrochemical characterization of sodium intercalated $NaFePO_4$ for application in Na-ion batteries.

The coin-type (**Figure 4.3**) is a two-electrode test cell in which an anodic circular current collector is sealed with a cathodic current collector, providing excellent insulation and electrical contact. It is assembled in the Argon-filled Glove Box according to the same procedure as for the Swagelok® cell. The cathodic current collector hosts an aluminium foil over which the sodiated $NaFePO_4$ is placed, covered with two glass microfiber separators and wet with few droplets of 1 M $NaPF_6$ in PC solution as electrolyte. Eventually, a hard carbon and a stainless-steel current collector disks are put on top of the separators, acting as negative (counter) electrode, while a circular spring complete the assembly procedure before that a crimping machine seals the anodic current collector to the rest of the cell. The cell is now transferred outside the Argon-filled glove box to undergo the electrochemical testing.

4.1.2 Methodology for the chemical de-lithiation of LiFePO4 and sub-sequent Na ion intercalation

The olivine structured $NaFePO_4$ can also be obtained via chemical oxidation of the pristine $LiFePO_4$ and sub-sequent reduction of the de-lithiated $FePO_4$ in the Argon-filled dry glove box environment. The pristine $LiFePO_4$ is added to a 0.5 M nitronium tetrafluoroborate solution (NO_2BF_4, *Alfa Aesar*, *99+%*) in acetonitrile (*Sigma-Aldrich*) with low excess of NO_2BF_4 (molar ratio $\frac{mol_{NO2BF4}}{mol_{LiFePO4}} = 1.2$) and left under an Argon environment for 24 h at ambient laboratory temperature to obtain the heterosite $FePO_4$. The oxidation of Fe^2 to Fe^3 and the Li^+ extraction likely occurs according to the following reaction:

$$LiFePO_4 + NO_2BF_4 \rightarrow FePO_4 + NO_2 + LiBF_4 \quad (4.1)$$

The heterosite $FePO_4$ is then reduced with excess of sodium iodide (molar ratio $\frac{mol_{NaI}}{mol_{LiFePO4}} = 2$) in 0.5 M NaI (*Alfa Aesar, 99.5+%*) solution in acetonitrile for 40 h at 60 °C according to the following reaction:

$$2FePO_4 + 2NaI \rightarrow 2NaFePO_4 + I_2 \quad (4.2)$$

Eventually, the sodium intercalated olivine structured $NaFePO_4$ is deeply washed with acetonitrile and vacuum dried overnight in a Büchi chamber (*Model B-585*). **Figure 4.4** shows the final centrifugation cleaning procedure of the deposited $NaFePO_4$ with the removal of the newly formed, yellowish iodine.

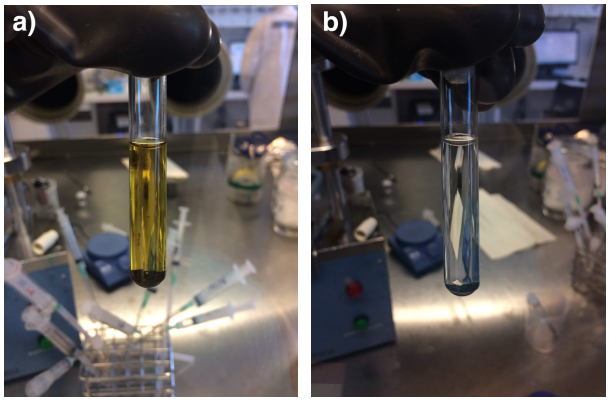

Figure 4.4 Before (a) and after (b) the cleaning procedure of the chemically reduced $NaFePO_4$ with NaI. The yellowish iodine must be completely removed or it might affects the electrochemical performances.

4.2 Electrochemical de-lithiation of the pristine $LiFePO_4$

$LiFePO_4$ is de-lithiated through a galvanostatic charge cycle over Li metal at C/20 up to the cut-off voltage of 4 V vs. Li^+/Li and, then, held at that voltage value until the current freely decreases to a limit corresponding to a C/200 rate, which accounts for the complete removal of Li^+ ions.

Figure 4.5 shows the characteristic flat voltage plateau upon galvanostatic charge, evolving at 3.5 V vs. Li^+/Li and reaching a maximum specific capacity of 165 mAh g^{-1} out of the theoretical 170 mAh g^{-1}. The graph clearly demonstrates that 0.92 Li^+ per formula unit have been successfully extracted from the olivine $LiFePO_4$, obtaining an almost completely de-lithiated $FePO_4$.

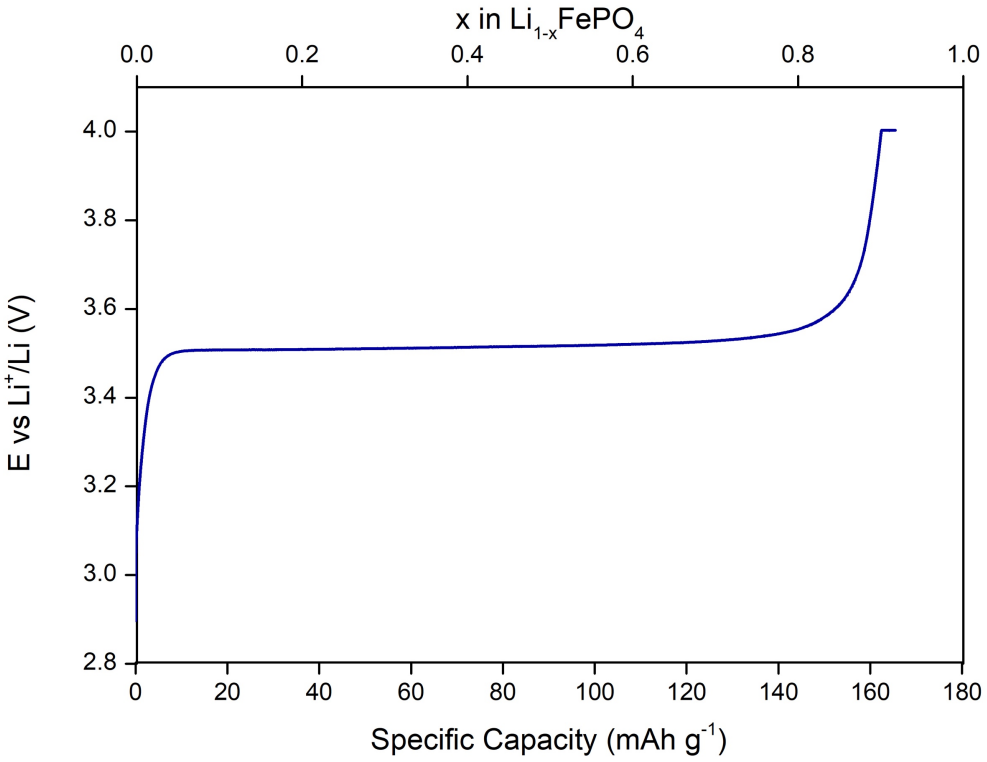

Figure 4.5 Voltage vs ratio of Li^+ (top x axis) and specific capacity (bottom x axis) profiles of the electrochemical galvanostatic de-lithiation process at C/20 of the pristine $LiFePO_4$.

4.3 Electrochemical Na^+ ions insertion into the olivine phase $FePO_4$

The electrochemical insertion of Na^+ ions into the de-lithiated $FePO_4$ occurs through a galvanostatic discharge cycle in a two-electrode Swagelok®-type cell against Na metal at a

current rate of C/20, starting from the open circuit voltage up to a lower cut-off limit of 2.2 V. A following charge cycle is performed up to the upper cut-off voltage of 4 V in order to study the reversibility of the process. The results are shown in **Figure 4.6**.

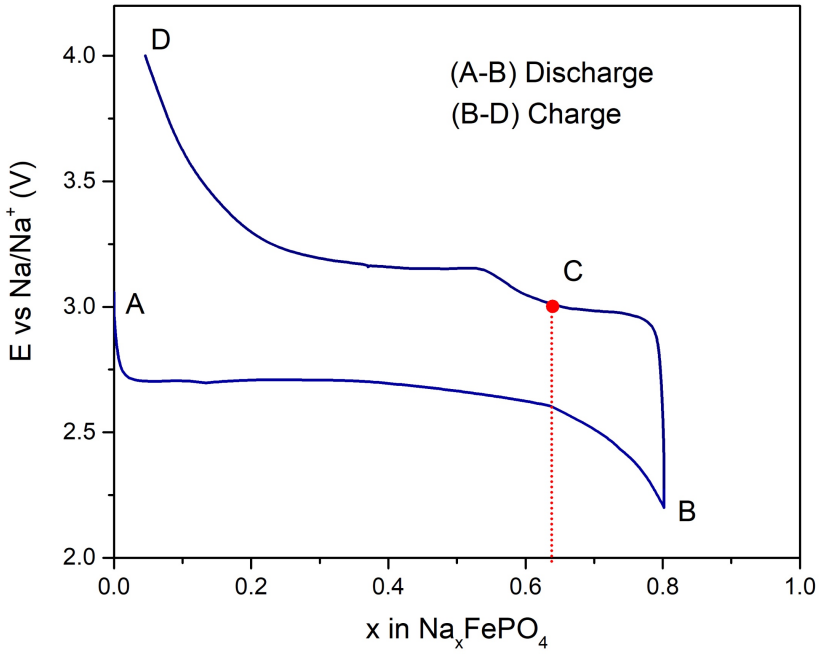

Figure 4.6 Insertion of Na^+ (discharge, A-B) into the de-lithiated $FePO_4$ and following first charge cycle (B-D). Cycled at C/20 at ambient laboratory temperature in a Swagelok® cell against Na metal counter electrode and 1 M $NaPF_6$ in PC as electrolyte.

Figure 4.6 shows that 0.8 Na^+ per formula unit can be reversibly intercalated in the $FePO_4$ structure. Likewise the electrochemical redox reaction already seen for $LiFePO_4$ versus lithium metal, during discharge Na^+ inserts in the host structure with the corresponding reduction of Fe^{3+} to Fe^{2+}, while the extraction of Na^+ takes place with the concurrent oxidation of Fe^{3+} to Fe^{2+} during charge, according to the following reaction:

$$NaFePO_4 \leftrightarrow Na_{1-x}FePO_4 + xFePO_4 + xNa^+ + xe^- \quad (5.3)$$

Nevertheless, $NaFePO_4$ shows a noticeable difference in the voltage profiles during charge and discharge. The discharge profile exhibits an almost flat plateau starting at 2.72 V vs Na^+/Na and a sloping decay at its end, whereas two plateaus (at 3.05 V and, then, at 3.46 V vs Na^+/Na) are observable in charge as a consequence of a voltage discontinuity at the corresponding Na^+ ratio of about x = 0.65 (point C). The peculiar difference in the charge

and discharge behaviour is consistent with the results reported in literature and is likely due to an asymmetric kinetics of the two processes [78]. The voltage discontinuity indicates that the charge reaction undergoes two activation energy levels; in the range $0.65 < x < 0.8$ the activation energy is lower than in the range $0 < x < 0.65$, therefore while moving from $x = 1$ to $x = 0$ (charge) the system has to overcome a second, higher, kinetic barrier. The single plateau upon discharge is correspondingly explained by the fact that, while moving from $x = 0$ to $x = 1$, the reaction firstly encounters the higher activation barrier and the required electrical overpotential is already enough to overcome the second (lower) energy barrier [98]. The discontinuity in the charge voltage profile was firstly explained by Moreau at al [81] as corresponding to the formation of an intermediate phase at $x = 0.7$ ($Na_{0.7}FePO_4$) and further investigations over the phase diagram of the olivine $NaFePO_4$ revealed that the first voltage plateau at 3.05 V vs Na^+/Na corresponds to a single phase solid-solution region, while the second plateau at 3.46 V vs Na^+/Na arises from a biphasic reaction involving the intermediate $Na_{0.7}FePO_4$ and $FePO_4$ phases. Due to the presence of different interfaces, the two-phase region requires a higher activation energy to overcome the related kinetic barrier. However, despite the single plateau, the discharge process provides information on the intermediate phase formation. Indeed, the final sloping decay occurs concurrently to the voltage discontinuity of the charge profile. The reason might reside in the great stability of the intermediate phase $Na_{0.7}FePO_4$ [98]; as a result, once it is formed, a further intercalation of Na^+ might result very difficult. In conclusion, the formation of an intermediate phase while cycling $NaFePO_4$ is the sign of an increased interaction of sodium ions with the host structure in comparison to the pristine $LiFePO_4$ where no intermediate compositions are reported under standard operating conditions [99].

4.4 Electrochemical characterization in half cells of the sodium intercalated $NaFePO_4$

The galvanostatic characterisation of the olivine $NaFePO_4$ is performed to assess the cycling behaviour of the sodium-intercalated sample at different C-rates at ambient laboratory temperature versus sodium metal and with 1 M of $NaPF_6$ in PC solution as electrolyte. Both **Figure 4.7** and **Figure 4.8** illustrate the voltage versus specific capacity profiles of $NaFePO_4$, in particular the former shows the capacity loss at progressively increasing C-rates, while the latter the cycling stability at a fixed C-rate.

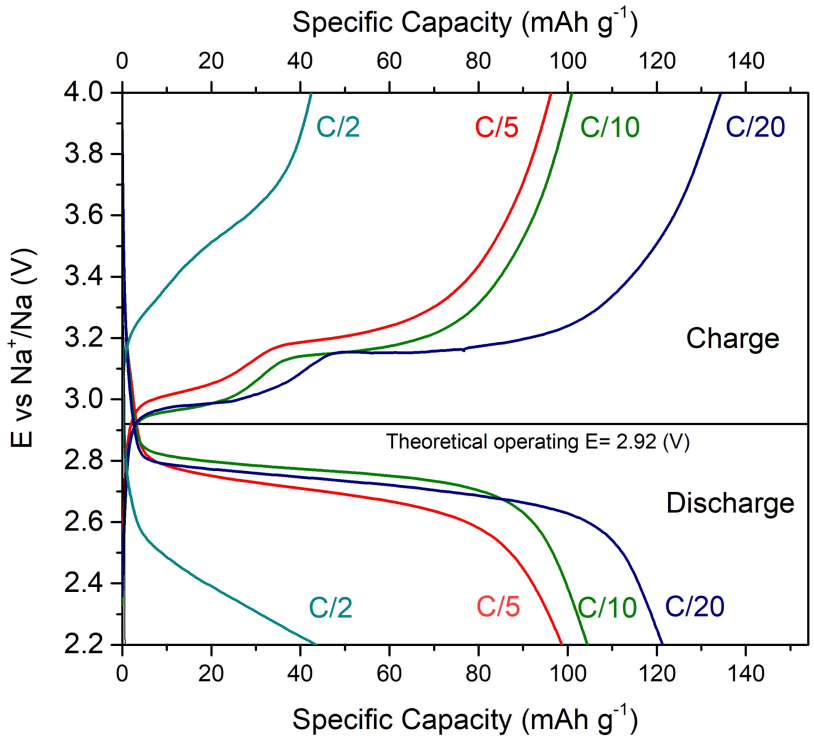

Figure 4.7 Charge/discharge potential vs. specific capacity of the sodium intercalated $NaFePO_4$. Cycles extracted from cycling tests carried out at increasing C-rates at ambient laboratory temperature.

The sodium intercalated $NaFePO_4$ exhibits remarkable specific discharge capacities of 121 mAh g^{-1} at C/20 (134 mAh g^{-1} in charge) and 105 mAh g^{-1} at C/10 (103 mAh g^{-1} in charge) out of the theoretical 154 mAh g^{-1}, in accordance with the values already reported in the literature [82], [98], [100]. By increasing the C-rate from C/20 to C/5, the overpotential increases slightly, while at reasonably high C/2 rate, the voltage plateaus are hardly distinguished and the overpotential is large, which is ascribed to the limited ionic and electronic conductivity of $NaFePO_4$. Despite the rather low coulombic efficiency varying from 93 % to 96 %, the sodium insertion and extraction processes are highly reversible, as confirmed by the retention of the double plateau upon cycling. Starting with an average value of overpotential of 2.79 V vs Na^+/Na out of the theoretical operating voltage[9] of 2.92 V at the first discharge cycle, the polarization increases after the 10th cycle, following the constant decrease of the specific capacity up to the 20th cycle.

[9] The theoretical operating voltage of the electrochemical Na^+ de/intercalation reaction is reported by Moreau et al [81] and determined by considering a hypothetical single plateau between $FePO_4$ and $NaFePO_4$.

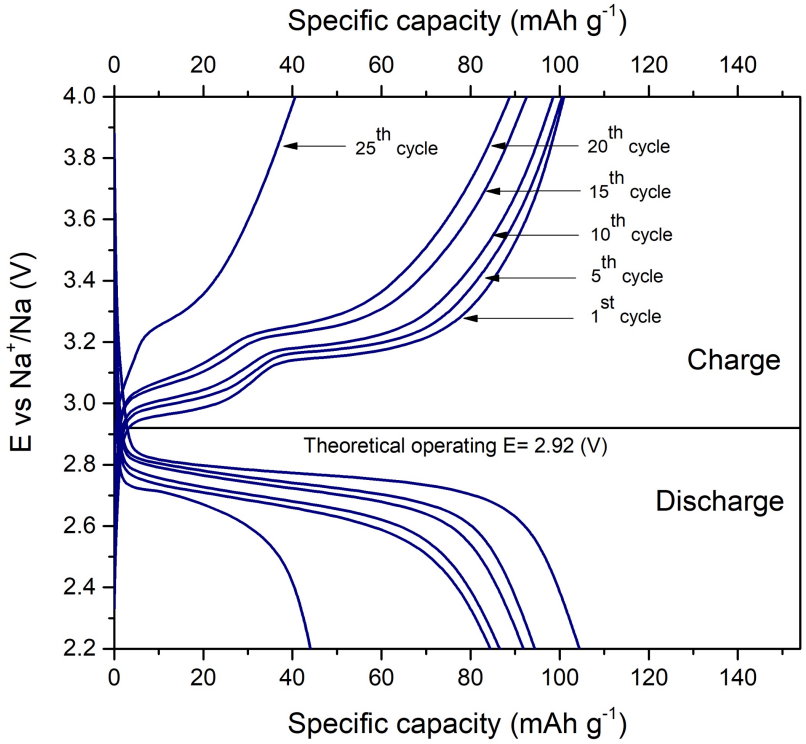

Figure 4.8 Charge/discharge potential vs. specific capacity of the sodium intercalated $NaFePO_4$. Cycled at constant C/10 rate at ambient laboratory temperature.

The peculiar reaction mechanism involving an intermediate phase formation and the large volume contraction and expansion (about 17 %) of the $FePO_4$ structure upon cycling, due to the larger ionic ratio of sodium ion (102 pm for Na^+ and 76 pm for Li^+) [98], likely leads to a more pronounced loss of performance and to the charge/discharge polarization. Moreover, the imperfect mechanical integrity and sealing from atmospheric moisture of the Swagelok®-type test cells might be a reason for the fast decay in the electrochemical performances of the material. Clearly, optimisation is needed mainly in the preparation process, but the successful sodiation and following reversible operation of the obtained $NaFePO_4$ cathode material is well demonstrated.

4.5 Electrochemical characterization in full cells of the electrochemically sodium intercalated NaFePO4

The sodium intercalated $NaFePO_4$ (NFP) is an appealing cathode material for large-scale battery production because of its environmentally friendly and abundant constituting elements in addition to the acceptable values of energy and power density. The study carried out so far in Swagelok®-type cells was focused on demonstrating the feasibility of simple cation exchange from a pristine $LiFePO_4$ and the reversibility of the Na^+ intercalation

process into the olivine $FePO_4$ in electrochemical cells versus sodium metal anode. However, in order to assess the practical application of the developed $NaFePO_4$ cathode material, its storage behaviour is hereafter evaluated in terms of cell balance and working voltage window in a full cell configuration versus a commercial hard carbon (HC) anode. To the best of my knowledge, the following is the first study of this kind to be performed for the sodium intercalated $NaFePO_4$. The electrochemical performance of the NFP/HC full cell is evaluated in R-2032 coin-type cells assembled as described in **paragraph 4.1.1**. HC anodes are among the best performing negative electrode materials on the market, providing a specific capacity of about 300 mAh g^{-1} at full DoD[10] up to approximately 0 V vs Na^+/Na [101]. When assembling a full cell, which normally encompasses two active materials having different specific capacity at the two electrodes, balancing in terms of overall capacity (Ah) delivered by the two electrodes must be accurately obtained in order to get proper cell operation; cell balancing has been obtained according to the following equation:

$$C_+ = C_- \cdot (1 + n) \tag{4.4}$$

Being:

$$C_+ = m_{cathode} \cdot c_{cathode} \ [Ah] \tag{4.5}$$

$$C_- = m_{anode} \cdot c_{anode} \ [Ah] \tag{4.6}$$

where $m_{cathode}$ and m_{anode} are the grams of the active material at the cathode and anode sides, respectively, while $c_{cathode}$ and c_{anode} are the corresponding specific capacities in Ah g^{-1}. An empirical coefficient $n \neq 0$ is generally considered to avoid the following two undesired shortcomings:

- plating of Na^+ ions over the anode surface with Na metal dendritic growth;
- excess solid electrolyte interphase (SEI)[11] formation on the anode surface with important loss of active ions.

[10] A battery's depth of discharge (DoD) indicates the percentage of the battery that has been discharged relative to the overall capacity of the battery.

[11] The Solid Electrolyte Interphase (SEI) is a solid layer formed at the anode surface due to the decomposition of some of the electrolyte components. See **paragraph 2.3.4** for a more comprehensive explanation.

To avoid the first drawback, a value of $n < 0$ is applied and the cell configuration is therefore "cathode-limited", namely a lower amount of active material is used at the cathode side with respect to the corresponding amount if n was equal to 1. On the contrary, to avoid an excess of SEI formation a value of $n > 0$ is considered and the configuration is therefore "anode-limited". The best value of n can only be found empirically and varies according to the system under study.

At first, assuming a possible plating of Na^+ onto the surface of the HC anode, the NFP/HC full cell is as assembled in a slightly cathode-limited configuration, with a 4 % of weight reduction of the active material at the anode ($n = -0.04$) and cycled at ambient laboratory temperature under the voltage ranges between 2 - 4 V vs Na^+/Na. **Figure 4.9** shows the galvanostatic charge/discharge voltage vs specific capacity profiles of the full cell at C/10 rate and by the analysis of the profiles shown in the graph, one can obtain several information on the system under study.

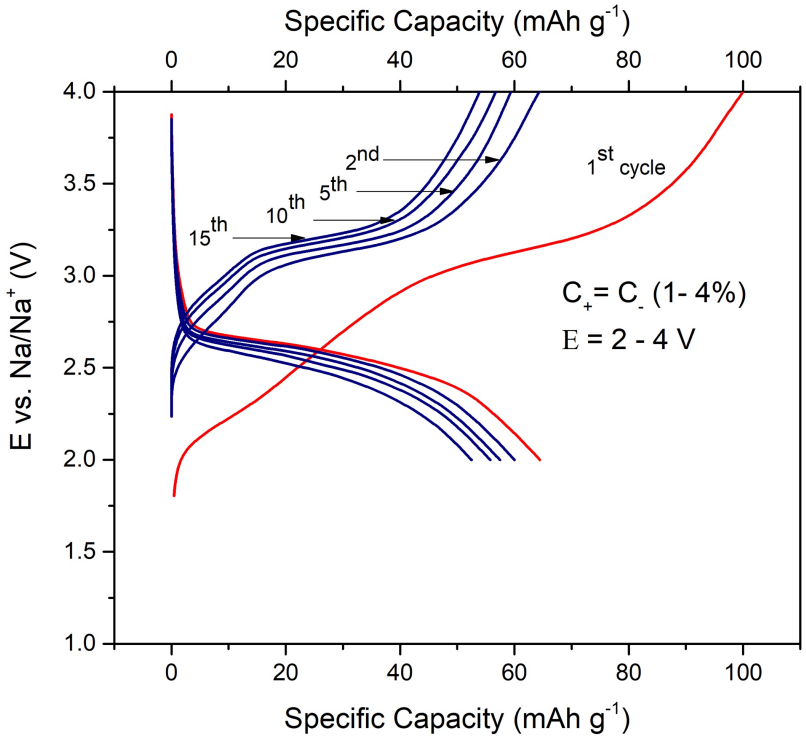

Figure 4.9 Charge/discharge voltage vs specific capacity profiles of the NFP/HC full cell assembled in a slightly cathode-limited configuration and galvanostatically cycled within the voltage window 2-4 V vs Na^+/Na at C/10 at ambient laboratory temperature.

First, the capacity fade of approximately 36 % with respect to the full charge capacity of 100 mAh g^{-1} between the first charge and discharge cycles (red lines on the graph) is clearly evident; it results in a limited 64 % coulombic efficiency upon initial cycling. Such a

remarkable capacity loss was indeed expected and can be ascribed to the SEI formation, namely some of the electrolyte components oxidise and irreversibly adsorb a considerable amount of Na^+ ions at the interface with the electrode material, resulting in the formation of a solid ion conducting layer, which, nonetheless, is fundamental for proper cell cycling as it avoid the further decomposition of the electrolyte. However, the Na^+ ions which have been adsorbed during SEI formation are inevitably lost and cannot be extracted during the followings discharge processes, which leads to the overall reduction of the specific capacity output.

The second recognisable information is the absence of the double plateau during charge, which is ascribed to the overlapping of the characteristic charge profile of NFP over sodium metal (**Figure 4.6**) and the single sloping plateau of HC that concurrently intercalates Na^+ as shown in **Figure 4.10**. Because of the overlapping of the profiles of the two active materials (NFP and HC), the NFP/HC full cell exhibits a first linear sloping profile upon charge, followed by an almost flat plateau corresponding to the second characteristics NFP/Na de-insertion process.

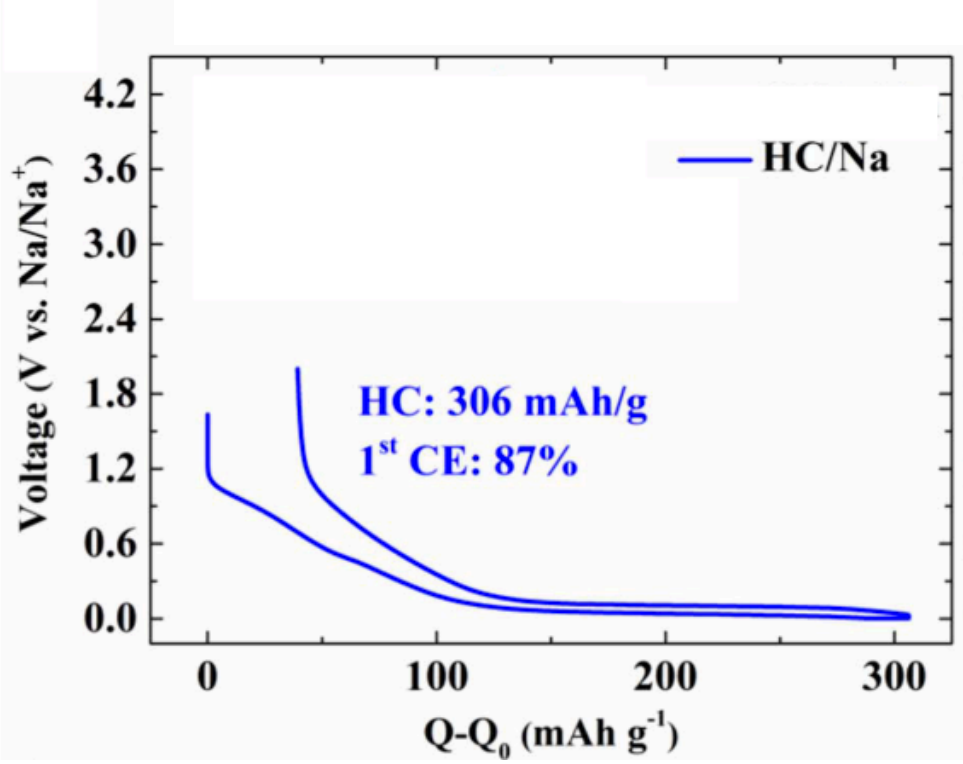

Figure 4.10 First charge/discharge cycle of HC vs Na metal cell, showing a coulombic efficiency of 87 %. Readapted from [101].

Eventually, the low value of coulombic efficiency shown in **Figure 4.10** also proves that the presence of HC in quality of active material at the anode side owns the responsibility of the SEI formation. In fact, no considerable capacity fade appears in the NFP/Na half-cell configuration as it is clearly visible in **Figure 4.8**. The following **Chapter 4.5.1** shows the effect of using a different n coefficient on the overall electrochemical performance of the NFP/HC system. In addition, it will be explored a second voltage scan range for the system in order to exploit the discharge electrochemical behaviour at lower potential values.

4.5.1 The effect of the voltage scan range and capacity balance on 1st cycle capacity fade

The slightly cathode-limited configuration led to a great loss of Na^+ ions after the first charge cycle; as a result, an anode-limited cell configuration was assembled so as to reduce the SEI formation. In the anode-limited cell configuration, the anode weight was increased by 20 %, resulting in a $n = +0.2$ to the overall capacity balance:

$$C_+ = C_- \cdot (1 + 20\ \%) \tag{5.7}$$

In addition, a wider voltage scan range is explored in order to enhance the specific capacity output at low voltage values during discharge. **Figure 4.11** shows the galvanostatic charge/discharge voltage vs specific capacity profiles of the anode-limited NFP/HC full cell, cycled at C/10 rate between 1.2-4 V vs. Na^+/Na at ambient laboratory temperature. The anode-limited configuration and the enlarged voltage window led to an increase of the overall specific capacity (110 mAh g^{-1} upon the first charge cycle and 87 mAh g^{-1} in the second charge cycle) due to a consistent decrease in the capacity drop after the first charge process. The coulombic efficiency of the first cycle considerably increased from 64 % of the slightly cathode-limited cell to a remarkable 82 %, which then remains constant above 97 % upon prolonged cycling, as shown in **Figure 4.12**. Analysing separately the two different changes in parametric setting, **Figure 4.13** shows the benefit on the first charge/discharge cycle in terms of reduced SEI formation with the switch to the anode-limited configuration. During charge a lower percentage of active Na^+ are trapped on the anode surface with the decomposition of the electrolyte, therefore higher values (+ 8.9 % with respect to the cathode-limited configuration) of specific capacity are reached in the following discharge. Moreover, the charge voltage profile of the anode-limited configuration exhibits a steeper linear segment and a flatter subsequent plateau.

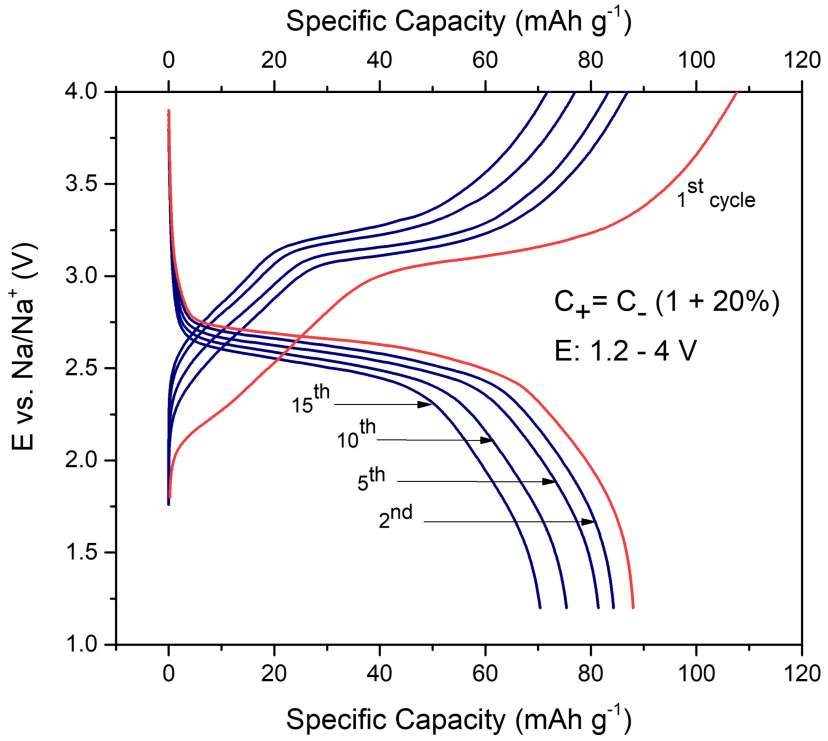

Figure 4.11 Charge/discharge voltage vs specific capacity profiles of the anode-limited NFP/HC full cell, cycled within the 1.2-4 V vs Na^+/Na voltage range at ambient laboratory temperature.

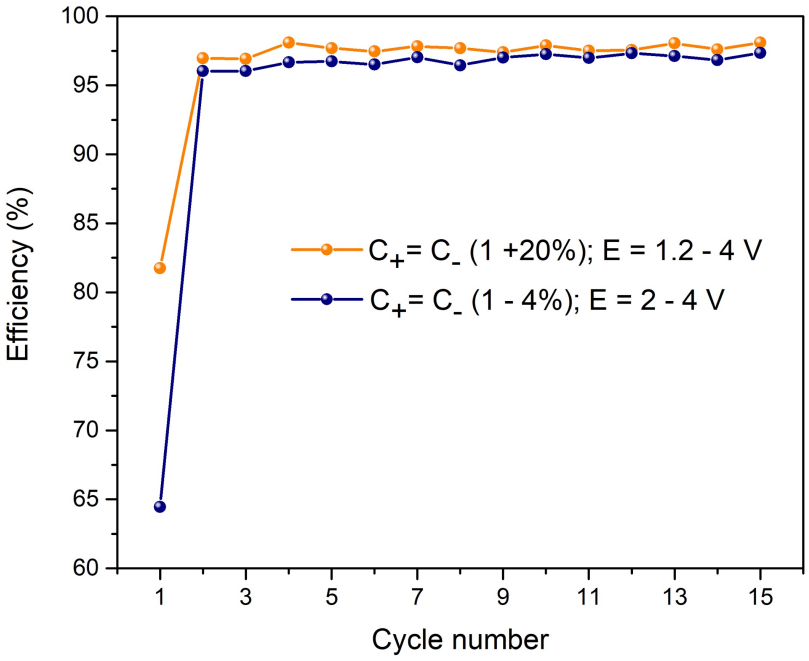

Figure 4.12 Comparison of the coulombic efficiency of the NFP/HC full cells cycled at C/10 at ambient laboratory temperature: cathode-limited in the voltage range 2-4 V vs Na^+/Na (blue line) and anode-limited with voltage window 1.2-4 V vs Na^+/Na (orange line).

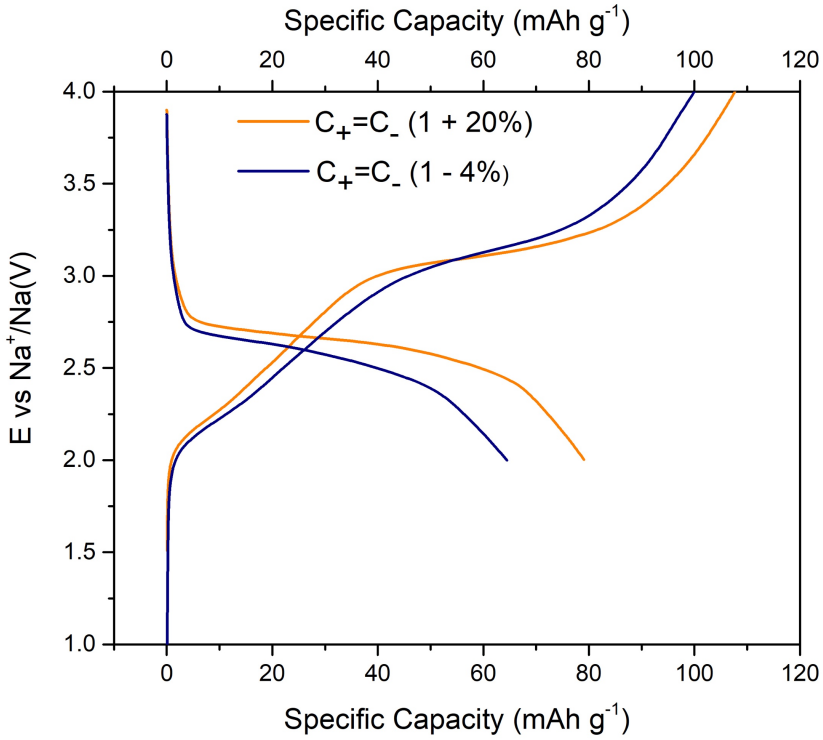

Figure 4.13 First charge/discharge voltage vs specific capacity profiles of the cathode-limited (blue line) and anode-limited (orange line) NFP/HC full cells, cycled at C/10 rate at ambient laboratory temperature.

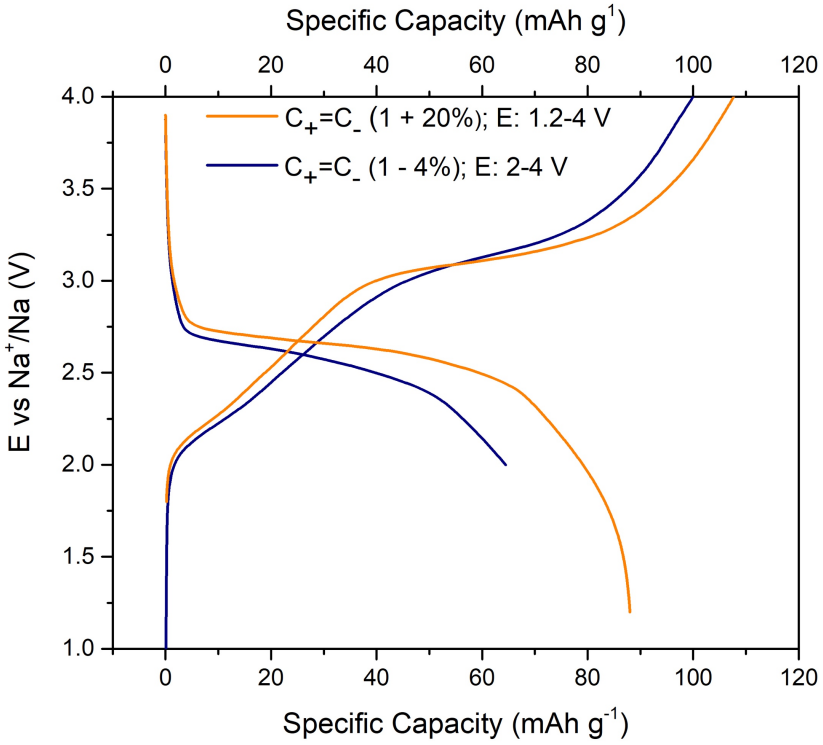

Figure 4.14 First charge/discharge cycle vs specific capacity profiles of the cathode-limited (2-4 V vs Na^+/Na, blue line) and anode-limited (1.2-4 V vs Na^+/Na, orange line) NFP/HC full cell configurations , both cycled at C/10 rate at ambient laboratory temperature.

Figure 4.14, instead, shows the specific capacity enhancement during the first discharge cycle due to the increased voltage window. Overall, the beneficial effects of the new parametric setting in terms of enhancement in the specific capacity output is well evident; nevertheless, by comparing **Figure 4.9** and **Figure 4.11,** a worse capacity retention from the second to the fifteen cycle is observed in the anode-limited full cell configuration, thus a deeper analysis of this aspect is carried out in the following section.

4.5.2 Considerations over specific energy

As briefly introduced before, comparing **Figure 4.9** and **Figure 4.11,** it is worth underlying the slightly lower capacity retention of the anode-limited configuration with increased voltage window. Indeed, 17 mAh g^{-1} are lost between the second and the fifteen charge cycles compared to the 11 mAh g^{-1} of the cathode-limited cell. Thus, the two cell configurations have been analysed in terms of specific energy (Wh g^{-1}). In ideal operating conditions, when the battery is discharged, it delivers to the load the full energy stored during the previous charge process, whereas in real operating conditions an energy loss is always recorded due to irreversible processes and it can be evaluated as the area enclosed by the voltage profiles of a charge and the successive discharge process: the lesser is the difference in average potential between the two profiles, the lower is the amount of energy lost. In this respect, **Figure 4.15** shows the energy loss of the anode-limited NFP/HC full cell during the second charge/discharge cycle.

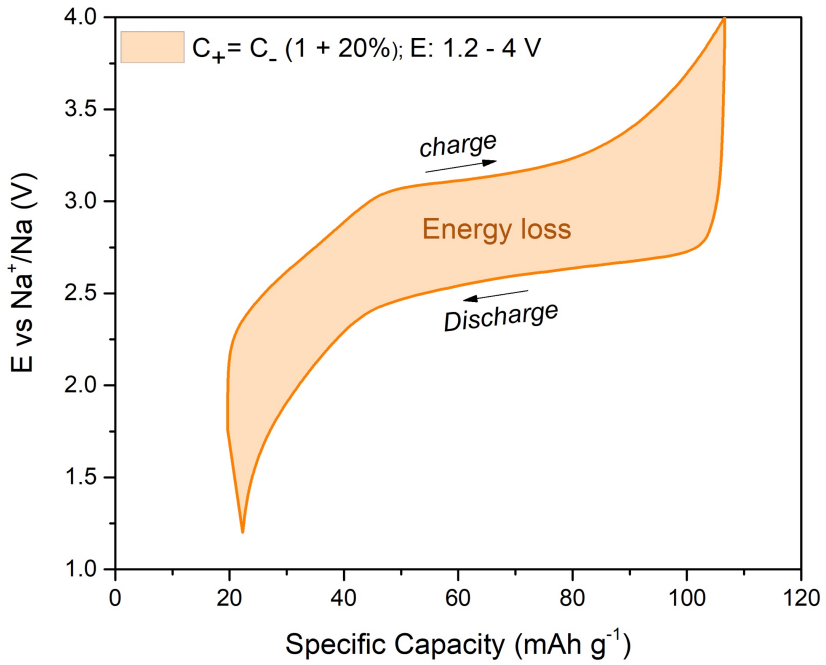

Figure 4.15 Energy loss at the second charge/discharge cycle of the anode-limited NFP/HC full cell, cycled at C/10 rate at ambient laboratory temperature.

Figure 4.16 compares the energy losses of the two NFP/HC full cell configurations under study at their 2nd and 15th charge/discharge cycles, respectively. Despite the much higher amount of energy stored and successively delivered by the anode-limited NFP/HC full cell, the graphs shows that the 15th and the 2nd cycles of the cathode-limited system better overlap one with each other if compared to the corresponding cycles of the anode-limited configuration; it accounts for enhanced amount of energy loss by this latter system. **Figure 4.17** confirms the above reported analysis by showing the evolution of the charge and discharge specific energies of the two systems with the number of cycles.

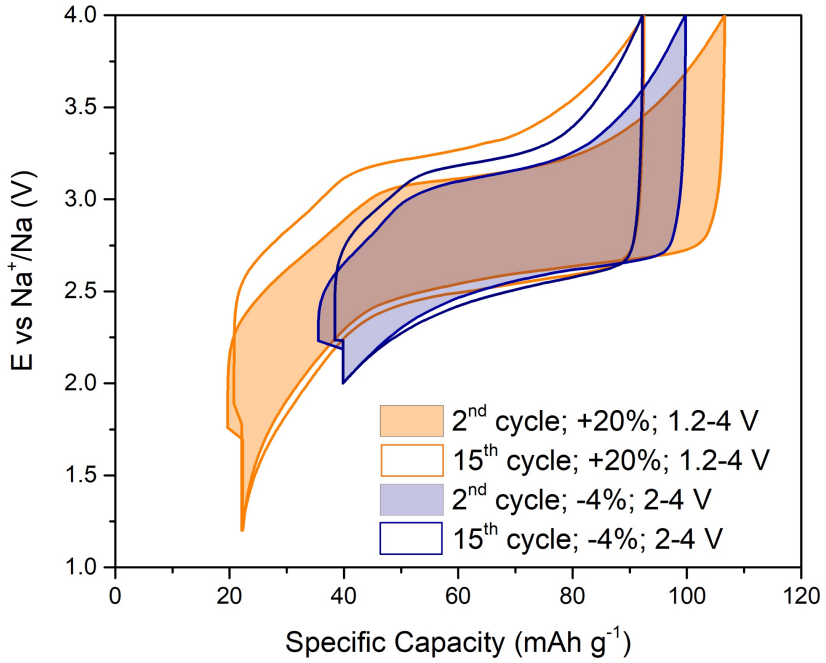

Figure 4.16 Energy losses at the 2nd and 15th charge/discharge cycles of the two NFP/HC full cell configurations under study (cathode-limited in blue and anode-limited in orange), cycled at C/10 rate at ambient laboratory temperature.

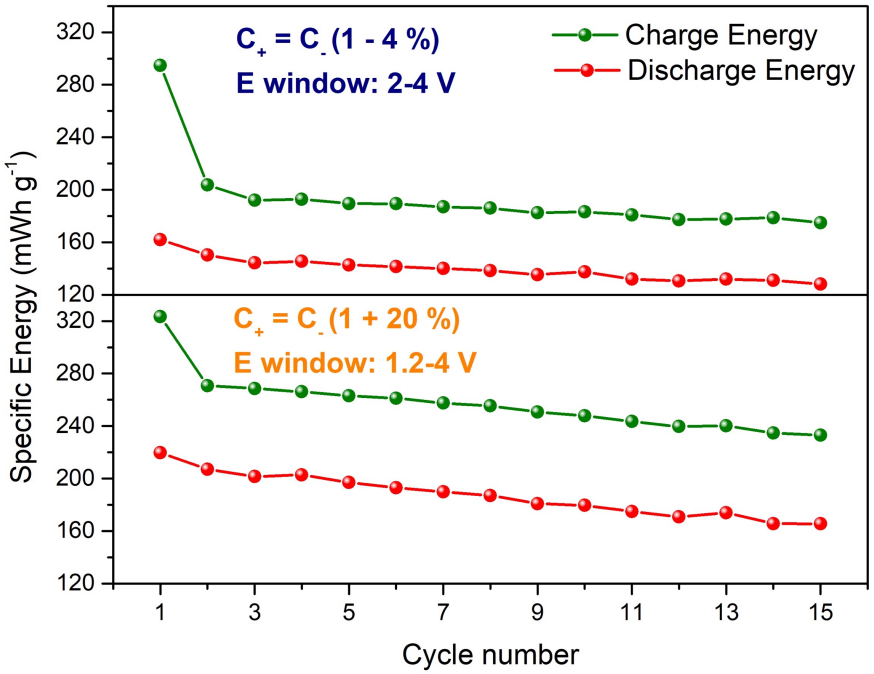

Figure 4.17 Evolution of the charge and discharge specific energy values with cycle number of the two NFP/HC full cell configurations under study.

The reduced SEI formation of the anode-limited configuration accounts for a reduced amount of active Na^+ ions adsorbed at the interface during the first cycle, thereby allowing to extend the electrochemical extraction of Na^+ from the HC electrode structure and reducing the specific energy loss at the second charge cycle. In this respect, **Figure 4.17** shows the considerable difference in the specific energy drop during charge after the first cycle. However, upon prolonged cycling, both the charge and discharge specific energies of the anode-limited configuration undergo a more pronounced overall decrease compared to the cathode-limited configuration, confirming in the results shown in **Figure 4.16.** The extended voltage scan range of the anode-limited configuration likely leads to detrimental side reactions between the active materials and the electrolyte at very low voltage values (see the curved sloping decay of the discharge voltage profiles at low voltage in **Figure 4.11**), which clearly results in increased capacity fade. Therefore, further adjustments of the capacity balance and operating voltage window are highly recommended in order to optimise the working conditions of the NFP/HC system.

4.6 Electrochemical characterization in full cells of the chemically sodium intercalated NaFePO4

This section shows the electrochemical results of the galvanostatic cycling of the olivine structured $NaFePO_4$, obtained via chemical oxidation of the pristine commercial $LiFePO_4$ and sub-sequent reduction of the de-lithiated $FePO_4$, as illustrated in **paragraph 4.1.2**. The active material is galvanostatically cycled in R-2032 coin-type NFP/HC full cell in the anode-limited configuration and voltage scan range from 1.2 to 4 V vs Na^+/Na. **Figure 4.18** shows noticeable differences in the electrochemical performances with respect to the electrochemically sodium intercalated $NaFePO_4$ detailed in the previous paragraphs, which is rather unexpected based on the literature reports [81].

By the analysis of the graph, three basic considerations arise and are discussed in the followings. On one side, the galvanostatic cycling at C/10 rate shows greatly reduced overall specific capacity, which is approximately half of the values obtained by the electrochemically intercalated $NaFePO_4$, and a low initial coulombic efficiency of 75 % due to a robust SEI formation. On the other hand, it is worth noting the greatly enhanced capacity retention upon prolonged cycling, with very high and stable the coulombic efficiency values exceeding 99 %.

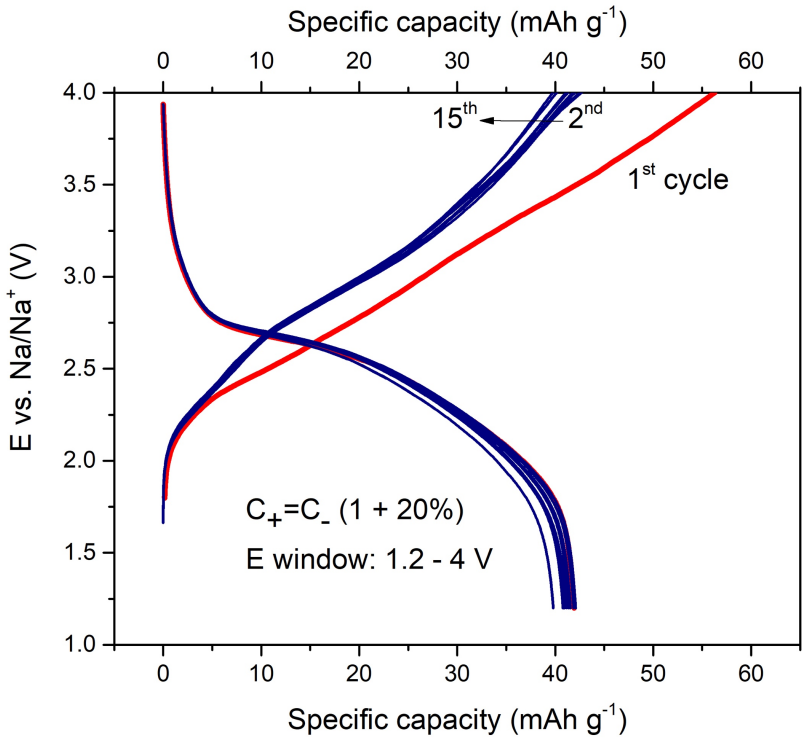

Figure 4.18 Charge/discharge voltage vs specific capacity profiles of the chemically sodium intercalated $NaFePO_4$ in anode-limited NFP/HC full cell configuration cycled at C/10 at ambient laboratory temperature in the voltage scan range 1.2-4 V vs Na^+/Na.

Differently from the corresponding electrochemically sodiated material, both the chemical de-lithiation and the following sodiation are time-demanding reactions because of the low kinetics of the processes. Although this does not fully accounts for the limited values of specific capacity provided by the chemically sodiated material (worth further investigation and optimisation), the chemical process in which Li+ ions are slowly extracted and Na+ ions are correspondingly slowly inserted in $Li(Na)FePO_4$ might improve the stability of the resulting $NaFePO_4$ structure and, thus, to the more efficient de/intercalation of Na^+. Eventually, the third viewable consideration is the absence of the characteristic flat plateau during the charge process. Also in this case, it worth further investigation in the structural characterization of the chemically obtained $NaFePO_4$, which might shows interesting differences with respect to the electrochemically obtained $NaFePO_4$.

4.7 Structural characterization of the chemically and electrochemically prepared $FePO_4$ and $NaFePO_4$

X-ray powder diffraction (XRD) patterns were obtained by a *Bruker DB Advanced* diffractometer equipped with Cu Kα radiation source in order to evaluate the modifications of the olivine-type structures of $FePO_4$ and $NaFePO_4$ after the chemical or electrochemical de-lithiation and sodium intercalation from the pristine orthorhombic $LiFePO_4$. The diffraction data were collected in the 2θ range of 18-50° with intermittent step of 0.02°.

Figure 4.19 shows the XRD patterns of the electrochemically prepared samples ($FePO_4$ and $NaFePO_4$), compared to the diffraction lines of the pristine $LiFePO_4$. The analysis of the main diffraction peaks clearly assesses the presence of the expected orthorhombic olivine-type crystalline system featuring a '*Pmnb*' space group both for the heterosite de-lithiated $FePO_4$ and the sodium iron phosphate[12] $NaFePO_4$. the purity of the $FePO_4$ profile accounts for the absence of any lithium derived phase, which means that all lithium has been properly extracted from the $LiFePO_4$ structure; moreover, only few very low intensity, minor peaks ascribable to a residual $FePO_4$ phase are depicted by asterisks in the $NaFePO_4$ diffraction line.

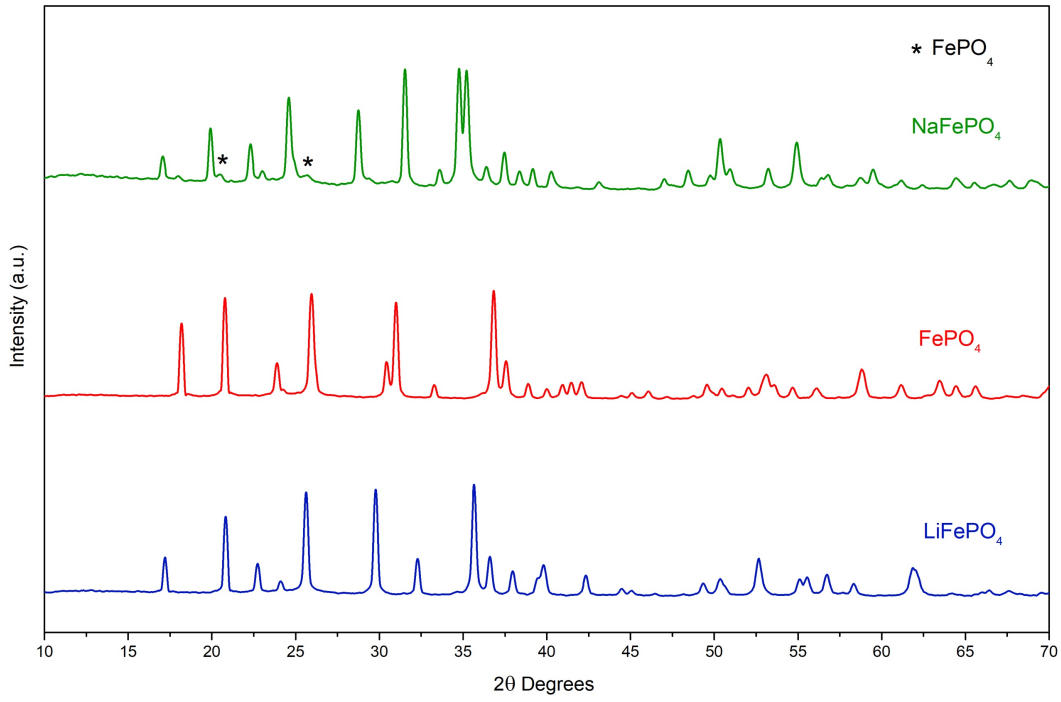

Figure 4.19 X-Ray powder diffraction profiles (2θ = 10-70°) of the electrochemically prepared samples $FePO_4$ and $NaFePO_4$, compared to the XRPD of the pristine $LiFePO_4$.

[12] Concerning the orthorhombic $FePO_4$, the main phase reported is the heterosite syn, while the main phase of $NaFePO_4$ is actually sodium 0.7 iron phosphate ($Na_{0.7}FePO_4$), namely the most stable intermediate phase already described during the electrochemical characterization.

For the sake of comparison, the XRPD diffraction profile of the chemically prepared $FePO_4$ and $NaFePO_4$ samples are shown in **Figure 4.20**, which again confirms the expected retention of the orthorhombic olivine-type phase. No clear differences with respect to the electrochemically prepared samples can be evidenced by the analysis of the diffraction profiles, which accounts for the efficiency of both the electrochemical and chemical preparation methods in obtaining sodiated iron phosphate cathode materials with excellent structure retention.

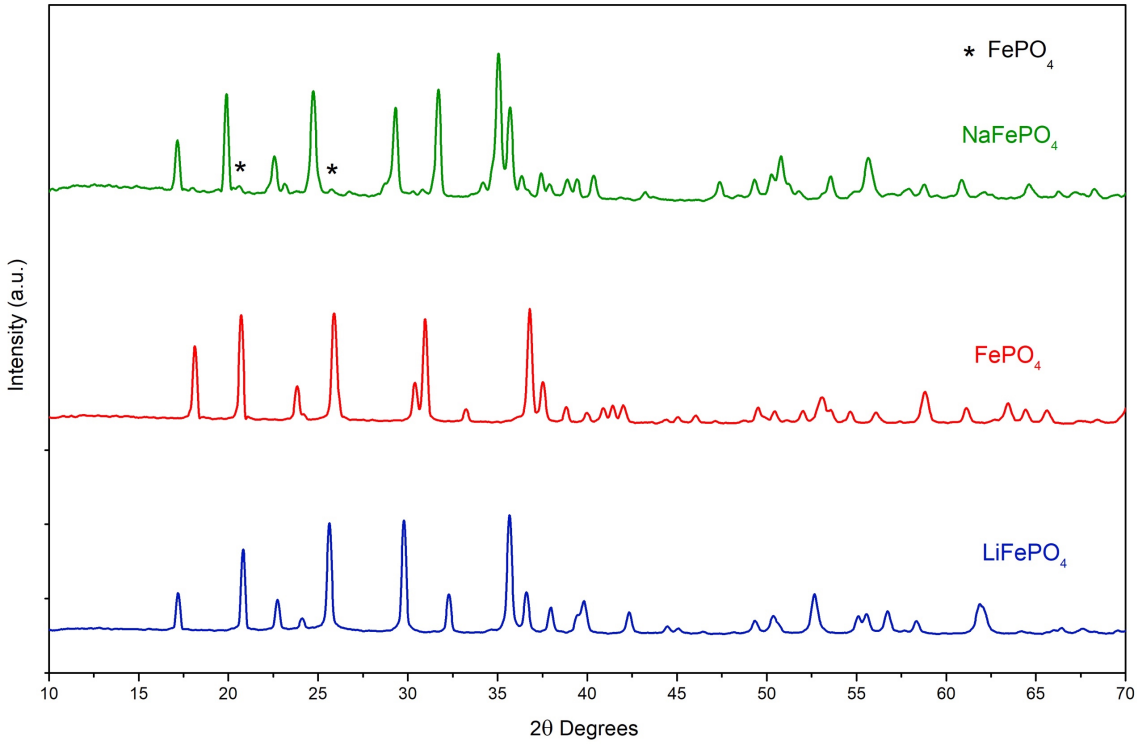

Figure 4.20 X-Ray powder diffraction profiles (2θ = 10-70°) of the chemically prepared samples $FePO_4$ and $NaFePO_4$, compared to the XRPD of the pristine $LiFePO_4$.

The purity of the chemically prepared $NaFePO_4$ is only slightly higher than its electrochemically prepared counterpart, as it can be seen by the complete absence of minor peaks marked by asterisks. Clearly, the XRPD analysis cannot provide any useful information to validate hypothesis of an enhanced structural stability of the chemically prepared sample, which might lead to the better capacity retention discussed in **paragraph 4.6**, as well as to justify the different electrochemical behaviour of the two samples; thus, further work in terms of optimisation and deeper characterisation is needed in this respect.

Future outlook and conclusion

In the framework of advanced alkali metal ion based battery systems, which are the technology of choice for the use in hybrid-electric vehicles and clean energy storage systems from renewables, this experimental thesis work focuses on the development and characterization of high performing nanostructured olivine-type cathode materials, having enhanced conductivity, Li^+/Na^+ ion diffusion and rate capability thanks to the specific addition of graphene oxide during electrode preparation and/or peculiar preparation techniques adopted.

In particular, $LiFePO_4$, among the huge list of potential new cathode materials, meets the safety and stability requirements needed for powering electric cars and owns the potential to dominate the grid-connected use due to the eco-friendliness and abundance of its constituting elements.

During the experimental activity I firstly tried to provide a solution for the intrinsic disadvantages of this material in terms of low lithium ion diffusion and electronic conductivity, which hinder to exploit the full electrochemical activity under high current regimes. Based on the encouraging results reported in literature on the performance enhancement of materials for the negative electrode, I followed the hypothesis that the striking conductivity properties of graphene could donate a desired ultrafast capability and help the active ions to efficiently diffuse among the particles. In this sense, $LiFePO_4$ was directly synthesized via the easy and low-cost hydrothermal synthetic route, which involves the dissolution of the precursors in water followed by an annealing stage under inert (N_2) atmosphere. Test electrodes containing $LiFePO_4$ and graphene oxide as the conductivity enhancer were prepared by standard 'doctor blading'. The electrochemical tests (galvanostatic cycling and cyclic voltammetry) confirmed that the use of graphene oxide allows enhanced Li^+ diffusion among the active material particles under very high current regimes (higher than 20C rate, up to 50C) and guarantees faster kinetics and extended electrochemical activity of extraction and insertion of Li^+ in the olivine-type structure of the material.

Following the promising results, I evaluated the addition of graphene oxide on a hydrothermally synthesized $LiFePO_4$, industrially optimized for delivering high capacity at low C-rates, but with intrinsic limitations in the ultrafast rate capability. The electrochemical tests did not show significant performance enhancement by the use of graphene oxide

because graphene oxide, likely due to the presence of oxygen, does not feature the real conductivity properties of pure graphene. As a result, chemical reduction was performed in alkaline environment with ascorbic acid as reducing agent. The X-ray diffraction confirmed the successful reduction and the electrochemical tests showed very interesting results. Indeed, the addition of the reduced graphene oxide as conductivity enhancer in the electrode preparation process led to an overall increase in specific capacity of the $LiFePO_4$ cathode up to the 10C rate and an improved kinetics of the extraction and insertion of the Li^+ ions. However, ultrafast rate capability at very high C-rates was not achieved as for the graphene oxide modified hydrothermally synthesized material. The reason probably resides in the different synthesis process of the material; being industrially optimized for working under low current regimes, the characteristics of the internal structure may intrinsically prevent the electrochemical activity at elevated C-rates, regardless of the enhancement brought by the reduced graphene oxide, which uniformly covers the grains with a homogeneous conductive layer, but does not modify the internal structure of the material.
Always following the same the idea of improving the characteristics of $LiFePO_4$, the second experimental activity carried out at Collège de France applied a different approach and looked forward to the future of the electrochemical storage systems. Indeed, I explored the possibility of using $LiFePO_4$ as pristine material for the chemical and electrochemical cationic exchange that involve the removal of lithium- and the insertion of sodium-ions to form the sodium-based corresponding polyphosphate $NaFePO_4$ (NFP), owning the same orthorhombic crystalline systems with favourable cationic channels for a fast and ease extraction and insertion of active Na^+ ions. The results demonstrated the successful and truly reversible electrochemical and chemical de-lithiation of $LiFePO_4$ and the sub-sequent insertion of Na^+. In particular, 0.8 Na^+ per formula unit can be intercalated and de-intercalated in the structure of the de-lithiated $FePO_4$ maintaining the desired olivine-type structure of the pristine lithiated material. However, the larger ionic size of sodium ions led to a strong interaction with the host structure, accounting for a more complex phase transformations during the Na^+ extraction and insertion and the formation of an intermediate phase during cycling. To the best of my knowledge, this work firstly proved the feasible cyclability at C/10 rate of $NaFePO_4$ cathode material in full Na-ion cells coupled with commercial hard carbon (HC) disks as anode. I tried to explore two different capacity balances and operating potential windows in order to fully exploit the theoretical performances of this cathode material. As a result, the anode-limited configuration guarantees lower capacity fade during the first cycle due to the SEI formation and the voltage window 1.2 – 4 V allows to reach higher specific capacity values. The comparison of

the galvanostatic cycling at C/10 rate in the NFP/HC full cell configuration resulted in interesting differences between the chemically and electrochemically prepared $NaFePO_4$. The electrochemically sodium intercalated compound exhibits higher specific capacity values, whereas the chemically prepared sample shows astonishing cycling stability worthy of a deeper future analysis.

Summarising, in this experimental research work I have successfully explored two different paths for the improvement of lithium iron phosphate-based Li-/Na-ion battery cathodes with remarkable results in terms of specific capacity output, rate capability and cycling stability. Further investigations in both directions might open the doors to other interesting developments. Concerning the addition of graphene, more complex synthesis techniques, already implemented with other electrode materials, might be explored to produce graphene/$LiFePO_4$ hybrids in which graphene oxide or reduced graphene oxide wrap the active particles or are anchored between the material layers. Among these, the 'spray-drying' is an interesting technique that nebulizes the active material with graphene to form micro-sized, spherical particles covered by graphene sheets, resulting in enhanced electrochemical conductivity and optimal buffering of disruptive effects of the volume change during cycling. It might be interesting to apply this synthesis technique to both $LiFePO_4$ and $NaFePO_4$, with the latter suffering from larger volume change. Regarding the sodium intercalated $NaFePO_4$, it owns appealing electrochemical and environmental advantages; further research work is still to be done to optimize the material, and indeed the sodium-ion technology itself, to properly understand its characteristic and electrochemical behaviour before considering it commercially viable.

Appendix

I. Experimental techniques for structural characterization

I.I X-ray powder diffraction

X-ray diffraction is an effective non-destructive survey technique, which provides information on the crystallographic structure and chemical composition of a material in the form of powder or thin film. When a monochromatic X-ray, having a wavelength λ of the same order of magnitude as the interatomic distance between the crystalline planes of the material, hits the sample, the ray is reflected. A peak is recorded when a constructive interference occurs between the crystalline planes and the incident beam. The relationship between the incident angle (θ) and the wavelength (λ) of the X-ray is given by the Bragg's law:

$$n\lambda = 2d_{hkj}sin\theta \tag{I.I}$$

A constructive interference occurs when the distance (d_{hkj}) between two adjacent crystalline planes is equal to an integer (n) multiple of λ. In the case of powders $n = 1$. The difference between a constructive and a destructive interference is shown in **Figure I.I**.

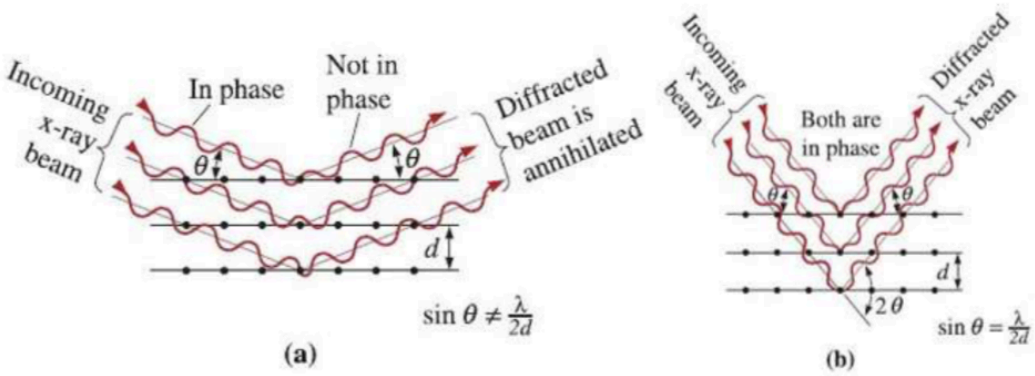

Figure I.I Bragg's law. Destructive (a) and constructive (b) interference [102].

A diffractometer (**Figure I.II**) consists of a monochromatic X-ray generator and a diffracted X-ray detector, which records the angle θ to which the beam is diffracted, giving the characteristic diffraction pattern. Since the length of the incident beam is known, the interplanar distance and the identity of the planes that cause diffraction can be determined by the Bragg's law [102].

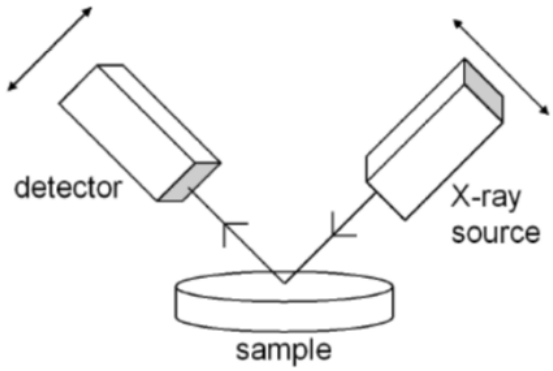

Figure I.II Schematic representation of a X-ray diffractometer [5].

Two diffractometers are used to detect the X-ray powder diffraction profiles of the sample in this work: an X'Pert MPD DY 1165 and a Bruker DB Advanced diffractometer both equipped with a Cu Kα radiation source (λ = 1.541 Å; 40 kV; 30 mA; 30°–50° 2θ, step size: 0.02° 2θ; 0.02 s per step).

II. Electrochemical testing techniques

In this work, the electrochemical testing of the samples has been carried out with a Battery Testing System model BT-2000 from Arbin Instruments (US) and a potentiostat/galvanostat/frequency response analyser model MPG-101 from Bio-logic (France).

II.I Cyclic Voltammetry

Cyclic voltammetry is a powerful technique, which allows to apply a potential linearly variable in time between a working and a reference electrode, while the current flowing through the working and a counter electrode is registered. The resulting diagram of the current as a function of the potential shows anodic and cathodic peaks at precise values of the x-axis, corresponding to the potential at which the electrochemical oxidation and reduction reactions occur. The relative height between the anodic and the cathodic peaks

reveals the reversibility of the process, while the area underlying provides information about the speed of the reaction. The velocity of the potential scan $(\frac{dV}{dt})$ is an important parameter, which influences the results of the test. In particular, if the scan is too fast, some electrochemical processes may not be detected.

II.II Galvanostatic cycling technique

The galvanostatic cycling technique consists in the application of a direct and constant current to the test cell and provides different quantitative and qualitative information on the electrochemical processes occurring during several sub-sequent charge and discharge cycles. Generally, two important graphical information can be extracted. Firstly, the voltage can be monitored as a function of time, providing information about the operating potential and the reversibility of the reduction/oxidation processes of the active material. Furthermore, the shape of the voltage profile versus time depicts the ion insertion and de-insertion mechanism in the host material. A mechanism that leads to a solid solution of the inserted ion in the host material appears as a sloping curve, whereas a plateau identifies a stoichiometric phase. Secondly, this technique allows measuring the capacity per unit mass, namely the amount of charge passed during discharge or charge, at different C-rates. The cycle life of the cell can be tested by maintaining the same C-rate (namely providing a constant current) for the required number of cycles, while the capacity retention and the stability of the active material can be evaluated by varying the C-rate.

Bibliography

[1] "WEO." [Online]. Available: https://www.iea.org/weo/. [Accessed: 12-Feb-2019].

[2] "The future of electric vehicles | Sustainability | Home." [Online]. Available: https://www.bp.com/en/global/corporate/sustainability/climate-change/a-low-carbon-future/electric-vehicles.html. [Accessed: 14-Feb-2019].

[3] E. Telaretti and L. Dusonchet, "Stationary battery technologies in the U.S.: Development Trends and prospects," *Renew. Sustain. Energy Rev.*, vol. 75, pp. 380–392, Aug. 2017.

[4] V. Pop, H. J. Bergveld, V. Danilov, and P. P. L. Regtien, "State-of-the-Art of battery State-of-Charge determination," in *Battery Management Systems*, Dordrecht: Springer Netherlands, 2008, pp. 11–45.

[5] C. Gerbaldi, "Mesoporous Materials and Nanostructured LiFePO4 as cathodes for secondary Li-ion batteries: synthesis and characterisation," Politecnico di Torino, 2006.

[6] M. Armand and J. M. Tarascon, "Issues and Challenges Facing Rechargeable Lithium Batteries," *Nature*, vol. 414, no. May, pp. 359–367, 2001.

[7] D. W. Murphy, F. J. Di Salvo, J. N. Carides, and J. V. Waszczak, "Topochemical reactions of rutile related structures with lithium," *Mater. Res. Bull.*, vol. 13, no. 12, pp. 1395–1402, Dec. 1978.

[8] M. Lazzari and B. Scrosati, "A Cyclable Lithium Organic Electrolyte Cell Based on Two Intercalation Electrodes," *J. Electrochem. Soc.*, vol. 127, no. 3, p. 773, Mar. 1980.

[9] M. Mohri *et al.*, "Rechargeable lithium battery based on pyrolytic carbon as a negative electrode," *J. Power Sources*, vol. 26, no. 3–4, pp. 545–551, May 1989.

[10] A. B. Gallo, J. R. Simões-Moreira, H. K. M. Costa, M. M. Santos, and E. Moutinho dos Santos, "Energy storage in the energy transition context: A technology review," *Renew. Sustain. Energy Rev.*, vol. 65, pp. 800–822, Nov. 2016.

[11] N. Nitta, F. Wu, J. T. Lee, and G. Yushin, "Li-ion battery materials: Present and future," *Mater. Today*, vol. 18, no. 5, pp. 252–264, 2015.

[12] M. S. Whittingham, "Electrical Energy Storage and Intercalation Chemistry," *Science (80-.).*, vol. 192, no. 4244, p. 1126 LP-1127, Jun. 1976.

[13] J. B. Goodenough, *Advances in lithium-ion batteries*. Kluwer Academic/Plenum Publisher, New York 4, 2007.

[14] K. Mizushima, P. C. Jones, P. J. Wiseman, and J. B. Goodenough, "LixCoO2 (0<x<-1): A new cathode material for batteries of high energy density," *Mater. Res. Bull.*, vol. 15, no. 6, pp. 783–789, Jun. 1980.

[15] A. Du Pasquier, I. Plitz, S. Menocal, and G. Amatucci, "A comparative study of Li-ion battery, supercapacitor and nonaqueous asymmetric hybrid devices for automotive applications," *J. Power Sources*, vol. 115, no. 1, pp. 171–178, Mar. 2003.

[16] J. N. Reimers and J. R. Dahn, "Electrochemical and In Situ X-Ray Diffraction Studies of Lithium Intercalation in Li[sub x]CoO[sub 2]," *J. Electrochem. Soc.*, vol. 139, no. 8, p. 2091, Aug. 1992.

[17] R. V. Chebiam, F. Prado, and A. Manthiram*, "Soft Chemistry Synthesis and Characterization of Layered Li1-xNi1-yCoyO2-δ (0 ≤ x ≤ 1 and 0 ≤ y ≤ 1)," 2001.

[18] G. G. Amatucci, “CoO[sub 2], The End Member of the Li[sub x]CoO[sub 2] Solid Solution,” *J. Electrochem. Soc.*, vol. 143, no. 3, p. 1114, 1996.

[19] B. Scrosati, “Recent advances in lithium ion battery materials,” *Electrochim. Acta*, vol. 45, no. 15–16, pp. 2461–2466, May 2000.

[20] P. T. Onnerud, J. J. Shi, S. L. Dalton, and C. Lampe-Onnerud, “Lithium metal oxide materials and methods of synthesis and use,” 21-May-2004.

[21] C. H. Chen, J. Liu, M. E. Stoll, G. Henriksen, D. R. Vissers, and K. Amine, “Aluminum-doped lithium nickel cobalt oxide electrodes for high-power lithium-ion batteries,” *J. Power Sources*, vol. 128, no. 2, pp. 278–285, Apr. 2004.

[22] D. Guyomard, “New trends in electrochemical technology: energy storage systems for electronics,” in *Energy Storage Systems for Electronics*, vol. 9, T. Osaka and M. Datta, Eds. Amsterdam: Gordon & Breach Science Publishers, 2000, pp. 253–350.

[23] M. M. Thackeray, W. I. F. David, P. G. Bruce, and J. B. Goodenough, “Lithium insertion into manganese spinels,” *Mater. Res. Bull.*, vol. 18, no. 4, pp. 461–472, Apr. 1983.

[24] G. Amatucci, A. Du Pasquier, A. Blyr, T. Zheng, and J.-M. Tarascon, “The elevated temperature performance of the LiMn2O4/C system: failure and solutions,” *Electrochim. Acta*, vol. 45, no. 1–2, pp. 255–271, Sep. 1999.

[25] K.S. Lee, H.J. Bang, S.T. Myung, J.Prakash, K.Amine, and Y.K. Sun, “Synthesis and electrochemical properties of spherical spinel Li1.05M0.05Mn1.9O4 (M = Mg and Al) as a cathode material for lithium-ion batteries by co-precipitation method,” *J. Power Sources*, vol. 174, no. 2, pp. 726–729, Dec. 2007.

[26] Yang-Kook Sun, Seung-Taek Myung, Myung-Hoon Kim, Jai Prakash, and K. Amine, “Synthesis and Characterization of Li[(Ni0.8Co0.1Mn0.1)0.8(Ni0.5Mn0.5)0.2]O2 with the Microscale Core−Shell Structure as the Positive Electrode Material for Lithium Batteries,” 2005.

[27] Y.K. Sun, S.T. Myung, B.C. Park, J. Prakash, I. Belharouak, and K. Amine, “High-energy cathode material for long-life and safe lithium batteries,” *Nat. Mater.*, vol. 8, no. 4, pp. 320–324, Apr. 2009.

[28] B. Scrosati and J. Garche, “Lithium batteries: Status, prospects and future,” *J. Power Sources*, vol. 195, no. 9, pp. 2419–2430, 2010.

[29] Z. Gong and Y. Yang, “Recent advances in the research of polyanion-type cathode materials for Li-ion batteries,” *Energy Environ. Sci.*, vol. 4, no. 9, p. 3223, 2011.

[30] J.-M. Tarascon and M. Armand, “Issues and challenges facing rechargeable lithium batteries,” *Nature*, vol. 414, no. 6861, pp. 359–367, Nov. 2001.

[31] C. Delacourt *et al.*, “Toward Understanding of Electrical Limitations (Electronic, Ionic) in LiMPO[sub 4] (M=Fe, Mn) Electrode Materials,” *J. Electrochem. Soc.*, vol. 152, no. 5, p. A913, May 2005.

[32] H. Huang, S.-C. Yin, T. Kerr, N. Taylor, and L. F. Nazar, “Nanostructured Composites: A High Capacity, Fast Rate Li3V2(PO4)3/Carbon Cathode for Rechargeable Lithium Batteries,” *Adv. Mater.*, vol. 14, no. 21, pp. 1525–1528, Nov. 2002.

[33] N. Recham *et al.*, “A 3.6 V lithium-based fluorosulphate insertion positive electrode for lithium-ion batteries,” *Nat. Mater.*, vol. 9, no. 1, pp. 68–74, Jan. 2010.

[34] A. K. Padhi, K. S. Nanjundaswamy, and J. B. Goodenough, “Phospho-olivines as Positive-Electrode Materials for Rechargeable Lithium Batteries,” *J. Electrochem. Soc.*, vol. 144, no. 4, p. 1188, Apr. 1997.

[35] G. Zubi, R. Dufo-López, M. Carvalho, and G. Pasaoglu, “The lithium-ion battery: State of the art and future perspectives,” *Renew. Sustain. Energy Rev.*, vol. 89, no. March, pp. 292–308, 2018.

[36] A. . Andersson and J. . Thomas, “The source of first-cycle capacity loss in LiFePO4,” *J. Power Sources*, vol. 97–98, pp. 498–502, Jul. 2001.

[37] A. S. Andersson, B. Kalska, L. Häggström, and J. O. Thomas, “Lithium extraction/insertion in LiFePO4: an X-ray diffraction and Mössbauer spectroscopy study,” *Solid State Ionics*, vol. 130, no. 1–2, pp. 41–52, May 2000.

[38] A. Yamada, S. C. Chung, and K. Hinokuma, “Optimized LiFePO[sub 4] for Lithium Battery Cathodes,” *J. Electrochem. Soc.*, vol. 148, no. 3, p. A224, Mar. 2001.

[39] G. Meligrana, C. Gerbaldi, A. Tuel, S. Bodoardo, and N. Penazzi, “Hydrothermal synthesis of high surface LiFePO 4 powders as cathode for Li-ion cells,” vol. 160, pp. 516–522, 2006.

[40] F. Di Lupo, G. Meligrana, C. Gerbaldi, S. Bodoardo, and N. Penazzi, “Electrochimica Acta Surfactant-assisted mild solvothermal synthesis of nanostructured LiFePO 4 / C cathodes evidencing ultrafast rate capability,” *Electrochim. Acta*, vol. 156, pp. 188–198, 2015.

[41] M. A. Hannan, M. M. Hoque, A. Hussain, Y. Yusof, and P. J. Ker, “State-of-the-Art and Energy Management System of Lithium-Ion Batteries in Electric Vehicle Applications: Issues and Recommendations,” *IEEE Access*, vol. 6, no. c, pp. 19362–19378, 2018.

[42] W. Xu *et al.*, “Lithium metal anodes for rechargeable batteries,” *Energy Environ. Sci.*, vol. 7, no. 2, pp. 513–537, Jan. 2014.

[43] B. N. Loeffler, D. Bresser, S. Passerini, and M. Copley, “Secondary Lithium-Ion Battery Anodes: From First Commercial Batteries to Recent Research Activities,” *Johnson Matthey Technol. Rev.*, vol. 59, no. 1, pp. 34–44, 2015.

[44] D. Bresser, E. Paillard, and S. Passerini, “Advances in batteries for medium- and large-scale energy storage,” in *Advances in batteries for medium- and large- scale energy storage*, C. Menictas, M. Skyllas-Kazacos, and T. M. Lim, Eds. Cambridge, UK: Woodhead Publishing, 2014.

[45] R. A. Huggins, “Lithium Alloy Anodes,” in *Handbook of Battery Materials*, Weinheim, Germany: Wiley-VCH Verlag GmbH, 1999, pp. 359–381.

[46] E. Ferg, R. J. Gummow, A. de Kock, and M. M. Thackeray, “Spinel Anodes for Lithium-Ion Batteries,” *J. Electrochem. Soc.*, vol. 141, no. 11, p. L147, Nov. 1994.

[47] M. B. Pinson and M. Z. Bazant, “Theory of SEI Formation in Rechargeable Batteries: Capacity Fade, Accelerated Aging and Lifetime Prediction,” *J. Electrochem. Soc.*, vol. 160, no. 2, pp. A243–A250, Jan. 2013.

[48] H. J. Ploehn, P. Ramadass, and R. E. White, “Solvent Diffusion Model for Aging of Lithium-Ion Battery Cells,” *J. Electrochem. Soc.*, vol. 151, no. 3, p. A456, Mar. 2004.

[49] P. Verma, P. Maire, and P. Novák, “A review of the features and analyses of the solid electrolyte interphase in Li-ion batteries,” *Electrochim. Acta*, vol. 55, no. 22, pp. 6332–6341, Sep. 2010.

[50] Q. Li, J. Chen, L. Fan, X. Kong, and Y. Lu, “Progress in electrolytes for rechargeable Li-based batteries and beyond,” *Green Energy Environ.*, vol. 1, no. 1, pp. 18–42, 2016.

[51] K. Xu, “Nonaqueous Liquid Electrolytes for Lithium-Based Rechargeable Batteries,” 2004.

[52] L. Yang, B. Ravdel, and B. L. Lucht, “Electrolyte Reactions with the Surface of High Voltage LiNi[sub 0.5]Mn[sub 1.5]O[sub 4] Cathodes for Lithium-Ion Batteries,” *Electrochem. Solid-State Lett.*, vol. 13, no. 8, p. A95, Aug. 2010.

[53] L. Hu, Z. Zhang, and K. Amine, “Electrochemical investigation of carbonate-based electrolytes for high voltage lithium-ion cells,” *J. Power Sources*, vol. 236, pp. 175–180, Aug. 2013.

[54] Z. Zhang *et al.*, “Fluorinated electrolytes for 5 V lithium-ion battery chemistry,” *Energy Environ. Sci.*, vol. 6, no. 6, p. 1806, May 2013.

[55] J. R. Croy, A. Abouimrane, and Z. Zhang, “Next-generation lithium-ion batteries: The promise of near-term advancements,” *MRS Bull.*, vol. 39, no. 05, pp. 407–415, May 2014.

[56] W. Li, J. R. Dahn, and D. S. Wainwright, “Rechargeable Lithium Batteries with Aqueous Electrolytes,” *Science (80-.).*, vol. 264, no. 5162, pp. 1115–1118, May 1994.

[57] J.-Y. Luo, W.-J. Cui, P. He, and Y.-Y. Xia, “Raising the cycling stability of aqueous lithium-ion batteries by eliminating oxygen in the electrolyte,” *Nat. Chem.*, vol. 2, no. 9, pp. 760–765, Sep. 2010.

[58] M. Zhao, B. Zhang, G. Huang, H. Zhang, and X. Song, “Excellent rate capabilities of (LiFePO4/C)//LiV3O8 in an optimized aqueous solution electrolyte,” *J. Power Sources*, vol. 232, pp. 181–186, Jun. 2013.

[59] L. Suo *et al.*, “‘Water-in-salt’ electrolyte enables high-voltage aqueous lithium-ion chemistries.,” *Science*, vol. 350, no. 6263, pp. 938–43, Nov. 2015.

[60] J. L. Schaefer, Y. Lu, S. S. Moganty, P. Agarwal, N. Jayaprakash, and L. A. Archer, “Electrolytes for high-energy lithium batteries,” *Appl. Nanosci.*, vol. 2, no. 2, pp. 91–109, Jun. 2012.

[61] C. Tang, K. Hackenberg, Q. Fu, P. M. Ajayan, and H. Ardebili, “High Ion Conducting Polymer Nanocomposite Electrolytes Using Hybrid Nanofillers,” *Nano Lett.*, vol. 12, no. 3, pp. 1152–1156, Mar. 2012.

[62] C. A. Lundgren, K. Xu, T. R. Jow, J. Allen, and S. S. Zhang, “Lithium-Ion Batteries and Materials,” in *Springer Handbook of Electrochemical Energy*, Berlin, Heidelberg: Springer Berlin Heidelberg, 2017, pp. 449–494.

[63] A. K. Geim and K. S. Novoselov, “The rise of graphene,” *Nat. Mater.*, vol. 6, no. 3, pp. 183–191, Mar. 2007.

[64] C. Lee, X. Wei, J. W. Kysar, and J. Hone, “Measurement of the elastic properties and intrinsic strength of monolayer graphene.,” *Science*, vol. 321, no. 5887, pp. 385–8, Jul. 2008.

[65] J. C. Meyer, A. K. Geim, M. I. Katsnelson, K. S. Novoselov, T. J. Booth, and S. Roth, “The structure of suspended graphene sheets,” *Nature*, vol. 446, no. 7131, pp. 60–63, Mar. 2007.

[66] A. A. Balandin *et al.*, “Superior Thermal Conductivity of Single-Layer Graphene,” *Nano Lett.*, vol. 8, no. 3, pp. 902–907, Mar. 2008.

[67] E. Yoo, J. Kim, E. Hosono, H. Zhou, and T. Kudo, “Large Reversible Li Storage of Graphene Nanosheet Families for Use in,” *Nano*, pp. 13–18, 2008.

[68] Y. Dong, Z. S. Wu, W. Ren, H. M. Cheng, and X. Bao, “Graphene: a promising 2D material for electrochemical energy storage,” *Sci. Bull.*, vol. 62, no. 10, pp. 724–740, 2017.

[69] M.S.Kim *et al.*, “Synthesis of Reduced Graphene Oxide-Modified LiMn0.75Fe0.25PO4Microspheres by Salt-Assisted Spray Drying for High-Performance Lithium-Ion Batteries,” *Sci. Rep.*, vol. 6, no. May, pp. 1–13, 2016.

[70] N. Sulaiman, M. A. Hannan, A. Mohamed, E. H. Majlan, and W. R. Wan Daud, “A review on energy management system for fuel cell hybrid electric vehicle: Issues and

challenges," *Renew. Sustain. Energy Rev.*, vol. 52, pp. 802–814, Dec. 2015.

[71] "Democratic Republic of Congo: "This is what we die for": Human rights abuses in the Democratic Republic of the Congo power the global trade in cobalt | Amnesty International." [Online]. Available: https://www.amnesty.org/en/documents/afr62/3183/2016/en/. [Accessed: 07-Feb-2019].

[72] J.-M. Tarascon, "Is lithium the new gold?," *Nat. Chem.*, vol. 2, no. 6, pp. 510–510, Jun. 2010.

[73] "USGS Mineral Resources Program." [Online]. Available: https://minerals.usgs.gov/. [Accessed: 07-Feb-2019].

[74] "Cars produced in the world - Worldometers." [Online]. Available: http://www.worldometers.info/cars/. [Accessed: 08-Feb-2019].

[75] W. Tahil, "'The trouble with lithium'. Implications of Future PHEV Production for Lithium Demand.," *Meridian Int. Res.*, pp. 1–22, 2007.

[76] P. Barpanda, L. Lander, S. I. Nishimura, and A. Yamada, "Polyanionic Insertion Materials for Sodium-Ion Batteries," *Adv. Energy Mater.*, vol. 8, no. 17, pp. 1–26, 2018.

[77] B. L. Ellis and L. F. Nazar, "Sodium and sodium-ion energy storage batteries," *Curr. Opin. Solid State Mater. Sci.*, vol. 16, no. 4, pp. 168–177, Aug. 2012.

[78] J. Lu, S. C. Chung, S. I. Nishimura, and A. Yamada, "Phase diagram of olivine NaxFePO4(0 < x < 1)," *Chem. Mater.*, vol. 25, no. 22, pp. 4557–4565, Nov. 2013.

[79] F. Sauvage, L. Laffont, and J.-M. Tarascon, and E. Baudrin*, "Study of the Insertion/Deinsertion Mechanism of Sodium into Na0.44MnO2," 2007.

[80] P. K. Nayak, L. Yang, W. Brehm, and P. Adelhelm, "From Lithium-Ion to Sodium-Ion Batteries: Advantages, Challenges, and Surprises," *Angew. Chemie - Int. Ed.*, vol. 57, no. 1, pp. 102–120, 2018.

[81] P. Moreau, D. Guyomard, J. Gaubicher, and F. Boucher, "Structure and stability of sodium intercalated phases in olivine FePO4," *Chem. Mater.*, vol. 22, no. 14, pp. 4126–4128, 2010.

[82] S. M. Oh, S. T. Myung, J. Hassoun, B. Scrosati, and Y. K. Sun, "Reversible NaFePO4electrode for sodium secondary batteries," *Electrochem. commun.*, vol. 22, no. 1, pp. 149–152, 2012.

[83] B. Jache and P. Adelhelm, "Use of Graphite as a Highly Reversible Electrode with Superior Cycle Life for Sodium-Ion Batteries by Making Use of Co-Intercalation Phenomena," *Angew. Chemie*, vol. 126, no. 38, pp. 10333–10337, Sep. 2014.

[84] H. Kim, J. Hong, Y.-U. Park, J. Kim, I. Hwang, and K. Kang, "Sodium Storage Behavior in Natural Graphite using Ether-based Electrolyte Systems," *Adv. Funct. Mater.*, vol. 25, no. 4, pp. 534–541, Jan. 2015.

[85] Y. Wen *et al.*, "Expanded graphite as superior anode for sodium-ion batteries," *Nat. Commun.*, vol. 5, no. 1, p. 4033, Dec. 2014.

[86] C. Bommier and X. Ji, "Recent Development on Anodes for Na-Ion Batteries," *Isr. J. Chem.*, vol. 55, no. 5, pp. 486–507, May 2015.

[87] K. Vignarooban *et al.*, "Current trends and future challenges of electrolytes for sodium-ion batteries," *Int. J. Hydrogen Energy*, vol. 41, no. 4, pp. 2829–2846, Jan. 2016.

[88] N. Ravet, Y. Chouinard, J. F. Magnan, S. Besner, M. Gauthier, and M. Armand, "Electroactivity of natural and synthetic triphylite," *J. Power Sources*, vol. 97–98, pp. 503–

507, Jul. 2001.

[89] F. Croce, A. D' Epifanio, J. Hassoun, A. Deptula, T. Olczac, and B. Scrosati, "A Novel Concept for the Synthesis of an Improved LiFePO[sub 4] Lithium Battery Cathode," *Electrochem. Solid-State Lett.*, vol. 5, no. 3, p. A47, Mar. 2002.

[90] J. Ma and Q.-Z. Qin, "Electrochemical performance of nanocrystalline LiMPO4 thin-films prepared by electrostatic spray deposition," *J. Power Sources*, vol. 148, pp. 66–71, Sep. 2005.

[91] J. Gao, F. Liu, Y. Liu, N. Ma, Z. Wang, and X. Zhang, "Environment-Friendly Method To Produce Graphene That Employs Vitamin C and Amino Acid," *Chem. Mater.*, vol. 22, no. 7, pp. 2213–2218, Apr. 2010.

[92] J. Chen, B. Yao, C. Li, and G. Shi, "An improved Hummers method for eco-friendly synthesis of graphene oxide," *Carbon N. Y.*, vol. 64, pp. 225–229, Nov. 2013.

[93] K. K. H. De Silva, H. H. Huang, R. K. Joshi, and M. Yoshimura, "Chemical reduction of graphene oxide using green reductants," *Carbon N. Y.*, vol. 119, pp. 190–199, 2017.

[94] M. J. Fernández-Merino *et al.*, "Vitamin C Is an Ideal Substitute for Hydrazine in the Reduction of Graphene Oxide Suspensions," *J. Phys. Chem. C*, vol. 114, no. 14, pp. 6426–6432, Apr. 2010.

[95] Z. Sui, X. Zhang, Y. Lei, and Y. Luo, "Easy and green synthesis of reduced graphite oxide-based hydrogels," *Carbon N. Y.*, vol. 49, no. 13, pp. 4314–4321, 2011.

[96] A. Abulizi, K. Okitsu, and J. J. Zhu, "Ultrasound assisted reduction of graphene oxide to graphene in l-ascorbic acid aqueous solutions: Kinetics and effects of various factors on the rate of graphene formation," *Ultrason. Sonochem.*, vol. 21, no. 3, pp. 1174–1181, 2014.

[97] C. Xu, X. Shi, A. Ji, L. Shi, C. Zhou, and Y. Cui, "Fabrication and Characteristics of Reduced Graphene Oxide Produced with Different Green Reductants," *PLoS One*, vol. 10, no. 12, p. e0144842, Dec. 2015.

[98] J. Lu, S. C. Chung, S. I. Nishimura, and A. Yamada, "Phase diagram of olivine NaxFePO4(0 < x < 1)," *Chem. Mater.*, vol. 25, no. 22, pp. 4557–4565, 2013.

[99] C. Delacourt, J. Rodríguez-Carvajal, B. Schmitt, J.-M. Tarascon, and C. Masquelier, "Crystal chemistry of the olivine-type LixFePO4 system (0⩽x⩽1) between 25 and 370 °C," *Solid State Sci.*, vol. 7, no. 12, pp. 1506–1516, Dec. 2005.

[100] Y. Zhu, Y. Xu, Y. Liu, C. Luo, and C. Wang, "Comparison of electrochemical performances of olivine $NaFePO_4$ in sodium-ion batteries and olivine $LiFePO_4$ in lithium-ion batteries," *Nanoscale*, vol. 5, no. 2, pp. 780–787, Dec. 2013.

[101] G. Yan, R. Dugas, and J.-M. Tarascon, "The Na 3 V 2 (PO 4) 2 F 3 /Carbon Na-Ion Battery: Its Performance Understanding as Deduced from Differential Voltage Analysis," *J. Electrochem. Soc.*, vol. 165, no. 2, pp. A220–A227, 2018.

[102] D. A. Askeland, P. . Fulay, and W. J. Wright, *The science and engineering of materials*, Sixth Edit. Cengage Learning, 2010.

[103] "The Paris Agreement | UNFCCC." [Online]. Available: https://unfccc.int/process-and-meetings/the-paris-agreement/the-paris-agreement. [Accessed: 12-Feb-2019].

Acknowledgements

I would like to express my very special thanks to my supervisor Professor Claudio Gerbaldi and my co-supervisor Doctor Giuseppina Meligrana. They gave me the opportunity to work in a completely new field, they trusted in me and wisely guided me through this experience, fruitful under both professional and human aspect. I also deeply appreciated the help and the patience of Francesca and Marisa of the Game Lab, who kindly spent a lot of their time answering to all my annoying questions and solving the countless problems raised by my clumsiness in the practical laboratory activity.

My heartfelt gratitude goes to Professor Jean-Marie Tarascon for the outstanding experience he enabled me to live in its laboratory at Collège de France, in Paris. I felt part of a very passionate and high-quality research group from whom I learned a lot. Special appreciation to Claudio, without whom my Parisian experience would have been even much harder than what it has been.

Thanks to all my friends and colleagues of Politecnico di Torino for the laughs and the joy through these years of heavy lectures and stressful examination sessions. Especially Pierluigi, my dear first flatmate, and Andrea for the days and nights spent studying together, I owe to you a great part of my academical achievements. Thanks to the dear friends, old and new, who supported me and believed in me during these years. To this sense, a special thought goes to Greta.

I would also like to say a great thank you to my flatmates Alice and Giampaolo (special mates in good and bad luck), Jùlia, Manuela and Paolo for your fellowship, fondness and mutual esteem. In a short space of time we have built a profound bond and I will strongly feel your most tender affection in all my future challenges.

Lastly, and most importantly, the deepest gratitude is reserved to my family for the daily encouragement and love. The endless care of my parents and my brother is fundamental and this thesis is dedicated to them.